Christoffer Kolbeinsen Surdal

Testing the use of acoustic emission sensors to detect in-situ hydraulic jacking

Experiences gained during the fieldwork and the potential use of AE to detect hydraulic jacking during high pressure pre-excavation grouting

Master thesis in environmental- and geotechnology
Trondheim 31.05.2021
Supervisor: Eivind Grøv, (SINTEF & NTNU)
Co-supervisor: Helene Strømsvik (SINTEF)

Norwegian university of science and technology
Faculty of engineering
Department of geoscience and petroleum

NTNU

Norwegian University of
Science and Technology

Norges teknisk-naturvitenskapelige universitet
NTNU

Fakultet for ingeniørvitenskap
Institutt for geovitenskap og petroleum
Studieprogram tekniske geofag

MASTEROPPGAVEN 60 poeng

Kandidatens navn: Christoffer Kolbeinsen Surdal

Oppgavens tittel: Teste bruk av sensorer for akustisk emisjon (AE) til å detektere hydraulisk jekking i felt
–Erfaringer fra feltforsøk av AE's potensial for påvisning av hydraulisk jekking under forinjeksjon med høyt trykk

English title: Testing the use of acoustic emission sensors to detect in-situ hydraulic jacking – Experiences gained during the fieldwork and the potential use of AE to detect hydraulic jacking during high pressure pre-excavation grouting.

Utfyllende tekst: Når en bergmasse utsettes for hydraulisk jekking skapes lavfrekvente vibrasjoner som propagerer radiellt ut fra punktet i bergmassen der jekkingen fant sted. Dette fenomenet kalles akustisk emisjon (AE) og ved hjelp av geofoner (vibrasjons-sensorer) kan slike signal identifiseres og prosesseres. Ved bruk av geofoner i felt vil det bli forsøkt å detektere hydraulisk jekking under ett hydraulisk splitteforsøk, dette gjøres for å bedre forståelsen av prosessen rundt hydraulisk jekking.

Under driving av tunneler benyttes vanligvis forinjeksjon for å få kontroll på innlekkasjen av vann i tunneler. I Norge benyttes det injeksjonstrykk typisk mellom 50-100 bar under slike arbeider. Det høye trykket kan medføre som konsekvens at sprekker som det injiseres på utvides ved at det oppstår hydraulisk jekking i bergmassen. Potensialet for bruk av AE for deteksjon av jekking under forinjeksjon skal også bli undersøkt. Her skal gjennomførbarhet, nytteverdi og mulige fremgangsmåter skal vektlegges.

Hensikten med ovennevnte arbeid i MSc-oppgaven er å:

- Teste bruk av AE for å detektere/måle jekking under utførelse av hydrauliske splitteforsøk.
- Analysere AE parametere for å etablere en forståelse av prosessene som opptrer under jekking.
- Diskutere lærdommen fra feltarbeidet mot rapporterte hendelser.
- Undersøke potensialet ved bruk av AE for deteksjon av hydraulisk jekking under arbeider med forinjeksjon i underjordsanlegg.

Ansvarlig faglærer og hovedveileder for oppgaven er Prof. II Eivind Grøv, Institutt for geovitenskap og petroleum.

Studieretning: Geologi

Hovedprofil: Miljø- og geoteknologi

Tidsrom: 23.08.2020-01.06.2021

Eivind Grøv

Abstract

In this thesis acoustic emission sensors were used to monitor a hydraulic fracturing stress measurement test to see whether AE could be used to detected hydraulic jacking (HJ) in-situ. Then an attempt was made to discern any difference in the acoustic parameters related to hydraulic fracturing, hydraulic jacking and noise. To achieve this the AE hits were filtered using the program AEwin then passed through a python code that would extract the acoustic parameters, analyze them using a mann-whitney u test and then plot them in box-plots. The acoustic hits was then transformed from the time domain to the frequency domain using a fast-Fourier transform to analyze the waves for differences occurring in the resulting frequency spectra. This data was then compared with similar data in the literature.

The data acquired during the field work was extremely noisy due to water leaks hitting the sensors and substantial filtering was needed. Out of the initial 7568 AE-hits 66 remained for further analysis post-filtering, this is thought to have significantly impacted the results. The apparent trend found in the data of this thesis goes against that indicated by previous literature. Hence it remains inconclusive whether HJ was detected or not.

The thesis shows the importance of acoustic shielding as a filtering mechanism and argues that wave-guides or boreholes should be implemented in future AE-monitoring programs together with source location to improve the usefulness of the monitoring.

AE-monitoring was never conducted during pre-excavation grouting due to unforeseen consequences related to sub-optimal borehole quality. It is still discussed how AE-monitoring of pre-excavation grouting can be a valuable tool to help detect real instances of hydraulic jacking. AE could potentially be used in conjunction with pressure- and flow graphs or other methods of analysis to classify instances of false jacking interpretation. Based on the AE-rate plots in previous literature showing an increase in AE-hits during fracture initiation and reopening it is seen as likely that hydraulic jacking during pre-excavation grouting can be detected through the use of AE-sensors.

Sammendrag

I denne oppgaven ble akustiske emisjonsensorer brukt til å overvåke et hydraulisk splitting forsøk for å se om AE kunne brukes til å oppdage hydraulisk jekking (HJ) in-situ. Deretter ble det forsøkt å se hvilken forskjeller som fantes mellom de akustiske parametrene knyttet til hydraulisk splitting, hydraulisk jekking og støy. For å oppnå dette ble AE-treffene filtrert ved hjelp av programmet AEwin, og deretter passert gjennom en pythonkode som skulle trekke ut de akustiske parametrene, analysere dem ved hjelp av en mann-whitney u-test og deretter plotte dem i boks-plott. De akustiske treffene ble deretter transformert fra tidsdomenet til frekvensdomenet ved hjelp av en rask Fourier-transformasjon for å analysere bølgene for eventuelle forskjeller som forekommer i de resulterende frekvensspektrene. Denne dataen ble deretter sammenlignet med lignende data i litteraturen.

Dataene som ble innhentet under feltarbeidet inneholdt ekstremt mye støy på grunn av vann som traff sensorene, og det var nødvendig med omfattende filtrering. Ut i fra originalt 7568 AE-hits var kun 66 gjenværende etter filtrering, dette antas å ha påvirket resultatene betraktelig. Den tilsynelatende trenden som er funnet i oppgavens data, er i strid med data fra lignende undersøkelser i litteraturen. Derfor er det fortsatt uklart hvorvidt jekking ble oppdaget ved bruk av AE.

Oppgaven viser viktigheten av akustisk skjerming som en filtreringsmekanisme og argumenterer for at sensorer bør festes på bølgeledere (eng: wave-guide) eller i borehull under fremtidige prosjekter sammen med AE-kilde lokalisering for å forbedre overvåkingsprogrammet.

AE-overvåking ble aldri gjennomført under for-injeksjon på grunn av uforutsette konsekvenser knyttet til suboptimal borehullskvalitet. Det diskuteres fortsatt hvordan AE-overvåking av for-injeksjon kan være et verdifullt verktøy for å oppdage reelle forekomster av hydraulisk jekking. AE kan potensielt brukes i forbindelse med trykk- og strømningsdiagrammer eller andre analysemetoder for å klassifisere forekomster av falske jekke hendelser i dataen. Basert på AE-rate-plottene i tidligere litteratur som viser en økning i AE-treff under bruddinitiering og gjenåpning, blir det sett på som sannsynlig at hydraulisk jekking kan oppdages under for-injeksjon.

Preface

This thesis is part of a two year masters degree in geological science within the field of engineering geology from the Norwegian university of science and technology (NTNU).

The idea for the thesis was formulated while reading different papers regarding the topic of hydraulic fracturing. The concept of hydraulic fracturing initially intrigued me because of the uncertainty related to it, I wanted to think of other approaches for detecting it in-situ and landed on the idea of using acoustic emission sensors. The initial scope of the masters degree was to correlate AE-data with pressure-/flow data from a grouting rig to try and verify interpreted jacking based on this data. However, due to unforeseen circumstances this wasn't possible, resulting in the thesis being more theoretical in nature. The findings are still useful as they show what went wrong, how to mitigate these mistakes in the future as well as the theoretical idea behind using AE-sensors as a tool for monitoring pre-excavation grouting with regards to hydraulic jacking.

I would like to take this opportunity to thank everyone who has helped me during this masters degree and my higher education. First a great thank you to Eivind Grøv for his guidance and sharing his network with me and for helping me become a confident engineering geologist. Thank you to Helene Strømsvik for including me in her ongoing research project, purchasing the sensors using her project funds, planning and executing our field trips, valuable constructive discussion and for motivating me when our initial plan didn't work as expected. This thesis wouldn't have been possible without you, so thank you! Thank you to the rock mechanics lab and Gunnar Vistnes at NTNU for allowing me to use their AEwin licence remotely so that I wouldn't have to travel 8 hours by train just to get some data. Thank you to Henki Ødegaard for sharing his AE experience with me. Thank you to YIT and SKANSKA for allowing Helene and I to conduct our research at their ongoing projects. A great thank you to Sondre Hjelmeland for a critical review of my thesis. And lastly thank you to my girlfriend Nellie for her continuing support and patience during these past months of intense work.

Oslo 29.05.2021
Christoffer Kolbeinsen Surdal

"If we knew what it was we were doing, it would not be called research, would it?"
— Albert Einstein

Abbreviations

AE: Acoustic emission

DAS: Data acquisition system

HF: Hydraulic fracturing

HJ: Hydraulic jacking

MFC: Micro Fine Cement

MSPS: Mega Samples Per Second

NGU: Norwegian geological survey

NPRA: The Norwegian Public Roads Administration

OPC: Ordinary Portland Cement

PF-index: Pressure Flow Index

SMH: Structural health monitoring system.

SoC: System on a chip

Symbols

α: Alpha, attenuation coefficient

A: Amplitude (dB or V)

g: acceleration of gravity (m/s^2)

C: Wave propagation velocity (m/s)

Δa: Aperture change

dB: Decibel, unit used to measure the intensity of sound or power level of an electrical signal

Δ: Delta, often used to denote change or difference.

p: Density (kg/m^3)

p_w: Density of water (kg/m^3)

E: youngs modulus

f: Frequency (Hz)

Hz: SI unit for frequency equal to cycles per second (1 Hz = 1 cycle/second)

λ: Wavelength

Ma: Mega-annum, unit of time equal to million (10^6) years.

μ: mu, a common prefix for denoting micro (10^{-6})

μ_s: Microseconds (0.000001 second \$10^{-6}$ seconds)

μ_w: Viscosity of water (Pa· s)

ν: Poissons ratio

P: Common denomination of pressure (MPa)

P_g: Grouting pressure (Mpa/bar)

π: Mathematical constant Pi

Q: Flow rate of grout or water (m^3/s)

r: Radius

σ: sigma, used to denote stresses in geology (Mpa)

σ_h: Horizontal stress component (Mpa)

σ_v: Vertical stress component (Mpa)

V: Voltage.

List of Figures

List of Tables

Table of content

1 Introduction

Water control is an important task during both tunnel construction and operation as water ingress is associated with a number of problems. Within the tunnel these problems might include low advancement rates, unpleasant work environment, corrosion of rock support, higher costs due to for instance increased time usage etc. In addition water ingress could lower the surrounding ground water table which might affect recreational areas, sensitive fauna and flora, water supply wells and could cause subsidence damage on buildings during urban tunneling.
The preferred method of choice for water control in Norway is through the use of high pressure pre-excavation grouting. Meaning that the pressures used range from 15 bar all the way up to 100 bar, depending on the project requirements. In comparison the pressure used in Sweden is seldom higher than 35 bar , even if both nations have similar geology. This difference stems from Sweden taking a more analytical approach to grouting due to urban tunneling and strict tightness requirements for underground storage of nuclear waste. Where as Norway's strategy is largely based on experience and the approach was developed through the successful use of higher pressures from the early days of hydro-power development (Grøv et al. 2014).
One consequence of the high pressure used in Norwegian grouting is that the risk of hydraulic jacking (HJ) is increased. HJ will in general lead to higher grout consumption and longer grouting time as the volume needed to be grouted is increased when the fractures are dilated (Strømsvik 2019). The current practice for detecting HJ during rock mass grouting is in most parts retrospective through the analysis of pressure and flow data acquired from the grouting rig. Recent research are trying to create methods for detecting HJ in-situ, most notable of these is the RTGC-method, PF-index and data algorithms created for the grouting rigs, these methods will be further reviewed in the theory section of this thesis. Most of these methods are based on assumptions and are therefore prone to misinterpreting whether jacking actually have taken place, i.e. recording false-positive jacking instances as real jacking. Hence there exists a demand for a way to verify whether jacking actually takes place, so that these methods can be further refined. The author believes this demand can be filled by using acoustic emission (AE) sensors as a way to detect the acoustic signature associated with HJ during pre-excavation grouting, and potentially also detect jacking in real time, making it a powerful tool in the scientific study of the effect of grouting. The scope of this study will be to gather previous uses of AE in rock engineering as it relates to jacking, look further into the mechanisms and acoustic parameters related to hydraulic jacking, research the source of AE during jacking, discuss how AE can be beneficial in monitoring grouting works and check if HJ can be observed in-situ with the use of AE-sensors.

To test this the AE-sensors would be used in the field on two occasions; first they were tested during a hydraulic fracturing stress measurement test conducted at the construction site for Løkjelsvatn power plant. This was done to test the sensors during a setting where jacking was certainly occurring so that the AE-characteristics associated with it could be recorded, in the hopes that they would be similar at the AE-test during pre-excavation grouting. Then the second test would be conducted during pre-excavation grouting at Nordøyvegen road construction project, but due to unforeseen circumstances the planned monitoring couldn't be conducted; so no data was acquired during this field trip. Due to this shortfall the discussion surrounding this project will be focused on what went wrong and how it can be mitigated in future AE-monitoring trials. Further the acquired AE-data from Løkjelsvatn will be presented together with it's limitations, filtering, interpretation and potential improvements to the monitoring program.
In the following section a brief introduction to these two projects will be given, followed by the regional and local geology for each one.

1.1 Løkjelsvatn power plant

To try and detect hydraulic jacking in-situ the AE-sensors were tested on hydraulic fracturing stress measurement tests conducted at the construction site for Løkjelsvatn power plant. The power plant is located in Etne municipality in the south-western part of Norway. The project is owned by Sunnhordaland Kraftlag (SKL), and the company hired to conduct the construction work is YIT Infra Norway AS (YIT 2018).
This project will consist of the construction of 5,1 km of tunnels, a power plant- and transformer hall, all placed underground with a rock cover of 541 meters. The total volume of blasted rock for the whole project is estimated to be 250 000 m^3 (NVE 2017). An overview of the tunnels and their placement is shown on the map in Fig.1. The power plant is projected to be finished before the end of 2021 and it's annual electricity production is estimated to be 163 GWh.

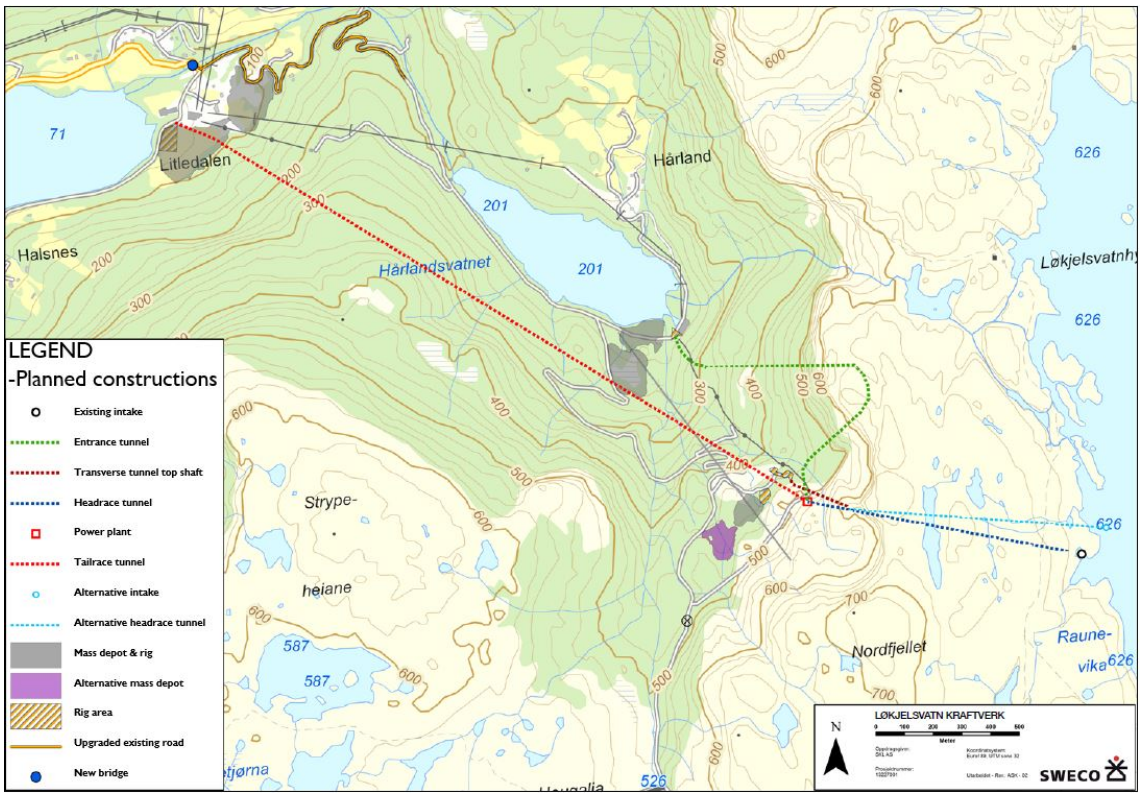

Figure 1: Overview of the planned constructions in the Løkjelsvatn power plant project. Translated to english from map in SKL (2018).

1.2 Nordøyvegen construction project

The tunnel where the planned in-situ AE monitoring during pre-excavation grouting was suppose to take place, is a part of the Nordøyvegen road construction project in Møre and Romsdal county, Norway (Fig.2). The goal of the construction project is to connect the islands of Lepsøya, Haramsøya, Skuløya/Flemsøya, Fjørtofta and Harøya to the mainland (Prop. 140 S 2016-2017), this will be achieved through the construction of three sub-sea tunnels, three bridges and a causeway (Skanska 2018). The different constructions and their length is shown in Table 1.
The construction contract with a value of 2,982 billion NOK was given to Skanska Norway in 2018; construction started in march 2019 and is estimated to be finalized within 2022 Skanska (2018).

Table 1: The different constructions used to cross the fjords with their length and connections indicated.

Construction	Length	Connection
Haramsfjord tunnel	3,5 km	Hestøya - Austnes
Nogvafjord tunnel	5,7 km m	Longva - Fjørtofta
Fjørtoftfjord tunnel	3,7 km	Fjørtofta - Myklebust
Causeway	2,7 km	Skjeltene - Lepsøya and Hestøya
Lepsøy bridge	800 m	Skjeltene - The causeway
Two minor bridges	109 m/200 m	Within the causeway

Source: *(Prop. 140 S 2016-2017).*

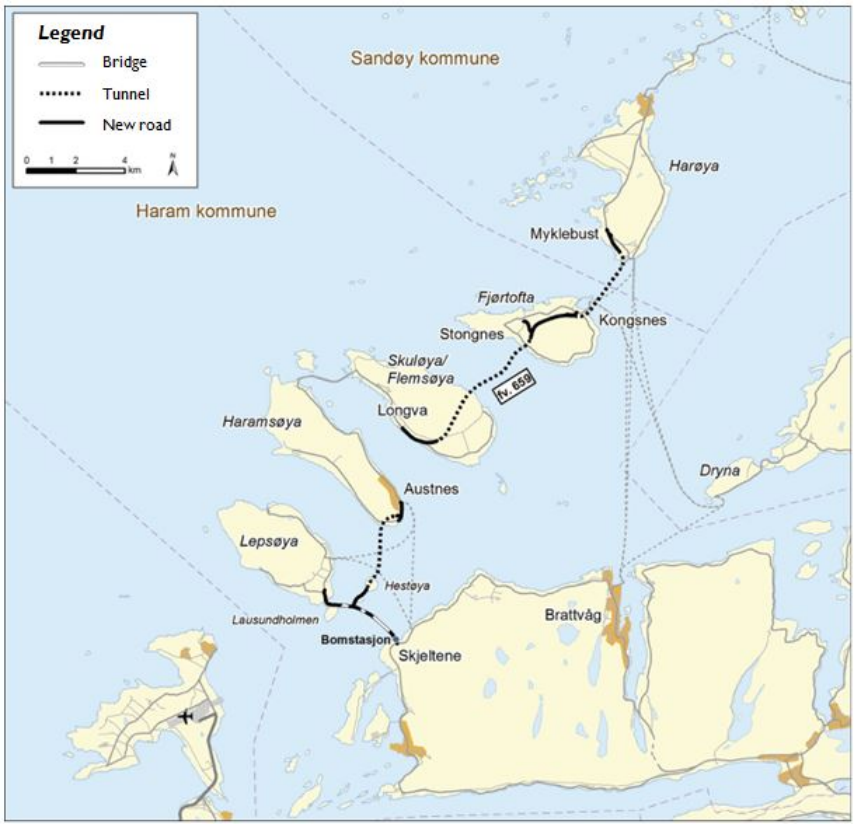

Figure 2: Overview map of the construction project Nordøyvegen in Møre and Romsdal county, Norway. Translated to english by the author from original figure in Prop. 140 S, 2016-2017.

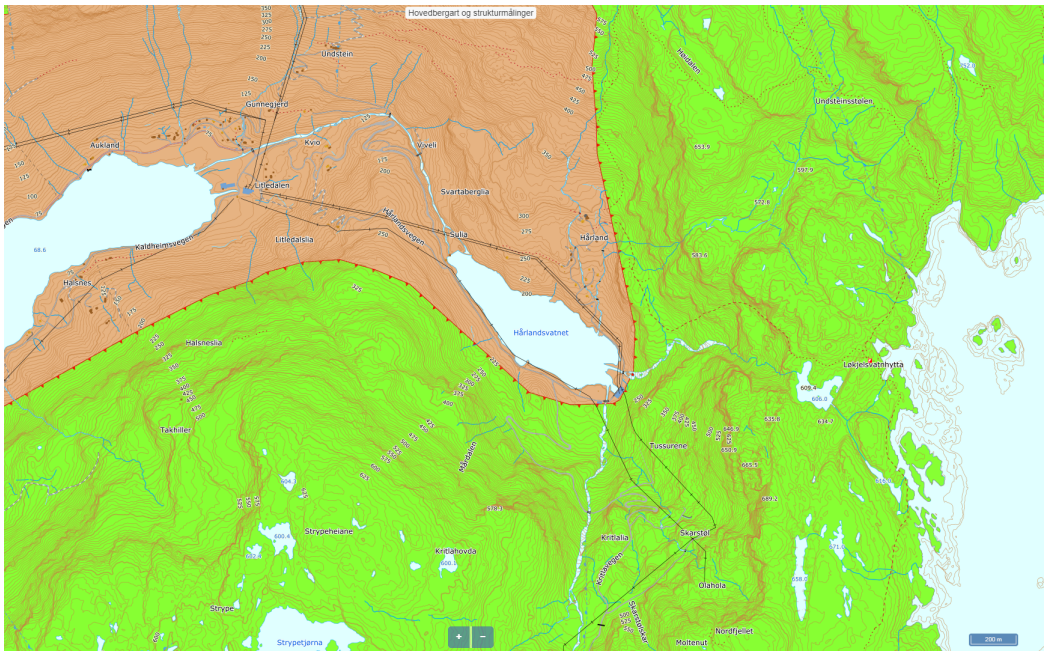

Figure 3: Map snipp from NGU. Green indicates a caledonian nape consisting of phyllite, some place garnet bearing and with sporadic quartz lenses (541 - 458.4 Ma). Brown is an amphibolitic gneiss (1600 - 1000 Ma) formed during the Sveconorwegian orogeny. Scale in lower right hand corner indicates 200 m.

2 Field areas

2.1 Løkjelsvatn

In the following section the regional and local geology related to Løkjelsvatn power plant will be presented.

2.1.1 Regional geology

The area surrounding Løkjelsvatn power plant consists of a bed rock made up of amphibolitic gneiss formed during the sveconorwegian orogeny (1600 - 1000 Ma). On top of the lower bed rock is a caledonian nape consisting of phyllite with sporadic quartz lenses, in places garnet bearing (541 - 458.4 Ma)(described from information given in the online geological maps provided by NGU (Norwegian geological survey)). A map of the area is shown in Fig.3.

The rock mass wasn't classified during this thesis, but investigations through visual observation and knocking with a geological hammer was done. When the tunnel contour was hit with a hammer the majority of the sections had a hollow sound, indicating fractures and openings behind the tunnel wall. This, together with the observed fractures, yielded an estimated poor rock mass quality. No geological reports or in depth geolgical information was found online regarding the geology of the project area.

2.2 Nordøyvegen

In the following section the regional and local geology related to the Nordøyvegen road construction project as well as the tunnel geology will be presented.

2.2.1 Regional geology

Ålesund municipality is situated within the western gneiss region of Norway, a large geological unit between Sogn and Nord-Trøndelag. During the Caledonian orogeny (400 Ma.) Precambrian rocks (1700 - 1500 Ma.) along the western edge of the Baltic shield were buried and metamorphosed, which resulted in a variety of lithologies including granitic gneiss and migmatite with lenses of amphibolite and mica-rich gneiss/schist. Also scattered across the region are occurrences of gabbro (1650 - 1200 Ma.) (Ramberg et al. 2013).

2.2.2 Local geology

The geology of the different islands is shown in Fig.4. Hestøya is dominated by garnet-rich gabbro, Haramsøya is dominated by granitic- and dioritic gneiss with areas containing mica-schist, amphibolite and meta-arkose. Suløya/Flemsøya and Fjørtofta both consist of migmatic- and dioritic gneiss with the former island also containing granitic gneiss with eclogite lenses. And Harøya is primarily made up of migmatic gneiss. (Text is formulated based on map in Karlsson & Grob (2017) as shown in Fig.4).

2.2.3 Weakness zones

Magnetic- and bathymetric surveying have been conducted in the area around Nordøyvegen by NGU on behalf of the Norwegian Public Road Administration (NPRA).
From the magnetic survey (Fig.5) three weakness zones/faults were identified which might cause problems during excavation; these zones are assumed to belong to the Møre - Trøndelag fault zone (MTFZ). One of these zones intersect the Nogvafjord tunnel and the other two intersects the Fjørtoft tunnel. The bathymetric survey didn't uncover a lot of structures due to sea floor sediments, but the observed irregularities are interpreted to correlate with the weakness zones from the magnetic survey. Seismic velocities of the different weakness- /fault zones are interpreted to represent poor rock mass quality (Dehls et al. 2011).

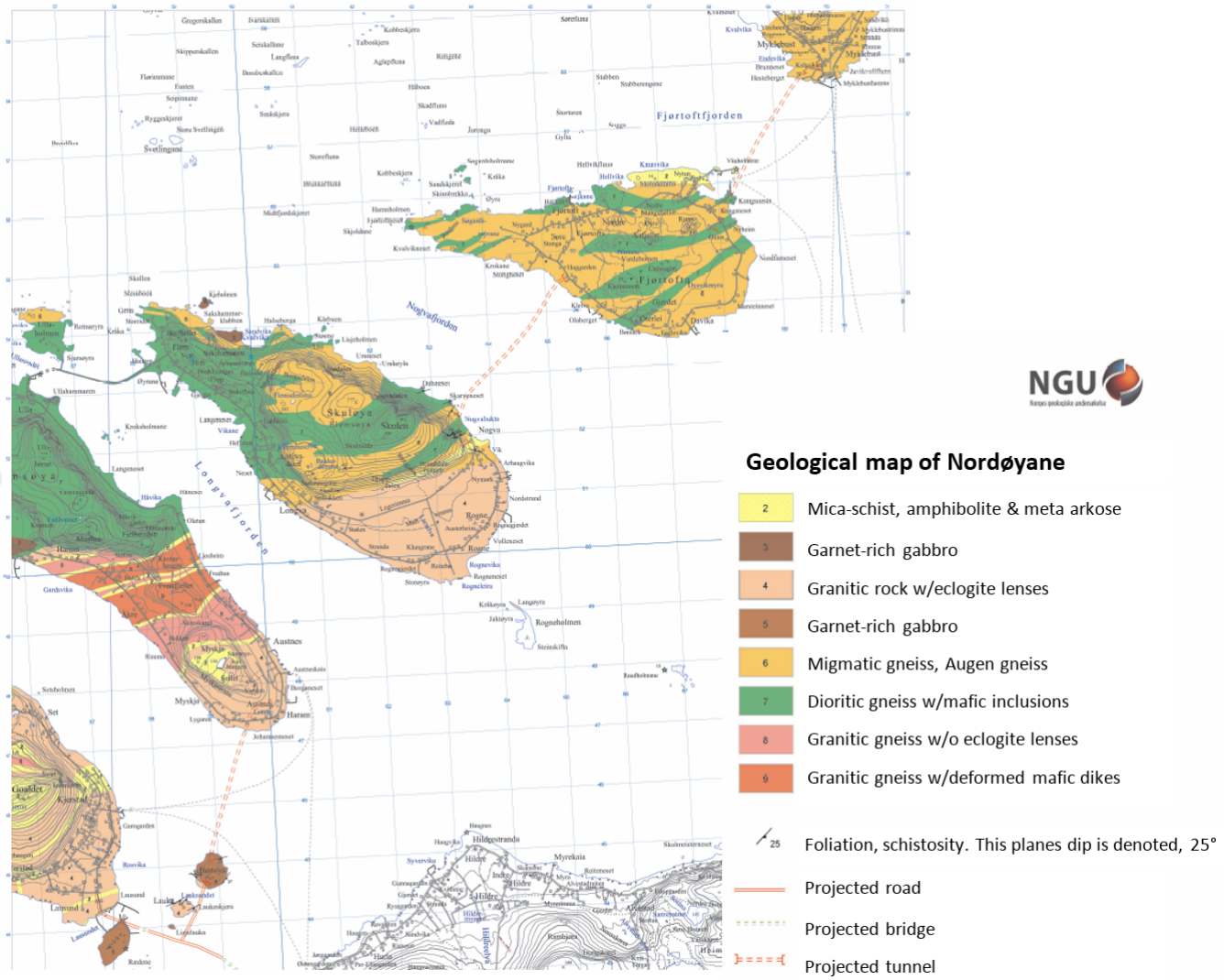

Figure 4: Geological map of Nordøyane, Møre og Romsdal. Translated from Karlsson & Grob (2017). Map initially based on data from Terry & Robinson (2003) according to Ganerød & Lutro (2011). Scale couldn't be added but each square represents 1 km.

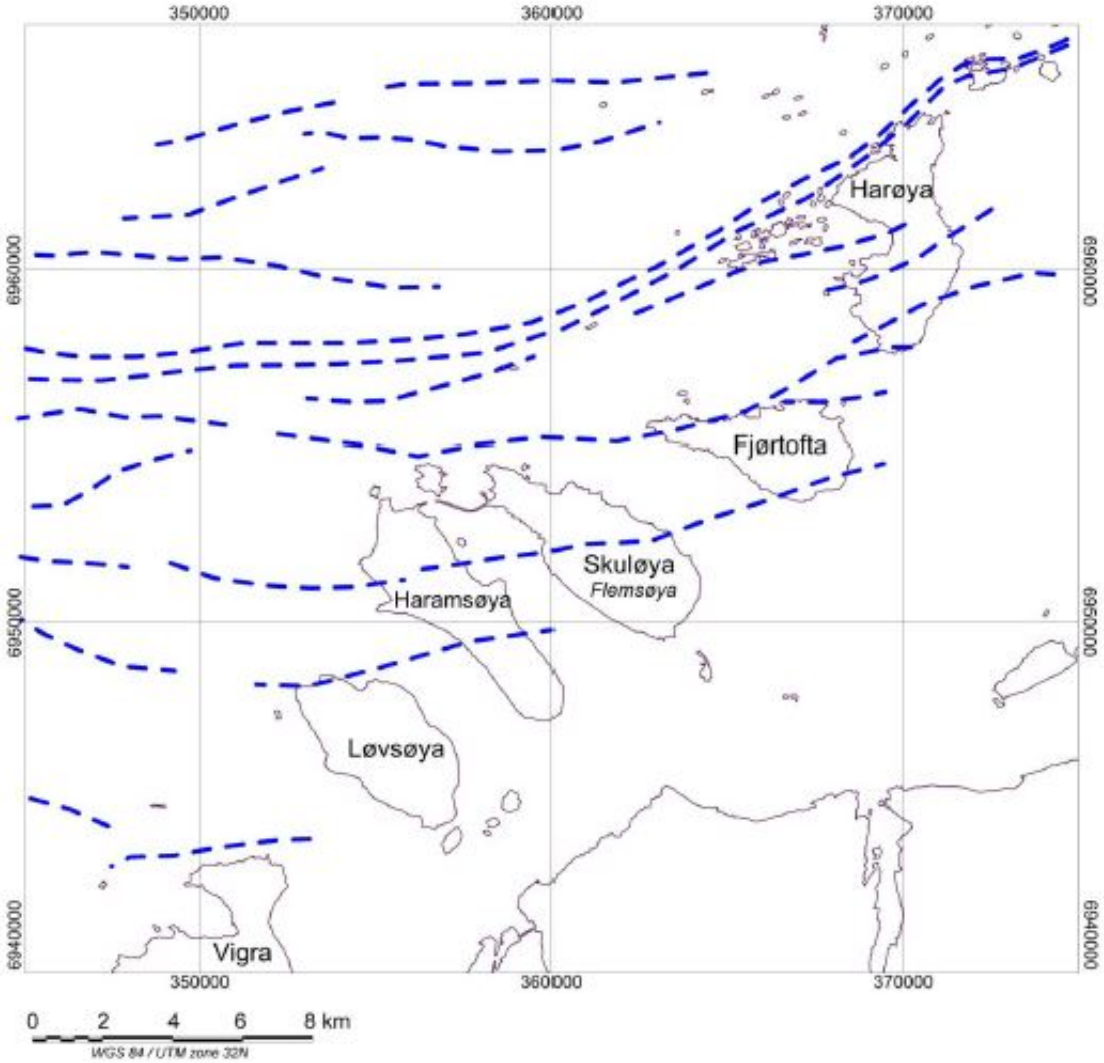

Figure 5: Weakness- /fault zones near Nordøyane interpreted from magnetic data by Dehls et al. (2011).

2.3 Fjørtoftfjord sub-sea tunnel

The AE-measurements was supposed to be conducted at the Fjørtoftfjorden sub-sea tunnel. Upon completion the tunnel will be 3680 meters long with it's deepest point at 118 meters below sea level (Karlsson & Grob 2017). In the following section the rock mass quality, geology and hydrogeology of the tunnel will be presented.

2.3.1 Tunnel geology

The following information is gathered from the geological report created by The Norwegian Public Roads Administration (NPRA) Karlsson & Grob (2017) and is briefly presented here.

2.3.1.1 Rock mass quality

The rock mass quality for Fjørtoftfjorden sub-sea tunnel is generally good with 73 - 85% of the tunnel having a Q-value greater than 4 (fair quality rock mass). No tunnel length is located in a exceptionally poor rock mass quality (Q<0.01) and only 0.1% of the tunnel is classified as having extremely poor rock mass quality (Q:0.01 - 0.1). See Fig.6 for a summary of rock mass quality as it relates to percentage of tunnel length. The difference in percentage is related to the classification being based on logged core-data and seismic data; both of which give different estimates (Karlsson & Grob 2017).

2.3.1.2 Major rock types

The major rocks along the tunnel axis are different types of pre-cambrian gneisses which contain folded or straight 1 - 5 cm thick layers of banded gneiss. The rocks at the cut located at Fjørtofta was shown to be a "dioritic to migmatic gneiss with mafic enclosures". The same migmatic gneiss was observed in the vicinity of the cut at Myklebust as well. Here it had smaller mafic enclosures (estimated 0.5 - 5 m in field, 10 m from core logging) with large garnet crystals, interpreted as eclogite. In addition to the gneisses in the area some Amphibolite consisting of amfibole and plagioclase with eclogite, biotite and carbonate as accessory minerals was mapped. Mica-schist, amphibolite and arkose could be present in the Fjørtoftfjord sub-sea tunnel between Peg.31845 - 31992 based on the geological map (Fig.4 showing these rock masses at the north end of Fjørtofta). Some pegmatite dikes consisting of alkali feldspar and plagioclase were also mapped in the core log data.

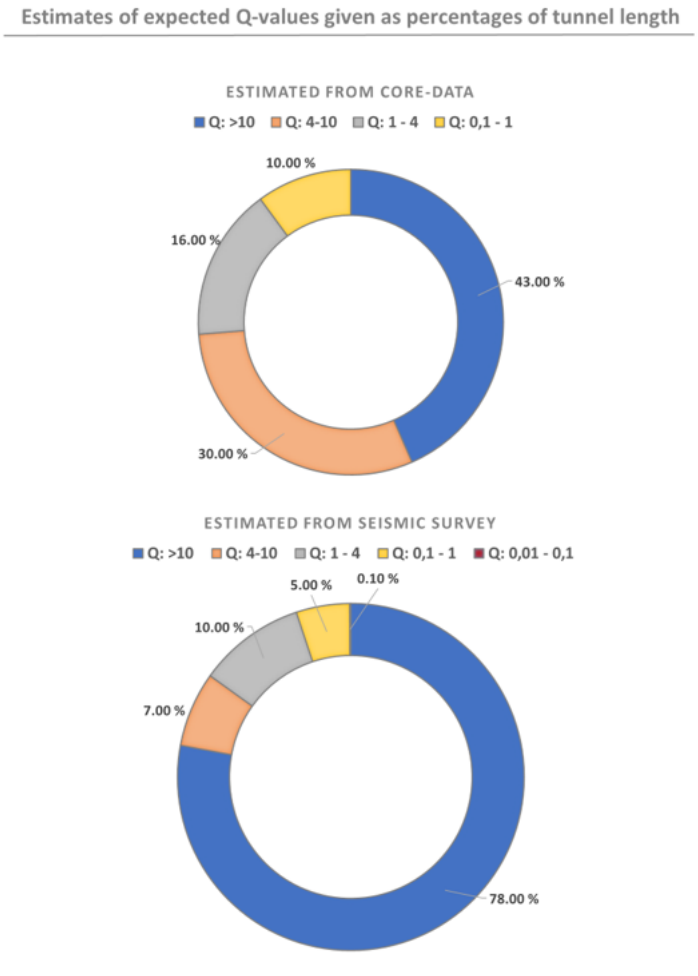

Figure 6: Percentage of tunnel situated within different rock mass qualities for the Fjørtoftfjorden sub-sea tunnel. Most of the tunnel (73 - 85%) is situated in rock classified as having a fair rock mass quality (Q<4), and only 0.1% is classified as poor rock mass quality (Karlsson & Grob 2017).

2.3.1.3 Structural geology

There exists a number of structures within the field area that can interfere with the tunnel stability, the most important for Fjørtoftfjorden sub-sea tunnel being the two fracture sets (S1 and S2) and the foliation plane (F1). S3,S4 and S5 isn't as widespread at Fjørtofta/Myklebust as it is on Hestøya. In addition to these structures there exists sporadic fractures of lesser extent. The rose diagrams for the structures dominating Fjørtoftafjorden sub-sea tunnel is shown in Fig.7.
Using the right-hand rule the strike-dip of S1 is shown to be 31°/31° SE at Fjørtofta and 40°/64° SE at Myklebust. For S2 strike-dip at Fjørtofta and Myklebust is 161°/78° SW and 176°/85° SW, respectively. The F1 structure varies quite a lot, at Fjørtofta it ranges from: 53°/90° SE - 88°/85° S and 266°/66° N. At Myklebust the F1 structure has a strike-dip of 260°/54° N.

S1 and S2 both has a fracture distance ranging from the dm scale to 1-2 meters. The waviness of the fractures is planar to slightly undulating. And the fracture roughness is classified as smooth to slightly rough. The fracture filling was found to consist of epidote, graphite and clay minerals, and partial slickensides were observed at some of the weakness zones.

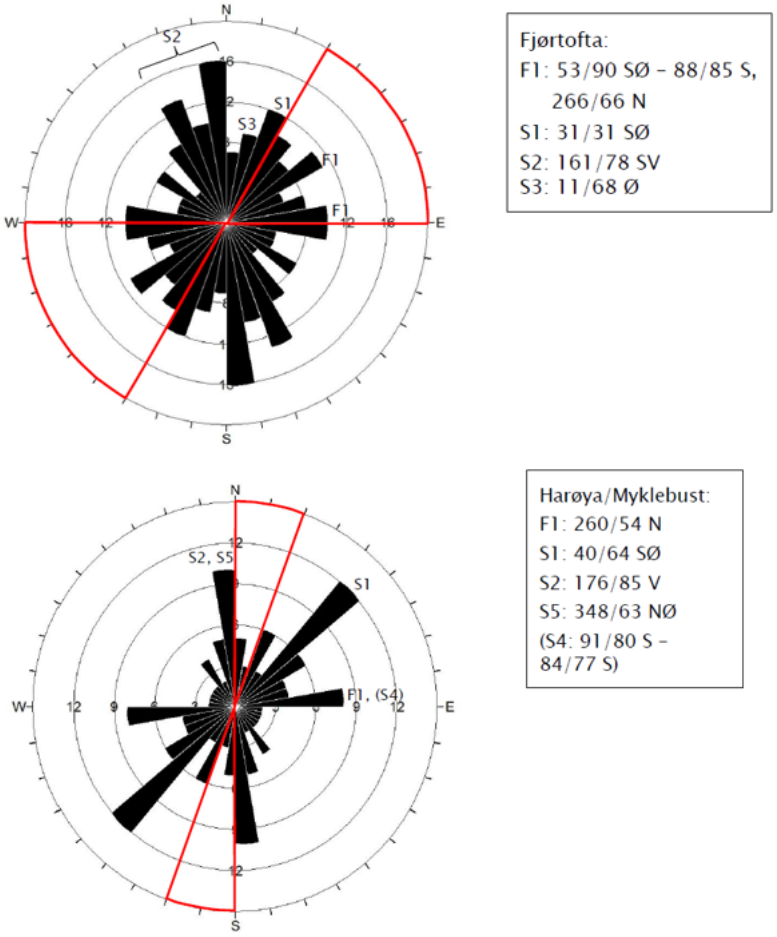

Figure 7: Folitation planes (F) and fracture sets (S) mapped for the cut at Fjørtofta and Myklebust, the most prominent feature at both areas is the S1 and S2 fracture-sets. Red indicates the axis of the tunnel. Source: (Karlsson & Grob 2017).

2.3.1.4 Hydrogeology

The rock mass in the project area is generally a stiff rock (gneiss) which contain a varying degree of open- and water bearing fractures. Most of the leakage is estimated to occur close to the weakness zones (seismic velocity of 3500 m/s - 4500 m/s), indicating that the rock mass is a typical fracture aquifer.
The measured water loss in the borehole from Myklebust was in the range of 0.07 - 0.25 l/m/min measured in the sub-sea surface of the borehole. This indicates that the general water loss is low with the main source of leakage being a few water bearing fractures- /weakness zones.
The leakage requirements for the tunnel is moderate with a maximum allowable inflow of 200 l/min/km tunnel (Karlsson & Grob 2017).

2.3.2 Test-section Fjørtoftfjorden sub-sea tunnel

The in-situ AE monitoring of pre-excavation grouting was supposed to be conducted at peg number 33397 which is located within a gneiss with no pre-defined weakness zones surrounding it. Based on the pre-excavation surveys conducted this section of tunnel was estimated to be situated in the rock mass class A/B (slightly fractured) with a Q-value greater than 10 (Karlsson & Grob 2017). Indicating competent rock which should in theory have been beneficial for AE-monitoring, had this been conducted.

3 Theory

3.1 Hydraulic fracturing stress measurements

Fracturing caused by a pressurized liquid is commonly denoted as "hydraulic fracturing" (HF). HF, together with Hydraulic testing of pre-existing fractures (HTPF), is often utilized to determine the in-situ rock stresses for a measured rock mass (Haimson & Cornet 2003).
The suggested method for conducting a HF/HTPF-test is given by ISRM as indicated in Haimson & Cornet (2003). The method consists of isolating a test-section of a borehole using two rubber packers, these packers are then pressurized to firmly attach them to the borehole wall. Subsequently a hydraulic fluid is pumped with a constant flow rate into the sealed off section, this gradually increases the internal pressure until a hydraulic fracture is formed (or in case of HTPF a pre-existing fracture is reopened). The pumping is then stopped and the internal pressure is allowed to dissipate, the measured pressure in this portion of the pressure graph is used to calculate the shut-in pressure through various approaches. After several minutes the internal pressure is fully released before the test section is resealed, pressurized and tested again using the same method and flow rate as before.
During the fracturing process the pressure within the packers is constantly two Mpa greater than the pressure within the test section, this is to ensure that the packers are kept in place. The principal stress state in the rock mass is related to the orientation of the HF and the magnitude of the in-situ stresses are calculated from key pressure parameters obtained from the pressure-time logs (Haimson & Cornet 2003).

3.1.1 Pressure parameters

From a HF-test the key pressure parameters obtained are; breakdown pressure (P_b), reopening pressure (P_r) and shut-in pressure (P_s). These pressures are found by analysing the pressure-time graphs, an example of which is shown in Fig.8. P_b is equal to the peak pressure from the first pressure cycle. P_r is found using the pressure-time graph from the second and/or third pressurization cycle and is the point on the ascending pressure line where the slope begins to deviate from the ascending pressure line in the first cycle. P_s is the pressure measured when a fracture is closed after opening, different approaches exists for determining the shut-in pressure and it is advisable to apply more than one when quantifying P_s given the importance of the parameter (Haimson & Cornet 2003). These approaches will not be covered in this thesis, for a detailed description the reader is directed to the article by ISRM regarding HF/HTPF: Haimson & Cornet (2003).

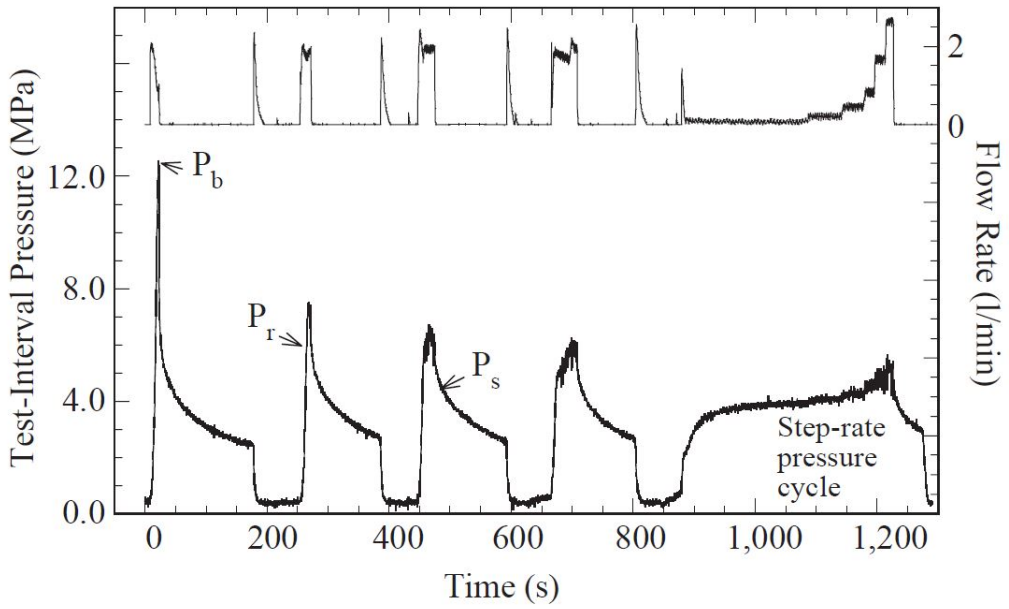

Figure 8: Pressure-time graph from a conducted HF test. Pb indicates breakdown pressure, Pr reopening pressure and Ps indicates shut-in pressure (Haimson & Cornet 2003).

3.2 Hydraulic Jacking

In Norwegian tunneling water control is mainly achieved through the use of high pressure pre-excavation grouting to ensure the formation of a low permeability zone surrounding the tunnel. The objective is to create a tunnel that is "tight enough for it's purpose", meaning that the goal is to achieve a maximum allowable inflow rate as oppose to a waterproof tunnel.

The use of high pressures (100 bar) is common when the rock mass is of good quality and the grouting cement used is OPC (ordinary portland cement). With the use of micro fine cement (MFC) a lower pressure of 50 - 70 Bar above the in-situ water head can be used (Grøv & Woldmo 2012).

The pressure used during pre-excavation grouting in Norway might seem excessive, but as noted by Strømsvik (2019) it needs to be viewed in conjunction with the favorable geology in Norway. The geology of Norway is generally made up of hard crystalline, self bearing rock as the majority of weathered rocks were removed during the last glacial period (Strømsvik 2019). The Norwegian grouting methodology is developed through decades of experience in road- and railway tunnels, sub sea tunnels and hydroelectric power projects. So the reason for the high grouting pressures used is a combination of experience and favourable geology (Strømsvik 2019), as well as the results obtained in the research project "Tunnels for the citizens" (Strømsvik et al. 2018).

One consequence of high-pressure grouting is that it increases the likelihood of hydraulic jacking being initiated. Hydraulic jacking (HJ) is the result of pressure increase within a fracture leading to dilation perpendicular to the fracture surface. The onset of hydraulic jacking occurs when the grouting pressure within the fracture is larger than the normal force acting on the fracture surface (Strømsvik et al. 2018). In the following section the concept of hydraulic jacking will be briefly presented together with it's consequences and how it is detected using today's practice.

3.2.1 Elastic and ultimate jacking

In Rafi & Stille (2014) the HJ process is divided into elastic- and ultimate jacking. Elastic jacking occurs when the grouting pressure (P_g) is high enough to carry the load of the overlying rock mass resulting in load bearing asperities no longer being in contact. At this point Rafi & Stille (2014) argues that the deformation is elastic and reversible, however, due to the presence of grout within the fracture it's unlikely to revert to the original position. Mathematically the grouting-pressure needed for elastic jacking can be expressed as:

$$1/3 < \frac{P_g}{3\rho g h} < P_{ultimate}, \tag{1}$$

where P_g is grouting pressure, ρ is the density of the rock mass, g is acceleration of gravity, h is the thickness of the overburden and $P_{ultimate}$ is the grouting pressure needed to cause ultimate jacking, after which the the overlying rock mass is lifted to an irreversible extent (Rafi & Stille 2014). For ultimate jacking to occur a grouting pressure of three times the overburden is needed, for mainly horizontal fractures the following equation can be applied to calculate the pressure where ultimate jacking is initiated:

$$P_n \leq P_{n,ultimate} = 1 + \frac{1}{I_n} + \frac{1}{3I_n^2}, \tag{2}$$

Where P_n is the normalized pressure ($P_g/3\rho g h$), h is the depth between ground surface and the jacked fracture, ρ is the density of the rock, I_n is the normalized grout penetration which is the relationship between grout spread and and depth of the fracture; $I_n = I/h$.

Jacking, in addition to pressure, is also governed by the spread of grout within the fracture. A consequence of this is that when grouting is conducted at a constant pressure the fracture will continue to be jacked with increasing grout spread (Rafi & Stille 2015). The deformation/change in aperture along the fracture can according

to Gothäll & Stille (2009) be quantified as:

$$\Delta a(r) = \frac{4}{3}\frac{P_e}{E}\frac{r_c^2(1-\nu^2)}{r}, \tag{3}$$

Where P_e (excess pressure) is the difference between grouting pressure P_g and critcial pressure P_c (i.e. pre-stresses on the fracture). E is the elastic modulus of the rock mass, r_c is the radius of the area over which P_e acts, ν is the Poisson's ratio and r is the distance from the borehole intersection (Gothäll & Stille 2009). As a fracture becomes elastically jacked (i.e. filled with grout) the grout will help carry some of the load. This will redistribute the load acting on the fracture, potentially leading to fracture deformation outside of the grouted zone (r > r_c) (Rafi & Stille 2015).

3.2.2 Consequences of hydraulic jacking

There are both negative and positive consequences regarding hydraulic jacking of fractures, in some projects the positive might outweigh the negative and vice versa. According to (Strømsvik 2019) the decision on whether HJ should be avoided or not is project specific and it is argued that the project owner should be made aware of the consequences. In this section the negative consequences of HJ will be discussed followed by the positive.

3.2.2.1 Negative consequences

Reduced penetration distance and increased grouting time
A rule of thumb given by Rafi & Stille (2015) is that "elastic jacking reduces penetration distance" meaning that when jacking happens a significant amount of grout is consumed close to the borehole. This in turn reduces the amount of grout available to penetrate further into the fracture. The total injected volume after jacking can be estimated using the following equation:

$$V_{inj} = \pi(\frac{4}{3})P_e r_c^2(\frac{1-\nu^2}{E})(2I - r_c) + \Delta V_b, \tag{4}$$

Where the symbols are the same as in Eq.3 except for ΔV_b which represents the volume of the initial fracture (i.e. the volume of a disc with radius l and thickness b) and I which represent the grout spread, this formula is a conjunction of Eq.5 and Eq.6 in Rafi & Stille (2015).

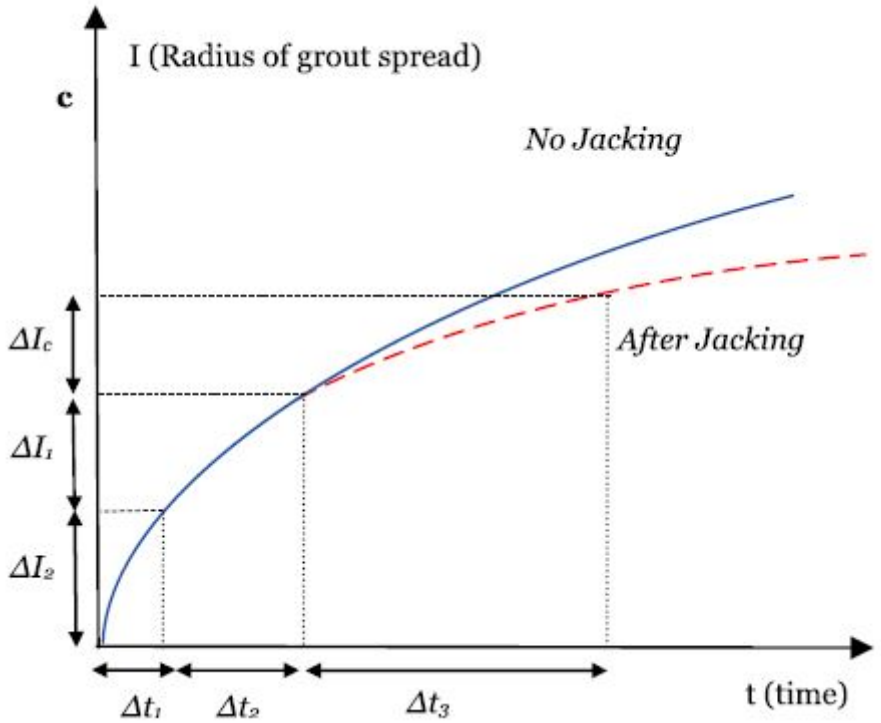

Figure 9: Grout penetration (i.e. volume increase) as it correlates with time increase due to jacking (Δt_3). ΔI_c is the reduction in grout spread due to jacking of the fracture (Rafi & Stille 2015).

Further the increase in time due to an increase in volume can be estimated using:

$$t = \frac{\Delta V_{inj}}{Q}, \tag{5}$$

Where Q is the grout flow, the increase in time due to jacking is shown graphically in Fig.9 (Rafi & Stille 2015).
Strømsvik (2019) noted a time increase from HJ equal to 88% in holes grouted with OPC, and 123% in holes grouted with MFC. This indicates that when HJ occurs more time is needed before the grouting work is deemed sufficient.

Increased grout consumption
Six tunnels were studied by Strømsvik (2019) to figure out the "significance of hydraulic jacking for grout consumption". The study found that HJ was related to a consumption increased of 79% (when using OPC) and 141% (when using MFC), as compared to holes where no jacking occurred. The measure used was l/m hole and OPC showed a slightly higher grout consumption in HJ holes (52 l/m hole) compared to MFC (41 l/m hole) for these specific projects (Strømsvik 2019).

Increased cost

Grouting is a costly process as can be seen from Fig.10. Stricter inflow requirements or limit residual inflow rate (LRIR) is associated with a high grouting cost. An inflow rate of $>$ 10 liters/minute/100 m tunnel increase the excavation cost by 50 - 70 % (Grøv & Woldmo 2012). And hydraulic jacking is strongly correlated with an increase in grout material consumption and grouting time (Strømsvik 2019), both of which will add additional costs to the already expensive grouting process.

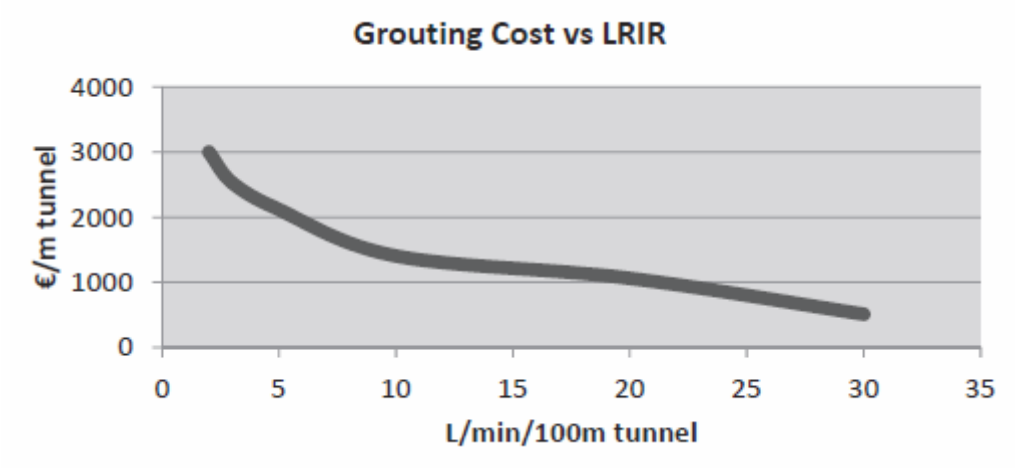

Figure 10: Cost (in euro) of pre-excavation grouting as it relates to limit residual inflow rate; LRIR (l/min/100 m tunnel). The price correlation isn't linear and a stricter inflow requirement is associated with higher costs (Grøv & Woldmo 2012).

Reduced sealing efficiency

When a fracture is jacked it's transmissivity is increased to T_{jacked} following the equation:

$$T_{Jacked} = \frac{\rho_w g}{12\mu_w}(b + \Delta a(r))^3 \tag{6}$$

where ρ_w and μ_w is the density and viscosity of water, respectively. g is the acceleration of gravity, b is the initial aperture size and $\Delta a(r)$ is the aperture change in radius r into the fracture from the borehole intersection, same as in eq.3 (Rafi & Stille 2015).

If a fracture is elastically jacked, and the packer is left in the borehole, the elastic deformation outside the grouted zone (see section.3.2) might remain permanently un-grouted (Rafi & Stille 2015). If the packer is removed/opened the elastic energy exerted by the grout on the rock mass might revert back, squeezing the grout further into the fracture, possibly increasing the grout fill ratio (Gothäll & Stille 2009).

Uplift

If the ultimate jacking limit is reached during grouting of a shallow, horizontal fracture in low stress conditions uncontrolled uplift of the overlying rock mass might be initiated (Gothäll & Stille 2009). Such an event would either fail along the existing block boundaries or if the rock mass is intact it might potentially fail according to the schematic shown in Fig.12.

As indicated in Fig.12 grouting of vertical fractures may potentially cause instabilites as well, especially if there exists a excavation close to the grouted hole. This has the potential to be a working hazard for tunnel workers at, or behind, the face (Gothäll & Stille 2009).

In Fig.11 a graphical representation of the k-ratio (σ_h/σ_v) with depth is shown Brown & Hoek (1978), the graph shows how horizontal stresses generally are higher closer to the surface compared to vertical stresses. This helps explain why horizontal fractures are more prone to jacking compared to vertical ones, for the simple reason that the horizontal stresses generally are higher close to the surface (Rafi & Stille 2014). This means that a grouting pressure large enough to cause jacking of horizontal fractures might not affect vertical fractures at all.

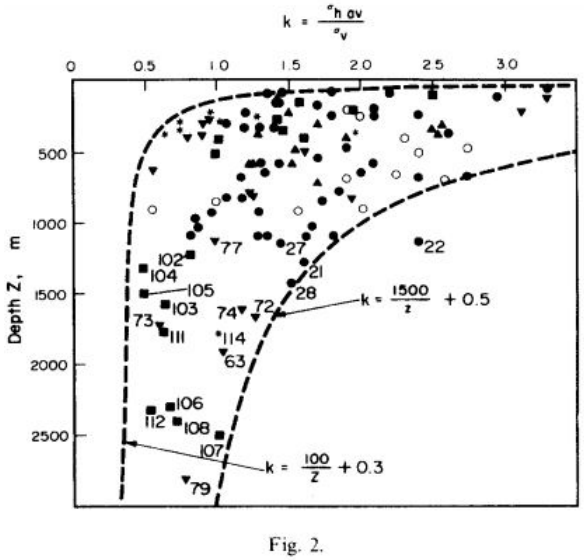

Fig. 2.

Figure 11: k-ratio (σ_h/σ_v) for different depths (m). The figure is created by plotting stress measurement data from around the world (Brown & Hoek 1978).

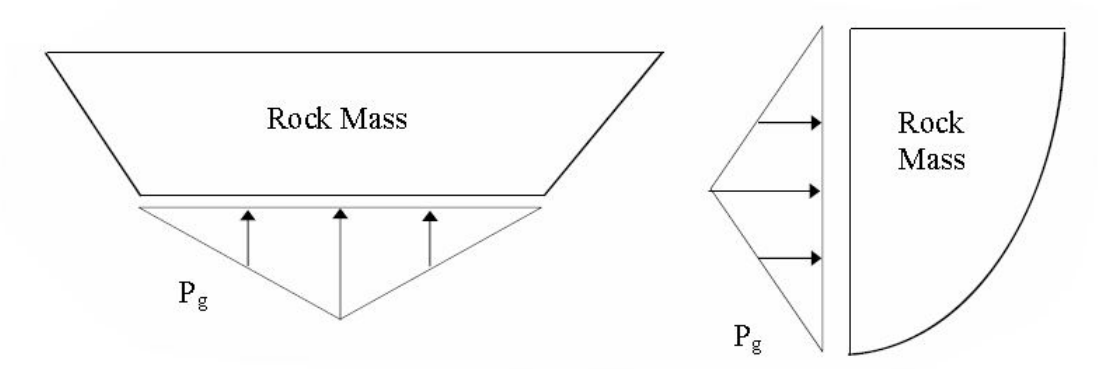

Figure 12: Failure at ultimate jacking pressure indicating shape of potential uplift (Yaghoobi Rafi 2013).

3.2.2.2 Positive consequences

Improved penetrability

Fracture deformation might be beneficial if it leads to increased grout penetrability, which may happen according to Rafi & Stille (2015).
Ashikhmen & Pronina (2001) noted that the penetrability of grout into finer fractures is directly related to the diameter of the largest particles. If the largest particles has a diameter close to/or greater than the aperture size the particles will block finer particles from entering the fracture. Large particles smaller than the aperture can still cause blockage. This might happen if multiple large particles are in contact, then an arching effect can occur as shown in Fig.13 effectively blocking the aperture opening (Ashikhmen & Pronina 2001). In this case jacking of the fracture would improve the grout penetrability by allowing larger particles to flow further into the fracture. However, Stille et al. (2012) states that the jacking will affect the largest fractures the most, with smaller fractures being to some degree closed. This means that the improved penetrability is only the case for larger fractures since the aperture size, and in turn penetrability, will be reduced for the smallest fractures. Therefore jacking is only viewed as positive if the target is to seal the largest fractures, if smaller fractures need to be sealed then jacking could have the opposite effect, as the smallest fractures might remain unsealed (Stille et al. 2012).
Eriksson & Stille. (2003) introduced the terms "critical aperture ($b_{critical}$)" indicating the aperture through which an infinite amount of grout can pass and "minimum aperture (b_{min})" i.e the aperture where no grout will pass through. Jacking a fracture further than $b_{critical}$ won't yield any additional benefits, and $b_{critical}$ is "rarely larger than twice the minimum aperture" (Fig.14) (Rafi & Stille 2015). This means that small amounts of jacking potentially could be beneficial.

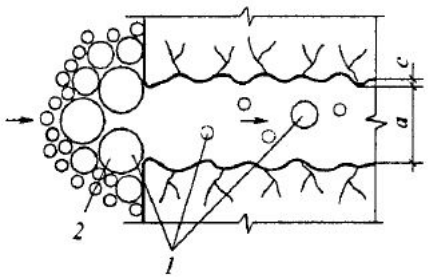

Figure 13: Illustration of arching effect caused by larger cement particles in grout, reducing the penetrability into finer fractures. a is the opening of the fissure, c is the roughness (Ashikhmen & Pronina 2001).

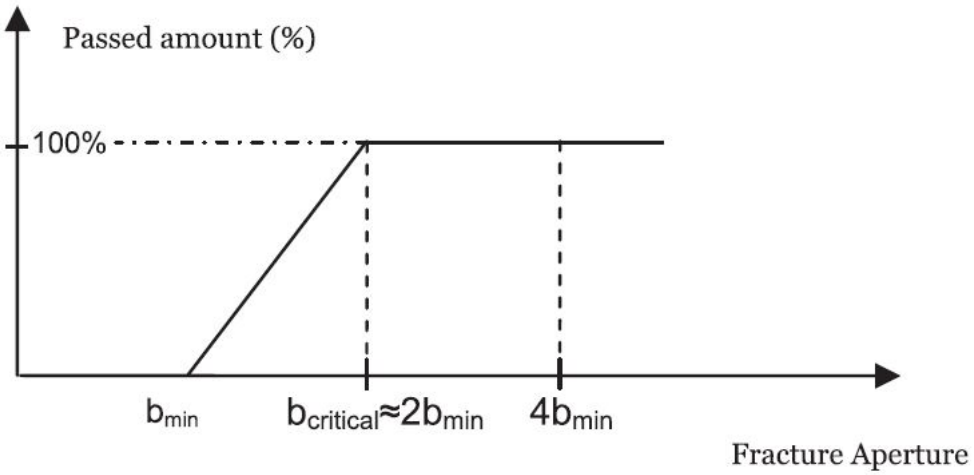

Figure 14: Amount of grout passed as it relates to aperture size. Jacking beyond the critical aperture ($2b_{min}$) won't improve penetrability (Rafi & Stille 2015)

.

3.2.3 Pressure distribution during grouting

During grouting the pressure is often assumed to dissipate in a linear fashion from the borehole and towards the grout front (e.g. Rafi & Stille (2015), Haugsand et al. (2019)), as shown in the simplified fracture geometry in Fig.15. A somewhat linear pressure distribution was found numerically by Skjetne & Mo (2016),these findings are reported in the final report from "TIGHT" (True Improvement in Grouting High pressure Technology for tunneling), working package Nr.4 (Grøv et al. 2020).
This cone shaped pressure distribution has implications for hydraulic jacking of fractures. Generally, for horizontal fractures, the grouting pressure P_g needs to be at least three times the initial loading pressure P_i to be able to cause uplift of the rock mass above the fracture (Jalaleddin et al. 2013). Another consequence is that the greatest aperture change occurs where the pressure is highest, meaning close to the grouting hole (Fig.16) (Zou et al. 2018). The same change is noted in Rafi & Stille (2015) where fracture volume is used instead of aperture change. And in most cases jacking will start at the bore hole intersection (Gothäll & Stille 2009), which is seen as fortunate if AE-monitoring is conducted during pre-excavation grouting in the future. As the sensors will be placed close to the borehole, meaning less attenuation of the signal. More on this in section.3.3.6.

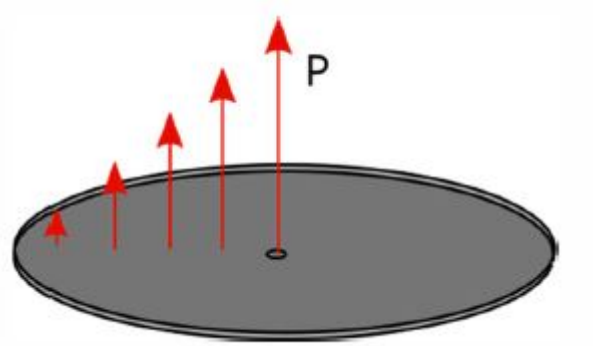

Figure 15: Pressure distribution within a simplified fracture geometry (modified by Haugsand et al. (2019) from figure in Brantberger et al. (2000)).

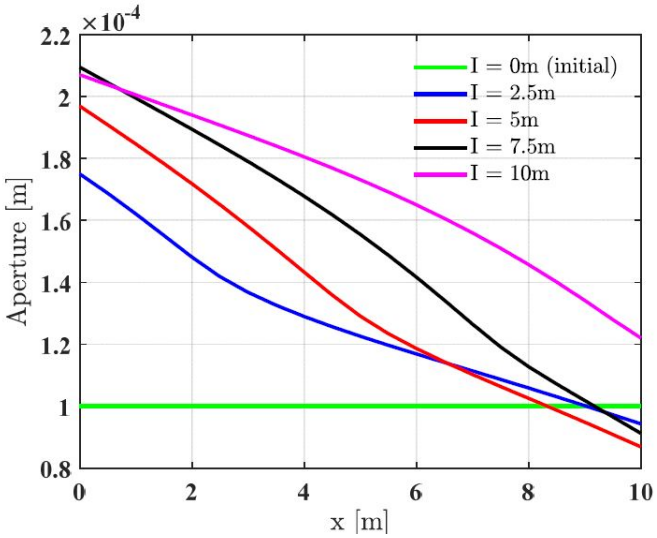

Figure 16: Aperture change caused by hydraulic jacking of a fracture given different penetration lengths of grout ranging from l=0m, 2.5m, 5m, 7.5m and 10m (Zou et al. 2018).

3.2.4 HJ detection

Today's practice of hydraulic jacking detection mainly involves analysing grouting rig data for changes in pressure and flow rate. Lombardi & Deere (1993) analysed the relationship between flow (Q) and pressure (P), by dividing flow with pressure the acquired Q/P-ratio can be used to detect spikes in graphs associated with HJ. When analysed together with flow and pressure this ratio is a good tool to detect HJ, see Fig.17. The Q/P ratio is seen to decrease as the resistance within the fracture increases, the pronounced peak is related to hydraulic jacking as pressure is seen to decrease and flow is increasing prior to reaching the peak due to hydraulic jacking (Strømsvik et al. 2018).

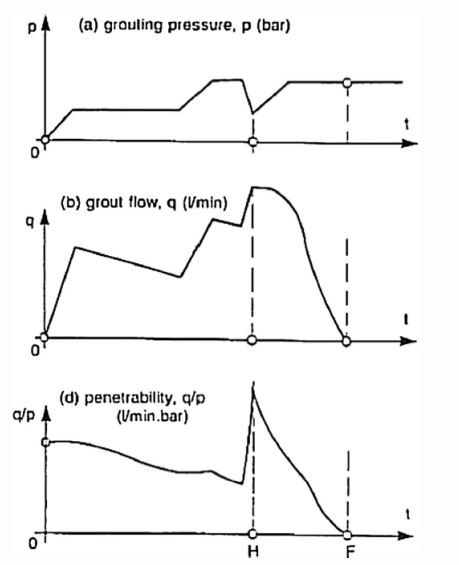

Figure 17: From top to bottom: Pressure, flow and Q/P ratio during hydraulic jacking/fracturing (Lombardi & Deere 1993).

Due to the high grouting pressure in Norwegian tunneling the Q/P-ratio by Lombardi & Deere (1993) was insufficient at detecting HJ since a large pressure drop during low flow rates didn't significantly change the Q/P-ratio according to Strømsvik et al. (2018). To successfully interpret the relationship between pressure and flow during high pressure grouting Strømsvik et al. (2018) developed the Pressure Flow index:

$$PF\,index\; =\; 0.9\,min\,/\,l \times Q_v - \frac{0.9 \times P}{1\,bar} + 81, \tag{7}$$

where Q_v represents the flow rate in l/min and P represents the grouting pressure in bar. The equation is modified to create a dimensionless value. This index was implemented in a computerized screening algorithm used to successfully detect potential HJ-events from grouting rig logs (Strømsvik et al. 2018).

Another approach is presented in Rafi (2014) based on the Real Time Grouting Control (RTGC) method developed by Gustafson & Stille (2005). By comparing back calculated flow predictions with the actual recorded grout flow Rafi (2014) shows how a deviation between the two could indicate hydraulic jacking (see Fig.18). The problem with this approach is that the same deviation can be the result of unreliable input data based on wrong assumptions regarding grout properties or aperture size (Rafi 2014).

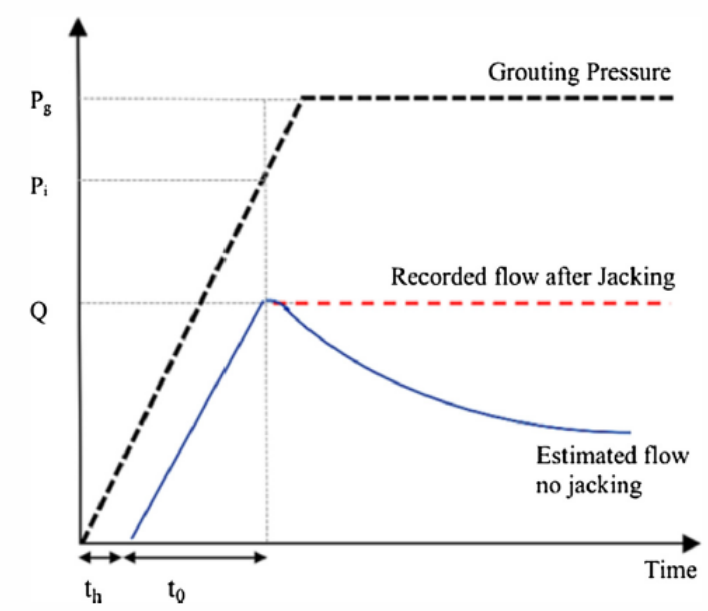

Figure 18: Figure showing the deviation in recorded- and estimated flow associated with hydraulic jacking.(Rafi 2014).

3.2.4.1 False positive HJ interpretation

There are a number of events that occur within a rock mass that can give the same pressure and flow pattern as HJ, this leads to the possibility of false positive hydraulic jacking interpretation. According to (Strømsvik et al. 2018) some of these events are:

- Grout starting to flow after standstill
- Rapid increase/decrease in flow by the operator
- Fluctuations caused by the pumping cycle on the rig
- Erosion of infilling along the fracture walls, or bursting through fracture infilling blocking the flow path (e.g. clay plug)
- Using low pressure when grouting an open fracture system

  (Strømsvik et al. 2018)

To successfully detect HJ when using the RTGC-method assumptions regarding the spread of grout and fracture deformation are required (Rafi 2014). If one, or both, of these parameters are based on the wrong assumption then HJ might be interpreted where no real HJ took place, or vice versa.

3.3 Acoustic emission

3.3.1 Acoustic emission sensors

In the following section a brief introduction to how AE-sensors work will be given. An acoustic emission sensor is made-up of a piezoelectric crystal placed inside a faraday cage. The sensors from physical acoustics has a piezoelectric element using a ceramic plate made out of Lead Zirconate Titanate (PZT). These piezoelectric crystals work by converting mechanical energy to electrical energy that can then pass through the cables and into the SHM-system. These sensors also have a built in pre-amplifier within the sensor casing that is mechanically attached to the crystal-plate (Mistras group 2017). A schematic of an AE-sensor without a built in pre-amplifier is shown in Fig.19.

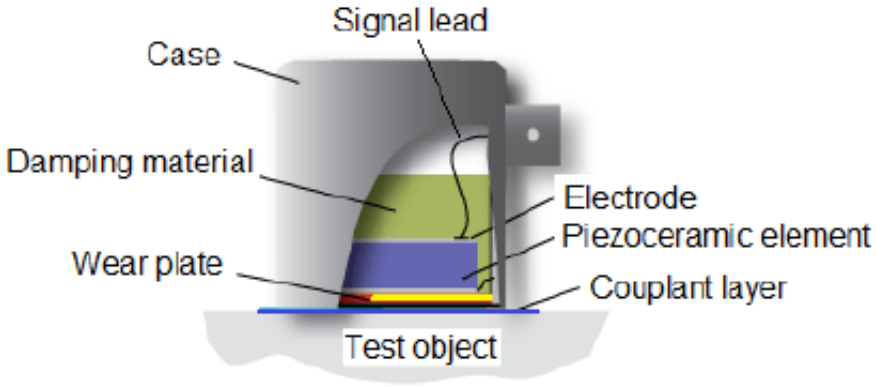

Figure 19: A schematic figure of the interior of a typical PZT-sensor. Note this sensor is not showing built in pre-amplifier. Source: (Svečko et al. 2013).

3.3.2 HF detection using AE

In-situ acoustic emission monitoring have successfully been used to verify hydraulic fracturing and/or hydraulic jacking during: injection of supercritical CO_2 (Ishida et al. 2017), hydraulic fracturing measurements (Zang et al. 2016) and during grouting of urban soil tunnels (Huck & Koerner 1981). This is far from every previous use of AE-sensors in rock engineering, for an extensive list the reader is referred to the article by Feng et al. (2019). In the following section the articles mentioned here will be briefly summarized with regards to their use in HF/HJ detection.

3.3.2.1 Injection of supercritical CO_2

To test the effect of fracturing fluid viscosity on HF Ishida et al. (2017) initiated a HF by injecting supercritical CO_2 into a rock mass while monitoring the process using AE-sensors. In this small scale experiment four holes were drilled one meter from the injection hole, and each hole contained four AE sensors spaced 0.6 m to 0.7 m apart, see Fig.20. The sensors used (AE703SW) had a resonance frequency of 70 kHz and were created by Fuji Ceramics corp. The pre-trigger was at 1 volt, pre-amplifier gain was set at 30 dB and the signal was filtered using a 20 - 200 kHz band-pass filter and the sample length was 2048 (Ishida et al. 2017).
The conclusion from the study was that the AE distribution showed the formation of two vertical hydraulic fractures following the break-down pressure (BD). After the BD, during a period of no pressure increase, the AE distribution extended perpendicular to the formed HF, these AE-events were interpeted to be the result of CO_2 migrating into pre-existing cracks in the rock mass Ishida et al. (2017).

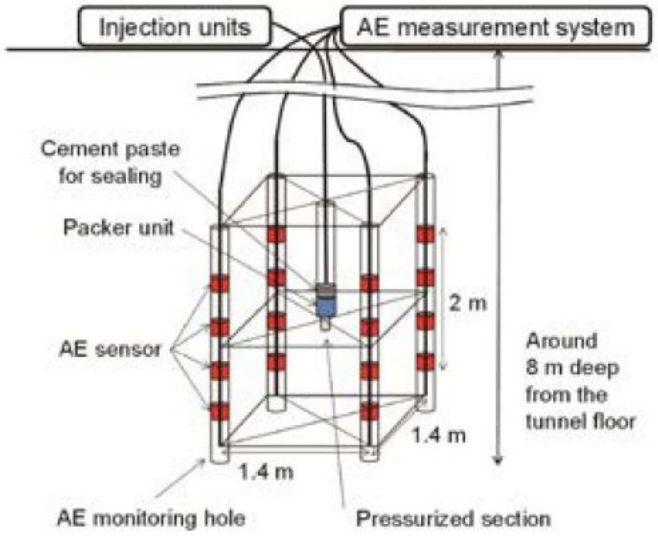

Figure 20: Experimental setup for HF monitoring during injection of supercritical CO_2 (Ishida et al. 2017).

3.3.2.2 Hydraulic fracture monitoring

Zang et al. (2016) conducted hydraulic fracture monitoring using AE, MS, broadband and electromagnetic signal response (EM) sensors. The test was performed at 410 m depth in hard crystalline rock at the Äspö Hard Rock Laboratory (HRL). These HF-tests were conducted to optimize the geothermal heat exchange in crystalline rock mass through multistage hydraulic fracturing. The AE-setup consisted of 11 sensors (GMuG MA BLw-7-70-75) in total, where two were placed at the tunnel wall, 8 in two boreholes and one sensor on the face of the neighboring tunnel, the set-up is shown together with AE-source location in Fig.21. The operational frequency range of the AE-sensors were 1 - 100 kHz.
Of the initial 69,400 AE hits 196 remained after processing and noise-filtering. The data showed AE hits being recorded after the initial fracturing, and also during the reopening of the initial HF, as can clearly be seen in Fig.22 obtained from Zang et al. (2016).

3.3.2.3 Grouting of soil-tunnel

Huck & Koerner (1981) used AE-sensors to detect fracturing caused by pressure grouting of an urban soil tunnel. The tested tunnel was excavated in a silty sand which was stabilized using a chemical grout injected with a high flow rate. During the grouting works the AE-monitoring system was used in such a way that when spikes in AE was recorded the pressure was decreased and slowly increased until another AE burst took place, these bursts were then interpreted as hydraulic fracturing due to pressure increase. The pressure recorded at the onset of these AE bursts were then interpreted as the critical pressure needed for HF to be initiated. This information was then used by the grouting operator to make a decision based on whether grouting should be continued or not, proving the applicability for AE-monitoring to "detect structural distress in a timely fashion on a production grouting project" Huck & Koerner (1981).

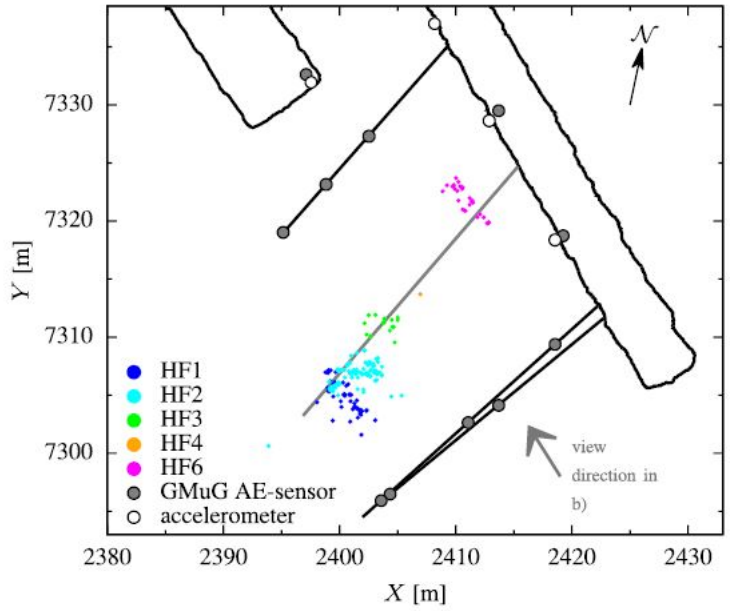

Figure 21: AE-sensor placement, and recorded AE-signals, during HF testing at 410 m depth in the Äspö Hard Rock Laboratory (HRL) (Zang et al. 2016).

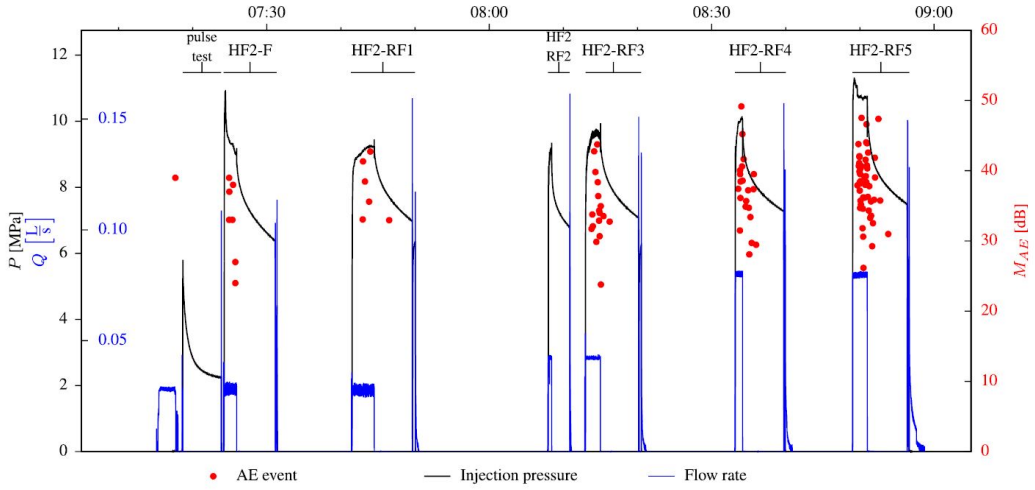

Figure 22: Correlation AE-hits to pressure and flow obtained during hydraulic fracturing of a crystaline rock mass at the Äspö Hard Rock Laboratory (HRL). HF - F indicates HF formation and RF indicates re-fracturing/opening. (Zang et al. 2016).

3.3.3 Acoustic emission sources and frequency

In soil AE signals are created by inter-grain friction and in a rock mass the signal can be the result of both fracture initiation and displacement (Dixon et al. 2003), or "relative movement between structural units" as explained by Hardy (2003). The same mechanism is mentioned by Ødegaard & Nilsen (2021); where AE-monitoring was conducted during a true triaxial laboratory test and the recorded AE-response was believed to result from repeated dynamic loading of fracture asperities. In addition to this Feng et al. (2019) suggests micro-crack opening and closing, volumetric expansion mechanisms and pore collapse mechanisms all create AE-signals that are distinguished from each other based on the polarity of the first motion P-wave. When a rock is fractured the elastically stored energy is converted to elastic waves that propagate out from a hypocenter where the fracturing took place (Hardy 2003). These waves propagate with different frequencies depending on the amount of energy released, the acoustic waves detectable by AE-sensors are usually in the frequency range of 10^4 - 10^5 Hz but might also be in the lower ranges of 10^6 Hz (Fig.23).

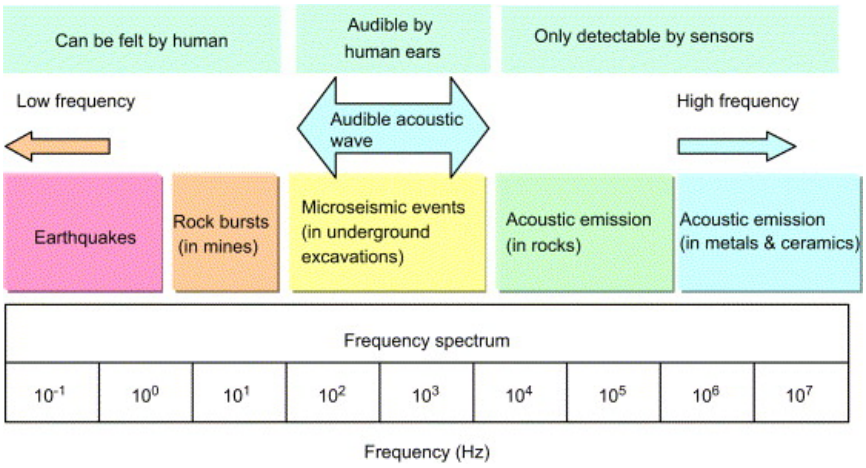

Figure 23: Resulting wave frequency from different sources related to rock engineering, the relevant range for AE is marked in green 10^4 10^5 Hz (Hardy 1981, Cai et al. 2007).

One common method for visualizing the frequencies present in an elastic wave is through the use of a fast-fourier transform (FFT). This algorithm can be used to find the spectral characteristics of the acoustic signal, which according to Zhang (2018) can be related to the rock state, rock structure and mechanical properties. In the same article it was found that the absolute energy and dominant frequency could be an indication of the scale of cracks within the rock mass. The part which is of interest to this study is that "a low frequency, high-energy acoustic emission signal usually represents the generation or development of large-scale cracks" (Zhang 2018), it is assumed that hydraulically jacked fractures will display the same low frequency domination.

3.3.4 AE-parameters

There are many parameters associated with an AE-wave, these parameters can be used to filter the signal through conducting a parametric analysis as described in section3.3.5.2 . These AE-parameters are semi-automatically extracted from the time-domain waveform by the processing system (AEwin) which simplifies the signal, making it easier to interpret and extract relevant characteristics of the wave for further analysis/processing (Zhang 2018). An example of a time-domain waveform and the parameters associated with it are shown in Fig.24. The following list is a break-down of the most common AE-parameters used Feng et al. (2019):

- **Trigger-point:** Prior to data acquisition a threshold value is selected based on the expected noise level, the threshold value is often greater than 45 dB during in-situ AE monitoring. The trigger-point is the point on the wave where the threshold value is exceeded and the data acquisition system (DAS) starts recording the parameters associated with the wave.
- **Pre-trigger:** This parameter is chosen by the AE-operator and determines the recording duration of data to be included prior to the trigger-point. According to the ISRM it is recommended that the pre-trigger is one-fourth of the number of samples of the recorded waveform.
- **Length of waveform:** The amount of recorded samples is determined by the waveform length as it relates to the sampling rate. For example at a sampling rate of 5 Mega Samples Per Second (MSPS) a length of 10 000 will allow for 488 μs of data in a single wave form.
- **Duration:** The duration of an acoustic wave is the length of time the wave spends with an amplitude exceeding the threshold value. The maximum duration is related to the length of the waveform and the sampling rate. In the previous example the maximum duration would be 488 μs.
- **Amplitude:** The amplitude is the voltage recorded at the signal peak (or trough) of a wave-form. Amplitude is commonly measured in decibel (dB).
- **Rise-time:** The time from the trigger-point to the highest peak is denoted as rise-time.
- **Count:** The number of signal pulses in a wave whose amplitude exceeds the threshold value. In Fig.24 the depicted wave would have a count of 5 (peaks above the threshold line).

  (Feng et al. 2019).

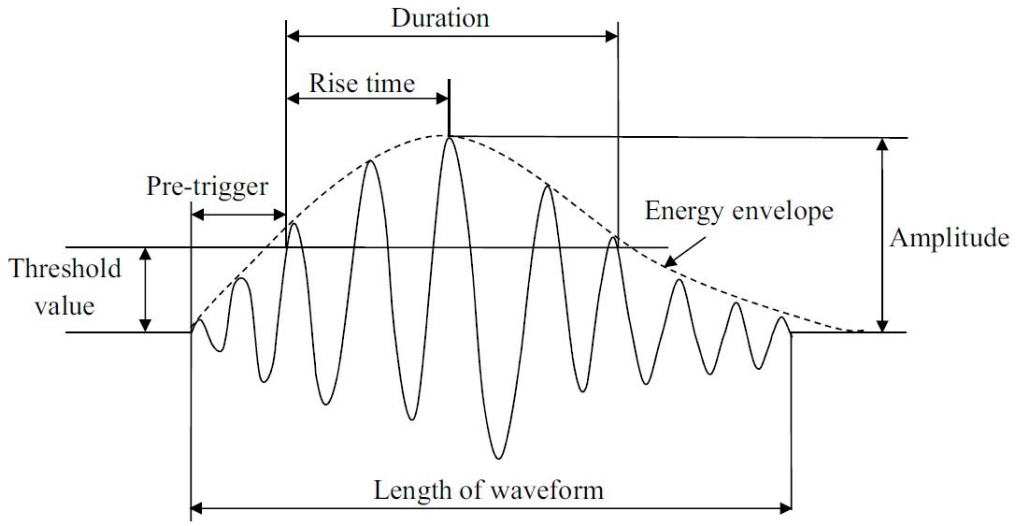

Figure 24: Important AE-waveform parameters (Feng et al. 2019).

3.3.5 Noise filtering

During in-situ AE measurements there are a number of potential noise sources. Some of these sources include, but are not limited to: percussion drilling, haul trucks, machine- and system noise, blasting, vibrations, electrical signals etc.. The best remedy for noise reduction is to control the noise source, either through ceasing operations or alternatively conducting the measurements at a time of low construction activity. There will always be some form of noise present in the data-set, but it's important to remove/limit the amount of noise to make further processing and analysis easier (Feng et al. 2019). In the following section the most frequently used approaches to noise filtering will be presented briefly.

3.3.5.1 Frequency filters

Perhaps the most common form of noise filtration is through the use of low-, high- and/or band-pass filters. These filters work by only recording a set component of the incoming wave, where a high-pass filter only allows frequencies higher than the cut-off value to pass through it, meaning that lower frequencies are filtered away, the opposite is true for a low-pass filter. A band-pass filter on the other hand can be looked at as a combination of a high- and low-pass filter, meaning that only frequencies occurring within a given range (or band) is allowed through the filter. An example of frequency filtering is shown in Ishida et al. (2014), where a band-pass filter between 5 - 100 kHz was applied to reduce the environmental noise. The choice of frequency filter can be found through trial and error, or if the frequency of the noise is known this can be used as a filter value. Another

approach applied by Niemz et al. (2020) is to use the fourier transform of the stacked AE-waves received at each sensor to visualize the frequency spectra and then decide on the band-pass filter which contains the main-frequency peaks and neglects the noise occurring outside of this band, the example given by Niemz et al. (2020) is shown in Fig.25.

3.3.5.2 Parameter value discrimination

Koerner et al. (1981) mentions a variety of this filtering where the hypothesis is that the rise time of true acoustic signals is shorter (i.e. sharper rise time) than background noise (i.e. longer rise time), meaning that values having long rise times can be filtered out during signal processing as they most likely are the result of noise. The same approach can be applied to other AE-parameters and their values (e.g. amplitude, duration, absolute energy etc.) as long as the values associated with noise or data for that particular parameter is known.

3.3.5.3 Spatial filtration

If the sensor array used contains enough sensors (minimum five) and these are placed sufficiently far apart it's possible to triangulate where an AE-signal originated. The reason for needing five sensors is due to the x, y, z coordinates and occurrence time being unknown and "the quadratic nature of the distance equation" Feng et al. (2019). Based on this concept Koerner et al. (1981) describes spatial filtration as rejecting all the signals that originate outside of the monitored target area, e.g. airborne noise originating from outside of the monitored rock mass.

3.3.5.4 Acoustic shielding

This approach isn't directly signal filtering as it entails reducing the amount of noise reaching the sensors through shielding the sensors from the environment, an example of acoustic shielding is to conduct AE-measurements from boreholes Koerner et al. (1981). There are many examples of this approach to signal monitoring in the literature, e.g. Zang et al. (2016).

3.3.5.5 Waveform filtering

According to Zang et al. (2016) the waveform associated with noise differ clearly from those associated with true AE signals. Based on this it's possible to screen AE-hits visually and exclude data based on their waveforms, this was one of the approaches utilized to filter out false AE-events during HF-monitoring at Äspo HRL (Zang et al. 2016).

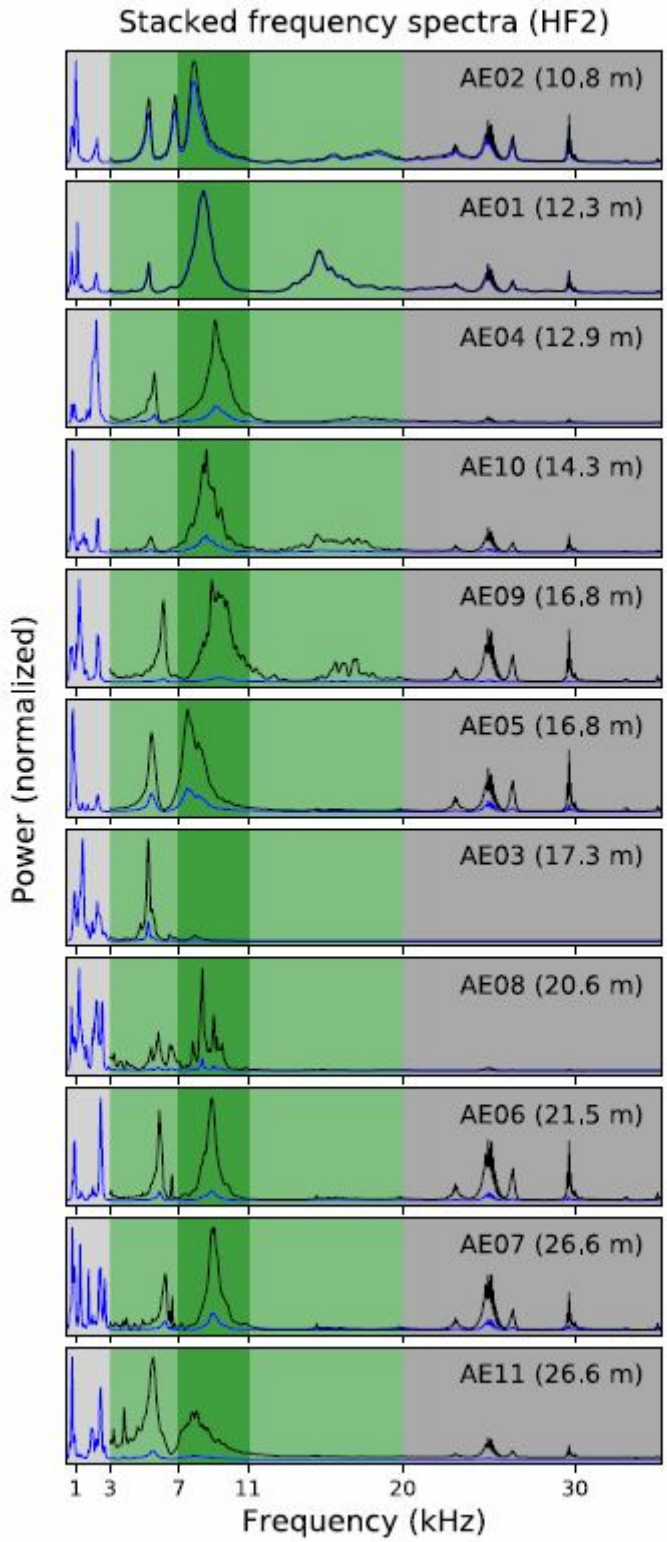

Figure 25: Frequency spectra obtained from sensor-wise stacking of AE-signals monitored during HF-testing at Äspo HRL by Niemz et al. (2020). The light- and dark green represents the choosen band-pass filters for further analysis. Light- and dark grey areas represent low-frequency and high-frequency noise respectively.

3.3.6 Attenuation

The high frequency created by AE is prone to attenuation (weakening) over long distances, meaning that the signal is only detectable within a small volume of rock compared to micro-seismic events (Feng et al. 2019). Koerner et al. (1981) illustrated the amount of attenuation for different materials as indicated in Fig.26. The figure clearly shows how attenuation is dependent upon frequency, the same dependency is noted by Hardy (2003). Based on the values given by Koerner et al. (1981) the attenuation ranges from roughly 10^{-4} - 1 dB/cm for the frequency range of 1 khz - 100 khz measured by the sensors used during this master thesis (table: 2). Another important factor not indicated in Fig.26 is the amount of internal structures (e.g. joints and strata), with more structures resulting in higher attenuation (Liu et al. 2020).

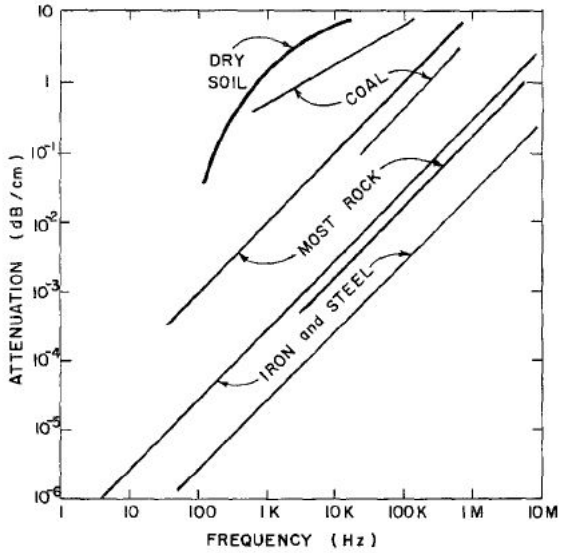

Figure 26: Amount of attenuation (dB/cm) for different frequencies and materials (Koerner et al. 1981).

Codeglia et al. (2017) states that it is possible to reduce the amount of attenuation by using a wave guide in the form of a rod or tube inserted into the rock mass consisting of a low attenuating solid (e.g. steel ($< 10^{-4}$ dB/cm)), the concept is shown in Fig.27. The principle of a wave guide is to create a low attenuation pathway that directs AE signals from the source to the AE sensors (Dixon et al. 2003).

One problem with using a wave guide is that low frequency waves might pass through the wave guide without propagating to the AE-sensor. This occurs if the wavelength is greater than four times the diameter of the wave guide tube/rod (Hardy 2003). However, these waves are not as prone to attenuation and therefor might travel to acoustic sensor regardless.

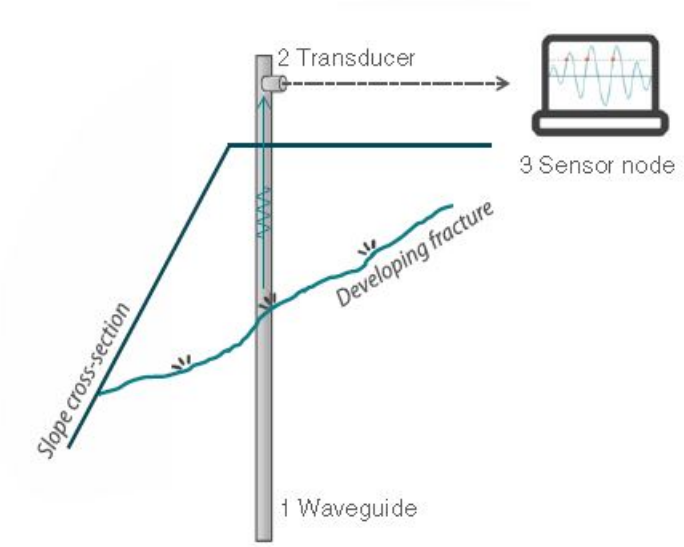

Figure 27: Wave guide concept sketch, a metal rod is inserted into the rock mass to help the AE-signal reach the AE-sensor by providing a low attenuation pathway (Codeglia et al. 2017).

3.3.7 Attenuation mechanism

According to Hardy (2003) the different mechanisms for AE wave attenuation is: geometric spreading, internal friction, scattering and mode conversion. In the following sections these will be briefly described together with formulas used to calculate them:

3.3.7.1 Geometric Spreading

Geometric spreading is the attenuation resulting solely from the geometry of the wave front. The energy in an elastic wave is equal to the amplitude squared (A^2) and when the elastic waves from an AE source propagates outwards this energy is distributed over a larger surface area. This leads to a reduction in amplitude (attenuation) following the relationship:

$$A = A_0/r \tag{8}$$

Where A_0 is the amplitude at the source and A is the amplitude at distance r from the source. This relationship is true for spherical wave propagation, which often is the case for AE sources (Hardy 2003).

3.3.7.2 Internal friction

In a rock mass the main attenuation mechanism is mechanical energy being transformed into heat due to friction acting between rock particles (Liu et al. (2020) and sources therein). This loss can be quantified according to the following equation by Hardy (2003):

$$A = A_0 e^{-\alpha r}, \tag{9}$$

where A, A_0 and r are the same as in Eq.8 and α is the attenuation coefficient, research indicate that α is frequency dependent (Hardy 2003). According to Liu et al. (2020) the density of minerals in a rock is the main factor influencing the attenuation of an elastic wave, with denser rocks showing lower attenuation coefficients.

3.3.7.3 Scattering

When a elastic wave encounters an obstacle (e.g. a mineral grain) secondary waves might form and scatter out from the obstacle surface. This will in turn reduce the overall energy of the initial wave front (Hardy 2003). This scattering effect only occurs when the obstacle is roughly the same size as the wavelength of the elastic wave, i.e:

$$d \approx \lambda, \tag{10}$$

$$\lambda = C \times f, \tag{11}$$

where λ is the wavelength, d is the mean mineral grain diameter, and C and f are the wave propagation velocity and frequency respectively. If the rock mass is blocky the same scattering can occur if the wavelength is comparable with the average block size (Hardy 2003).

3.3.7.4 Mode conversion

The final attenuation mechanism is mode conversion. When a wave propagates through a layer boundary, either cohesive or non-cohesive, at an oblique angle refracted and reflected wave components will be created. The degree of mode conversion is related to the angle of incidence and acoustic impedance of the materials at the boundary. This mode conversion will reduce the energy of the initial wave, leading to attenuation of the original signal (Hardy 2003).

4 Method

4.1 AE equipment

The AE equipment ordered to be used during the in-situ AE monitoring was produced by Physical acoustics corporation, part of Mistras group inc., and consisted of three AE-sensors (Table 2) and a structural health monitoring system (SHM) of the type Micro-SMH. However, there was a delay in the shipping of R.45I so during the AE-monitoring only two sensors were used.

Table 2: The ordered AE sensors and their respective bandwidth and sensitivity

Sensor	Bandwidth	Peak sensitivity
R.45I	1-30 kHz	124 dB
R3I-AST	10-40 kHz	120 dB
R6I-AST	40-100 kHz	117 dB

Because the expected frequency of the AE-waves resulting from jacking were unknown sensors having different bandwidths were chosen, so as to maximize the likelihood of detecting AE-signals during the field tests. The band-with of the sensors were overlapping so that the whole bandwidth from 1 - 100 kHz would be covered by the sensor array. Due to the delay of R.45I the covered frequency range was only 10 - 100 kHz during the monitoring conducted at Løkjelsvatn.

4.2 AE set-up

4.2.1 Data acquisition setup

The sensors were connected to the SHM system using cables. The task of the SHM system is to filter the incoming AE signal based on the defined filter strategy applied by the AE operator, after this the signal is digitized (analogue to digital conversion) and routed to a built in SoC (Zynq-7000 series) for feature extraction. The extracted features are then transferred to the acquisition computer (laptop) (Mistras group 2017), at Løkjelsvatn this was done through a Wi-Fi connection created by the SHM system itself.

Prior to the field work the AE-system was set up with: a pre-amplifier gain of 26 Volt for both channels, a band-pass filter of 20 kHz - 1 MHz, pre-trigger value of 25.6 μ_s, wave length of 10 (10K samples max. and the sampling rate was set at 5 MSPS (mega samples per second). Prior to monitoring the threshold value was set at 20; however, this was altered during the field work as it was found to be too sensitive. On the acquisition computer the incoming AE signals were observed in

real time and saved through the program AEwin produced by Mistras inc. group. The program was set up in such a way that a new .DTA file was created when the amount of data in the current file surpassed 6500 kB. In total 232 .DTA files were created during the field monitoring at Løkjelsvatn.

4.2.2 Mounting of the AE sensors

4.2.2.1 Wall mount

To mount the AE sensors to the tunnel wall two holes were drilled using a electric power drill with a strong steel bit capable of drilling through rock (Fig.28a). Then to ensure optimal surface area between the rock face and AE-sensor a roughly 4 x 4 cm area was flattened using a hammer and chisel before it was further flattened using an angle grinder (Fig.28b). The result of drilling and flattening is shown in Fig.30.
Threaded expanding bolts were then hammered into the holes and a steel plate was attached to these bolts using nuts. The sensor would be placed between the steel plate and the rock mass, so make sure the sensors weren't damaged by the steel plate a thick rubber square was placed between the plate and the sensor. Another function of the rubber was to allow for a slight angling of the sensor so as to ensure a good coupling to the rock. To reduce the amount of attenuation at the intersection between the sensors and rock surface a coupling agent in the form of a bathroom silicone sealant was applied to the sensors. Then the sensor was put in place and pressed against the rock wall by tightening the nuts, pushing the steel plate against the back end of the sensor. The full set-up is illustrated and photographed in Fig.29.

(a)

(b)

Figure 28: Photos captured during the AE sensor trial in Løkjelsvatn power plant. a) shows the drilling of holes for the expanding bolts, b) shows how the rock surface was flattened using an angle grinder prior to mounting the sensors (source: private photos).

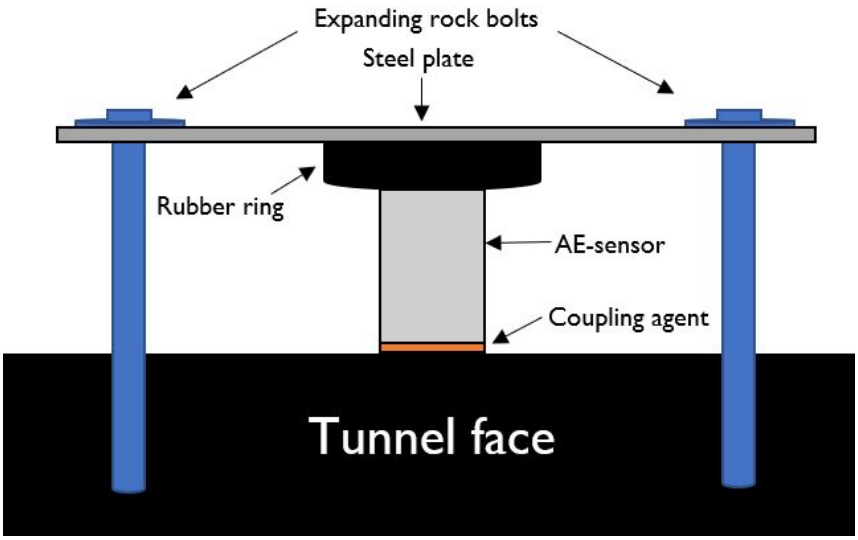

(a)

(b)

Figure 29: a) Illustrations showing how the AE sensors were mounted to the tunnel face using expandable bolts, steel plate and a rubber ring. (b) Photo of the setup taken during field work at Løkjelsvatn power plant (source: private photo).

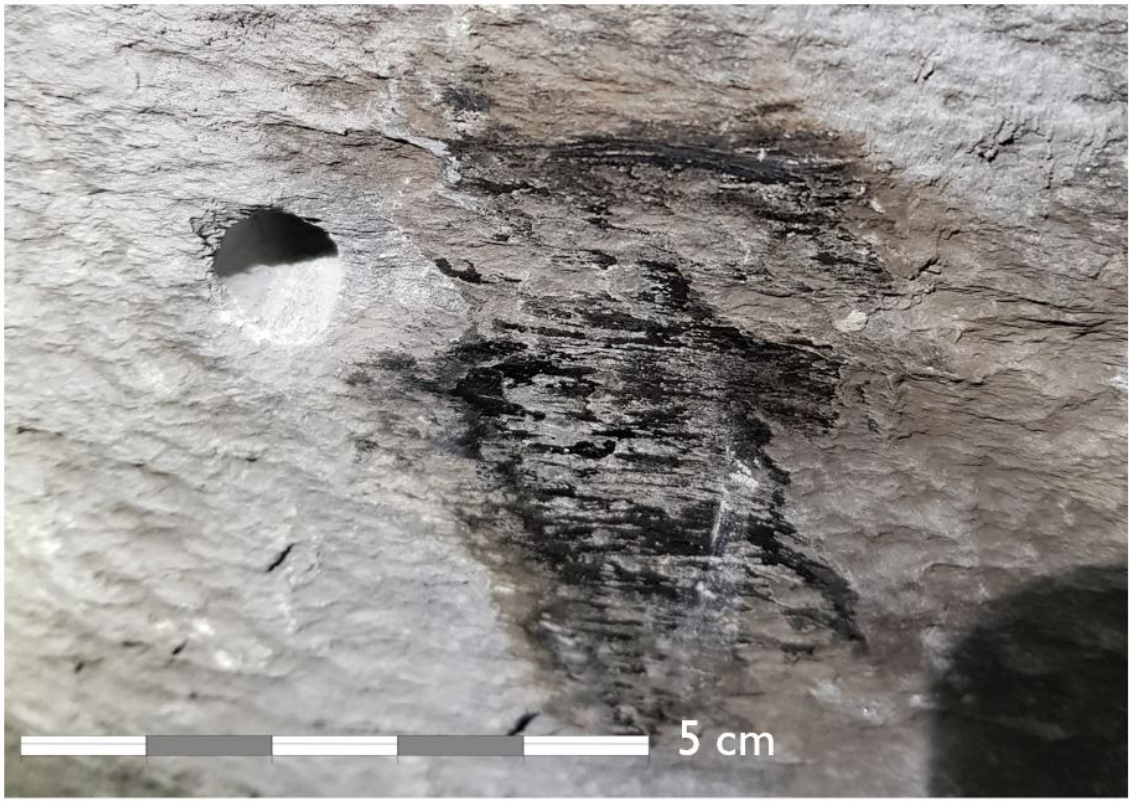

Figure 30: Flattened and smoothed area (black) after chiseling and angle grinding, this was done to ensure optimal coupling between the rock surface and AE sensors. (private photo).

4.2.2.2 Hole mount

After experiences gained during the Løkjelsvatn field work it was decided to mount the sensors within boreholes at the Nordøyvegen field work. Sadly, no monitoring was conducted due to unforeseen circumstances. The plan will still be mentioned in this section even tho it was never implemented successfully.
To conduct AE-monitoring from within a borehole the plan was to drill 100 mm holes using the tunneling jumbo that was drilling the grouting holes at the tunnel face. This diameter was chosen as it would be big enough to accompany the AE-sensors with the attached wires.
Prior to mounting the sensors the bottom of the monitoring borehole would need to be flattened using a grinding bit, this would be done to ensure a smooth rock surface onto which the sensors could be mounted.
Customised drill rods with circular supports created to fit a 100 mm borehole would be used to center the AE-sensors and keep them in place at the bottom of the borehole. If gaps existed between the circular support and borehole wall tape and styrofoam plates would be used to fill the gap, so that the sensors and drill rod would fit snugly in the borehole and not vibrate. To keep the sensor and rod in place at the end of the borehole two expansion bolts could be mounted to the tunnel face (same procedure as Løkjelsvatn, section.4.2.2.1) and a rubber strap would be wrapped around the rod and attached to the bolts, applying a slight inward pressure, a schematic of the plan is shown in Fig.31.
Before inserting the customised drill rods a thick layer of bathroom silicone sealant would have been added to the ceramic plate on the sensors. Then finally the cables from the sensors would be attached to the SMH-system which would hang from a plastic bag at the tunnel face and transmit data to the nearby acquisition computer.

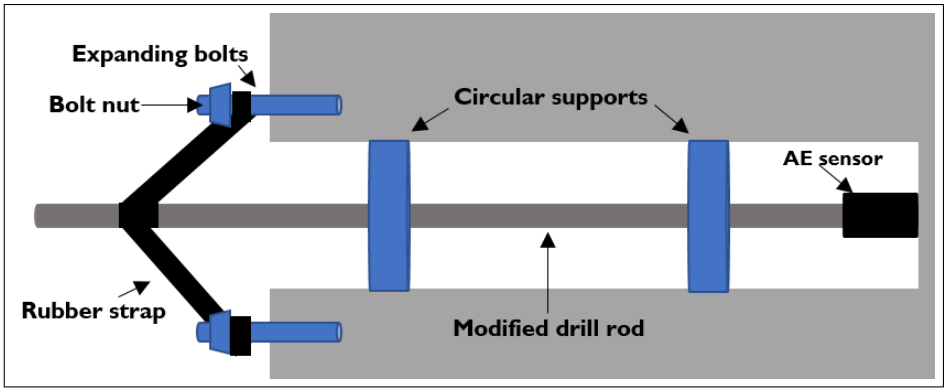

Figure 31: Schematic figure showing how the AE sensors would be mounted inside boreholes during the monitoring conducted at Nordøyvegen. Circular supports would be attached to a drill rod and then the AE-sensors would be attached to the end of this modified rod. To keep it all in place rubber strap would be wrapped around the rod and attached to two bolts at the rock surface.

4.3 Data processing

After acquiring the data in the field data processing is used to filter the data and to extract valuable information for further analysis.
During this thesis the data was filtered using different approaches and then subsequently analysed and plotted using different python modules, in the following section these approaches will be briefly presented.

4.3.1 AEwin

One of the hardest parts of AE-monitoring is to only extract the relevant AE-data by separating the data from the noise. To combat this the data was filtered and processed using the program AEwin. The processes for which it was used will be described in this section.
The first major use of AEwin is strictly just to access the .DTA files created by the SHM-system and extract the data present within these files (frequency, AE-parameters, waveforms, sample rate etc.). The first step that was conducted in AEwin was to combine all the .DTA files associated with the same HF-test. This had the added benefit of reducing the amount of files needed to be handled, making plotting and data-analysis easier and quicker.
Then the data-sets for each HF-test were separated into four folders; hits from hydraulic fracturing, hits from hydraulic jacking cycle nr.1 and cycle nr.2 and hits from noise. The AE hits that occurred within the time span of the first pressurization cycle were assigned to the HF folder, and the hits occurring in the second cycle were assigned to HJ1 and those in the third pressurization cycle were assigned to the folder HJ2. Hits occurring outside these pressurization cycles were deemed as noise and removed, except for 60 AE-hits that were extracted to discern any difference between the data and the noise. A visual representation of the time intervals associated with these folders is shown in Fig.32.
There was a slight time difference of 4 minutes and 44 seconds between the HF-monitoring computer and AE acquisition computer which needed to be corrected for. To find the time interval used to extract the relevant hits the start time and end time of the filtered pressurization cycle was converted to seconds and the respective time in the AE files would then be this time plus 285 seconds (4:44 min) added to it. This time interval was then used as the filter range in AEwin with every hit occurring outside this time span being rejected.

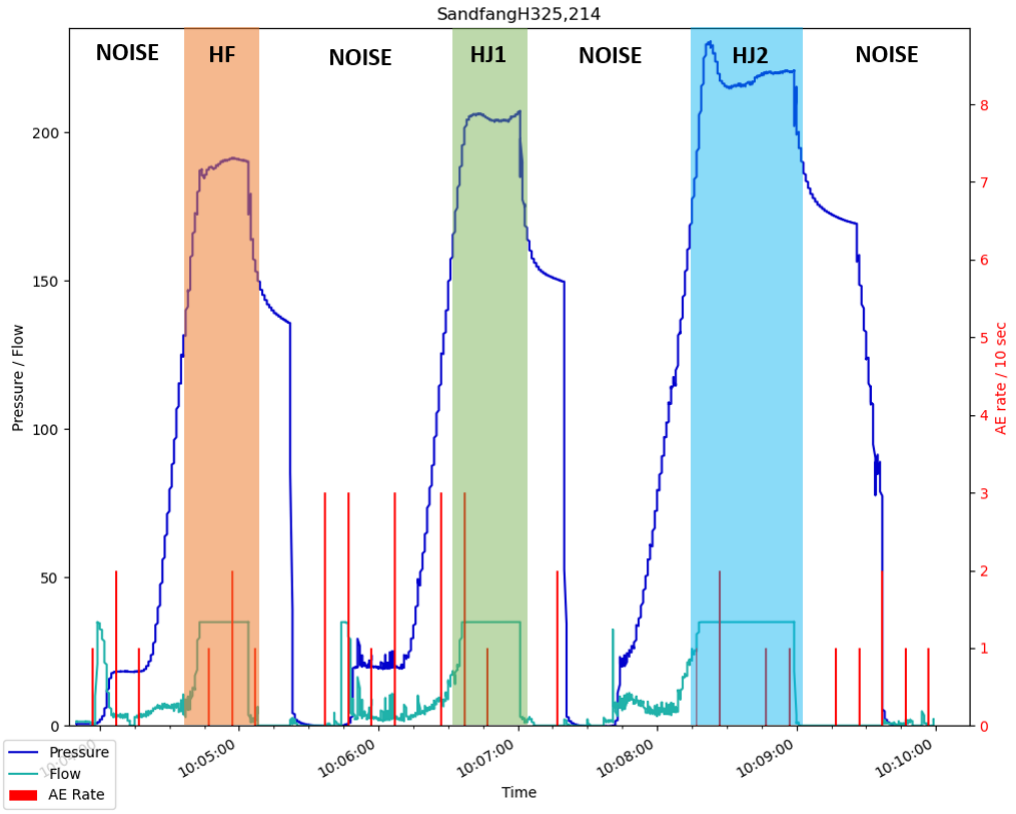

Figure 32: AE hits that fell within the orange interval on every HF-test conducted were assigned to the category "hydraulic fracturing" (HF) and every AE hit within the green interval were assigned to the category "hydraulic jacking 1" (HJ1) and every AE hit within the blue was assigned to HJ2. Every AE hit that fell outside of the marked columns were considered as noise and removed from further analysis, except 60 hits that were extracted and used to compare the data with the noise.

Since the AE data contained a lot of noise related to water hitting the sensors (see Fig.40) the water spikes that were present in the HF/HJ folders (after the initial separation) were removed during a second round of filtering. These spikes related to water arrived close to the end of each pressurization cycle, where the flow-rate drops down to zero. And since the water hitting the sensors was anything from a small trinkle (smaller rate spikes) to larger water streams (large rate spikes) the author decided that every AE hit occurring close to this drop in flow (+/- 5 seconds) was to be removed from the final data set, even if the removed spike wasn't due to water, as it was impossible to distinguish the origin of these spikes during post-filtering. The AE-hits from SandfangH228,27 and Sandfang328,213 was discarded as the data from these was seen as too noisy for further analysis. Finally the .DTA files in each folder were converted to two sets of .txt files, one set of parameter values (example in Fig.33) and one set containing waveform values (example in Fig.34).

Version V1.40

Sat Jan 16 08:34:12 2021

ID	SSSSSSSS.mmmuuun	CH	RISE	COUN	ENER	DURATION	AMP	ABS-ENERGY	P-FRQ
1	311.7722872	2	0	1	0	0	25	13.406E-03	102
1	325.7486800	2	25	4	0	36	31	1.471E+00	92
1	328.0768698	2	5	1	0	5	25	98.314E-03	92
1	599.1734263	1	5	2	0	10	27	230.888E-03	107
1	600.0168675	1	0	1	0	0	25	0.000E+00	92
1	601.9172475	2	5	2	0	15	27	280.417E-03	92
1	614.4910870	2	18	5	0	42	29	1.186E+00	107
1	717.8494410	2	75	10	0	97	31	3.076E+00	97
1	728.5856120	2	27	4	0	28	28	739.028E-03	107
1	735.7028500	1	5	3	0	45	31	1.316E+00	102
1	736.5186000	1	10	3	0	52	31	1.339E+00	83
1	741.6319435	2	0	3	0	95	29	1.028E+00	107
1	753.3084745	2	4	1	0	5	25	92.728E-03	92
1	861.6106778	1	4	3	0	53	31	1.174E+00	102
1	865.0498595	1	14	16	0	321	32	7.825E+00	83
1	866.8617650	1	11	2	0	16	30	757.462E-03	83

Figure 33: Text file structure for AE-parameters associated with different hits acquired from AEwin.

```
DATE: Friday, January 15, 2021
TIME: 20:03:27
SAMPLE INTERVAL (Seconds):   0.0000002000
SIGNAL UNITS: volts
TIME UNITS: Seconds
DATA TYPE: WAVEFORM
NUMBER OF DATA POINTS PER WAVEFORM: 10240
CHANNEL NUMBER: 2
HIT NUMBER: 2
TIME OF TEST: 401.2349003

 0.00335693
 0.00366211
 0.00396729
 0.00427246
 0.00457764
 0.00488281
 0.00488281
 0.00488281
 0.00488281
 0.00457764
 0.00396729
```

Figure 34: Text file structure for one AE-wave acquired from AEwin.

In AEwin a number of different parameters can be extracted, but the only ones that were used in this thesis were the "common" ones, i.e. rise time, count, duration, amplitude and absolute energy. Energy and peak frequency were also extracted (see Fig.33) but the value of energy was always 0 or 1, which isn't as useful for statistical analysis and peak frequency was seen as redundant when the Fast Fourier Transform analysis was conducted (see section.4.3.2).

4.3.2 Fast Fourier transform

Using a Fast Fourier Transform (FFT) AE waves were transformed from the time domain to the frequency domain, an example of which is shown in Fig.35. This was done to discern any potential differences between the noise- and data not present in the time domain. To achieve this a python code using the fast-Fourier transform module of scipy (Virtanen et al. 2020) was implemented, this code is shown in Appendix. A.3 and A.4.
This code is quite simple and only takes the number of samples (data points) and sample interval as input, both of which are given in the AE-wave files (see Fig.34). From these files a sample interval of 0.0000002 seconds and number of samples equal to 10240 was found. The sample interval is the same as 1/ sample rate which was the chosen input in the code. This was done as to easier convert the output to kHz (divide sample rate by 1000) as oppose to Hz which was given when the sample rate was used. So a sample rate of 5000 was used (5 MSPS/1000). Then the code was fed data from stacked AE-waves (i.e. every wave in a folder were fed into the algorithm at the same time) to extract the frequency spectra associated the stacked AE-waves.

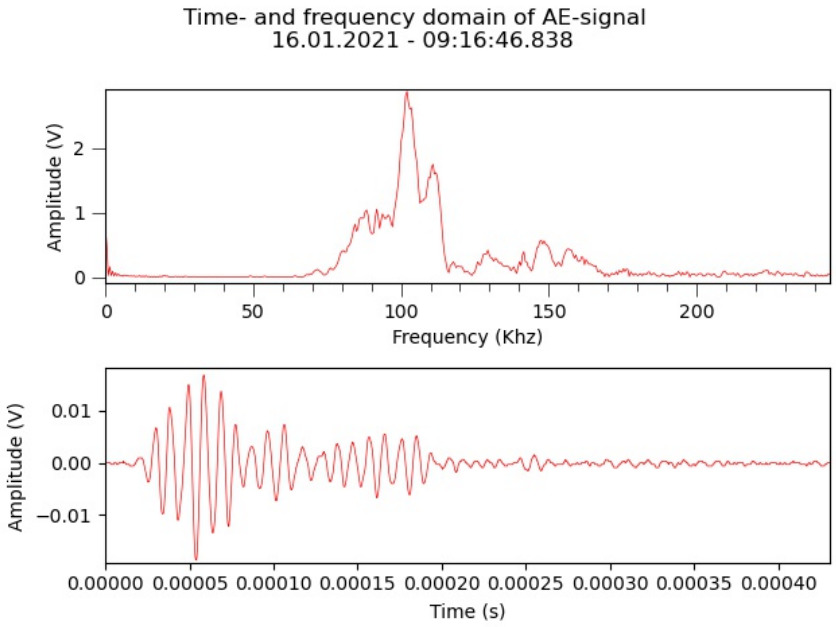

Figure 35: Example of an AE wave in the time domain and frequency domain, to obtain the dominant frequencies a Fast Fourier Transformation (FFT) was conducted on the stationary AE wave shown. In this example the dominant frequency is 100 kHz and the range of the dominant cluster is from 60 kHz - 115 kHz.

4.3.3 Statistical analysis

To conduct the statistical analysis the statistics module of scipy by Virtanen et al. (2020) was implemented into a python code. From the statistics module the Mann-whitney U test (originally published by Mann & Whitney (1947)) was implemented in a code which was used to calculate the statistical U- and P-values related to the different AE-parameters. This was done to discern any difference between the data related to HF, HJ1, HJ2 and noise. In the same code the Q1, Q3, mean, min and max values, the typical five number summary used in statistics were calculated. This code is shown in Appx.A.2 and applies the scipy statistics module, numpy module by Harris et al. (2020) and python statistics module (different from scipy stats) by Van Rossum (2020).
This statistical data was then plotted as box-plots using the python module matplotlib by Hunter (2007). This code is shown in in Appendix. A.1.

4.3.4 AE-rate plots

More python code was implemented to analyse the rate of AE occurrence and plot the AE rate per 5 seconds up against the pressure and flow graphs obtained from the HF-test conducted at Lökjelsvatn. To calculate the AE rate a five second bin would be passed along the time arrays for every AE-hits and count the number of hits occurring within every 5 second span. Then the AE rate bin was plotted at the place where the bin time and HF-test time was identical. The codes used to do this is shown in Appendix.A.7, A.6 and A.8.

4.3.5 Frequency domain and time domain plots

To view the apparent noise waves found throughout this study in the time and frequency domain the python code shown in Appendix.A.5 was created. This code takes a wave file and extract the wave parameters then conducts a fast fourier analysis on the wave parameters and plots them along side the time domain appearance of the same wave. Examples of the result is shown in Appendix.B.

5 Results

5.1 Løkjelsvatn AE-measurements

5.1.1 AE parameter distributions

The result of the parameter-study conducted on the data from Løkjelsvatn power plant is summarized in Table 3, the same data is shown graphically in Fig.36. This data will be further discussed in section.6.2.3 and is only presented here.
There appears to be a difference between the AE-hits associated with hydraulic fracturing and hydraulic jacking seen in the data. Most of the data related to every data-set is highly skewed towards the right, except for amplitude for HJ1 which is skewed towards the left.
HF generally has a higher absolute energy and amplitude and lower count and duration when compared with HJ1 and HJ2. HJ1 has a higher AE-count and longer rise time than both HF and HJ2 but a lower duration than HJ2. The differences in HJ1 and HJ2 with regards to absolute energy and amplitude are very small, but it appears as HJ2 has a generally lower values for these parameters with regards to the inter-quartile range, however it also has the highest values with regards to the max (whiskers) for both absolute energy and amplitude. The noise displays a tendency towards higher count and rise time when compared to all the other parameters and a higher duration than HF and HJ1, but a lower duration than HJ2, which is the highest. The absolute energy and amplitude for noise is higher than HJ1 and HJ2 but lower than that found to represent HF.
There appears to be a general decline in amplitude, a slight decrease in absolute energy, and an increase in duration with each HJ-cycle following fracture initiation. Count and rise time show no clear trend with each HJ-cycle and absolute energy is lower during HJ than HF.

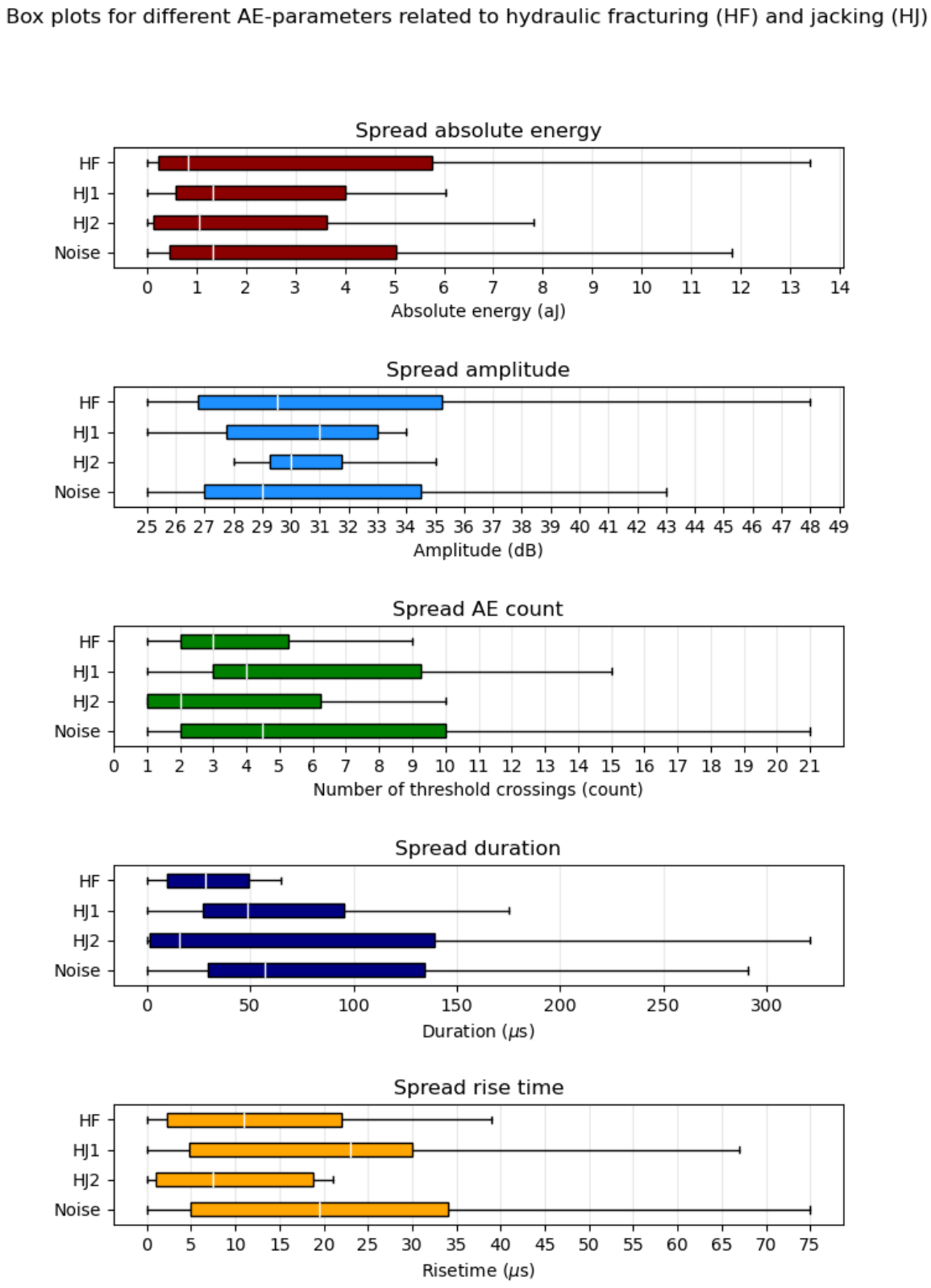

Figure 36: Statistical analysis of parameters related to hydraulic fracturing (HF), both instances of hydraulic jacking (HJ1-2) and noise acquired from Løkjelsvatn. Every parameter is skewed to the right and outliers are removed prior to plotting but not prior to creating the box plots.

Table 3: Statistical five number summary for AE parameters related to HF, HJ1, HJ2 and noise

AE parameters: HF

Parameter	Min	Q1	Median	Q3	Max
Abs-energy (aJ)	0.0	0.23	0.84	5.75	13.4
Amplitude (dB)	25.0	26.75	29.5.0	35.25.0	48.0
Count	1.0	2.0	3.0	5.25	9.0
Duration (μs)	0.0	9.75.0	28.5.0	49.5	65.0
Rise time (μs)	0.0	2.25	11.0	22.0	39.0

AE parameters: HJ1

Parameter	Min	Q1	Median	Q3	Max
Abs-energy (aJ)	0.0	0.58	1.33	4.0	6.038
Amplitude (dB)	25.0	27.75	31.0	33.0	34.0
Count	1.0	3.0	4.0	9.25	15.0
Duration (μs)	0.0	27.25	48.5	95.5	175.0
Rise time (μs)	0.0	4.75	23.0	30.0	67.0

AE parameters: HJ2

Parameter	Min	Q1	Median	Q3	Max
Abs-energy (aJ)	0.0	0.13	1.06	3.6	7.825
Amplitude (dB)	28.0	29.25	30.0	31.75	35.0
Count	1.0	1.0	2.0	6.25	10.0
Duration (μs)	0.0	1.25	15.5	139.0	321.0
Rise time (μs)	0.0	1.0	7.5	18.75	21.0

AE parameters: Noise

Parameter	Min	Q1	Median	Q3	Max
Abs-energy (aJ)	0.0	0.450	1.32	5.04	11.818
Amplitude (dB)	25.0	27.0	29.0	34.5	43.0
Count	1.0	2.0	4.5	10.0	21.0
Duration (μs)	0.0	29.5	57.0	134.25	291.0
Rise time (μs)	0.0	5.0	19.5	34.0	75.0

5.1.2 Statistical analysis

Most parameters displayed high p-values when analysing the differences between each data-set, this data is given in table.4 where the lower p-values ($p<0.1$) are highlighted in bold. It is clear that the greatest difference is found in the parameters count, duration and rise time as these are associated with the lowest p-values.
In the following paragraph only the p-values indicating a large difference between the tested data sets is mentioned, this is because these findings are assumed to be the most important ones when checking for any difference in AE-parameters, which was within the scope of this thesis. Between HF and HJ2 the p-value for count, duration and rise time is the lowest; 0.0815, 0.0659 and 0.0780 respectively. The same values for HF and HJ1 is higher with p-values for the same parameters being 0.2351,0.3802 and 0.3165 respectively. Between HJ1 and HJ2 the lowest p-values are found when analysing the difference based on count and rise time; p-value=0,0709 and 0.0631, respectively.
The difference between HF and noise is again greatest for the parameters count, duration and rise time with p-values being 0.0378, 0.0087 and 0.0459 respectively. The same goes for HJ2 and noise where the p-values are 0.0327, 0.0538 and 0.0248 for count, duration and rise time respectively. HJ1 and noise indicate high p-values for each parameter.
The apparent difference observed in Fig.36 with regards to absolute energy between HF and HJ1 ($p=0.4022$) and HF-HJ2 ($p=0.2258$) can't be said to be a definite difference since there exists a roughly 22 - 40% chance that the observed difference is due to random chance. The same goes for amplitude where HF-HJ1 ($p=0.4327$) and HF-HJ2 ($p=0.4833$) where the chance of the difference being random is roughly 43-48%.

Table 4: U-statistics and P-values for the AE parameters associated with HF, HJ1, HJ2 and noise

U-statistics and p-value from comparing HF-HJ1, HF-HJ2 and HJ1-HJ2

	HF/HJ1		**HF/HJ2**		**HJ1/HJ2**	
Parameters	U-statistics	p-value	U-statistics	p-value	U-statistics	p-value
Absolute energy (aJ)	240.5	0.4022	243.5	0.2258	156.5	0.2505
Amplitude (dB)	244.0	0.4327	277.5	0.4833	166.5	0.3511
Count	220.0	0.2351	213.5	**0.0815**	130.0	**0.0709**
Duration (μs)	238.0	0.3802	207.5	**0.0659**	144.0	0.1491
Rise time (μs)	230.5	0.3165	212.0	**0.0780**	127.5	**0.0631**

Sample size (n): HF=28, HJ1=20, HJ2=18, Noise=60
Low P-values highlighted in bold

U-statistics and p-value from comparing HF-Noise, HJ1-Noise and HJ2-Noise

	HF/Noise		**HJ1/Noise**		**HJ2/Noise**	
Parameters	U-statistics	p-value	U-statistics	p-value	U-statistics	p-value
Absolute energy (aJ)	752.0	0.2165	583.0	0.4273	476.5	0.2274
Amplitude (dB)	812.0	0.4023	547.0	0.2791	485.0	0.2581
Count	642.5	**0.0378**	585.5	0.4379	385.5	**0.0327**
Duration (μs)	574.0	**0.0087**	533.5	0.2316	404.0	**0.0538**
Rise time (μs)	652.0	**0.0459**	598.5	0.4956	374.5	**0.0248**

Sample size (n): HF=28, HJ1=20, HJ2=18, Noise=60
Low P-values highlighted in bold

5.1.3 Frequency domain

From Fig.37 the frequency spectrum of AE hits associated with HF, HJ (1 & 2) and noise is shown. The three major frequency clusters for the HF AE hits is 94 kHz, 111 kHz and 144 kHz in descending order based on magnitude, for HJ1 the major regions are 83 kHz, 89,5 kHz and 102 kHz. HJ2 has three clusters in the area 105, 98 and 92 kHz. The frequency distribution for noise is clustered around 93, 91, 102 kHz in descending order based on amplitude of frequency cluster. The rise for each frequency cluster is also more rapid in HJ1 and HJ2 when compared with HF and Noise. It appears like the range between different frequency clusters are reduced during progressive fracturing. For HJ the range is 50 (144-94 kHz), for HJ1 and HJ2 the same range is 19 and 13, respectively. The noise frequencies appears to be more chaotic in nature, as there are only two clear frequency clusters as oppose to the other data-sets where there appears to be multiple smaller clusters. The noise is generally weaker in amplitude with the top two peaks having an amplitude of 0.220 and 0.177. For HF the three top peaks are at amplitudes of 0.300, 0.210 and 0.179. HJ1 is 0.254, 0.199 and 0.185 and HJ2 is 0.329, 0.274 and 0.198 respectively.

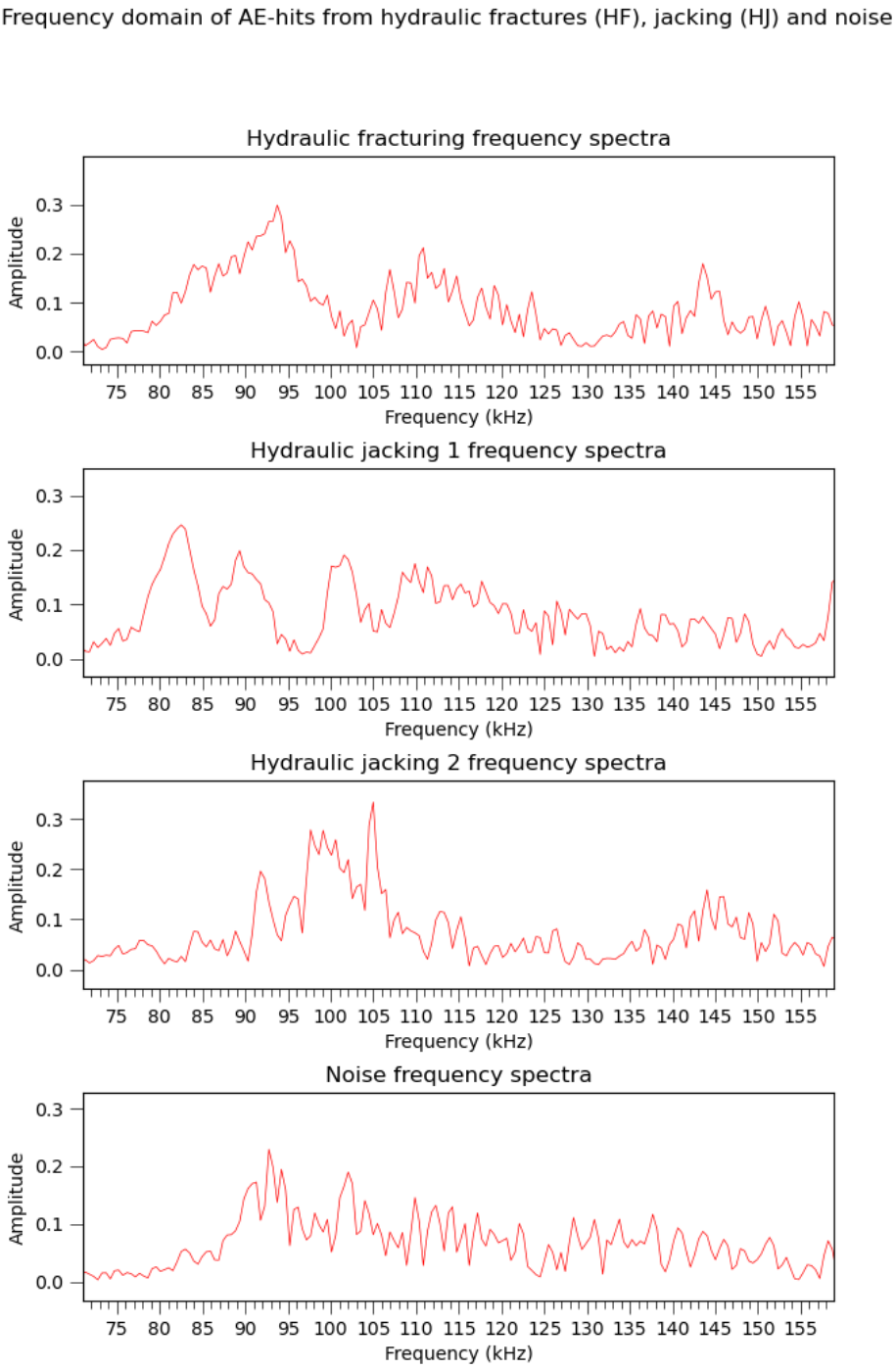

Figure 37: Frequency spectra distribution for the AE hits associated with HF and HJ. HF spectra generally indicate higher frequencies (94 kHz, 111 kHz and 144 kHz) on the three major peaks as oppose to those related to HJ1 (83 kHz, 89,5 kHz and 102 kHz), HJ2 (105, 98 and 92 kHz) and noise (93 kHz, 91 kHz and 102 kHz). HJ also has a much quicker rise in frequency indicating a narrower frequency band for each cluster.

5.2 AE-rate

In Fig.38 and Fig.39 the rate of AE signal occurrence (# of AE hits/ 5 sec) is plotted against the flow and pressure data acquired during HF-stress measurements at Løkjelsvatn power plant.

The data plotted here is the filtered data used in the above mentioned statistical analysis, the same plots in their unfiltered state is shown in Appendix.C, an example of which is also shown in Fig.40. Note that the unfiltered figures plots the AE rate every 10 seconds as the computational load of plotting this data every five seconds was too great, causing python to shut down due to stack overflow.

The following description is for the plots located in Fig.38: Plot a, c, d, e and f in indicate an increase in AE rate at the start of the first pressurization cycle, this increase is coinciding with the assumed point interpreted as break down pressure (P_b). There are also AE-spikes occurring within the middle and towards the end of the constant flow portion in the first pressurization cycle for plot a and f. a, b, d, e and f all indicate an increase in AE-rate at the point assumed to be the reopening pressure (P_r) for the second and third pressurization cycle.

The following description is for the plots located in Fig.39: g, h, i, j and l all indicate an increase in AE-rate corresponding with P_b, g, h, i and l also include AE-spikes towards the end or middle of the first pressurization cycle. g, h, i and k all indicate an increase in AE rate at P_r for the second pressurization cycle. h and i shows an increase at P_r for the third cycle. g, h, i and j all show an AE rate increase towards the middle and/or end of the second pressure cycle. g and i also indicate the same increase for the third cycle.

An example of noise present in the rate data prior to filtering is shown in Fig.40. Note that the rate spikes shown in Fig.39 (g) is also present in Fig.40. However, it's not visible as the AE-rate towards the end of the pressurization cycles is too great, effectively hiding the smaller AE-spikes shown in Fig.39 (g).

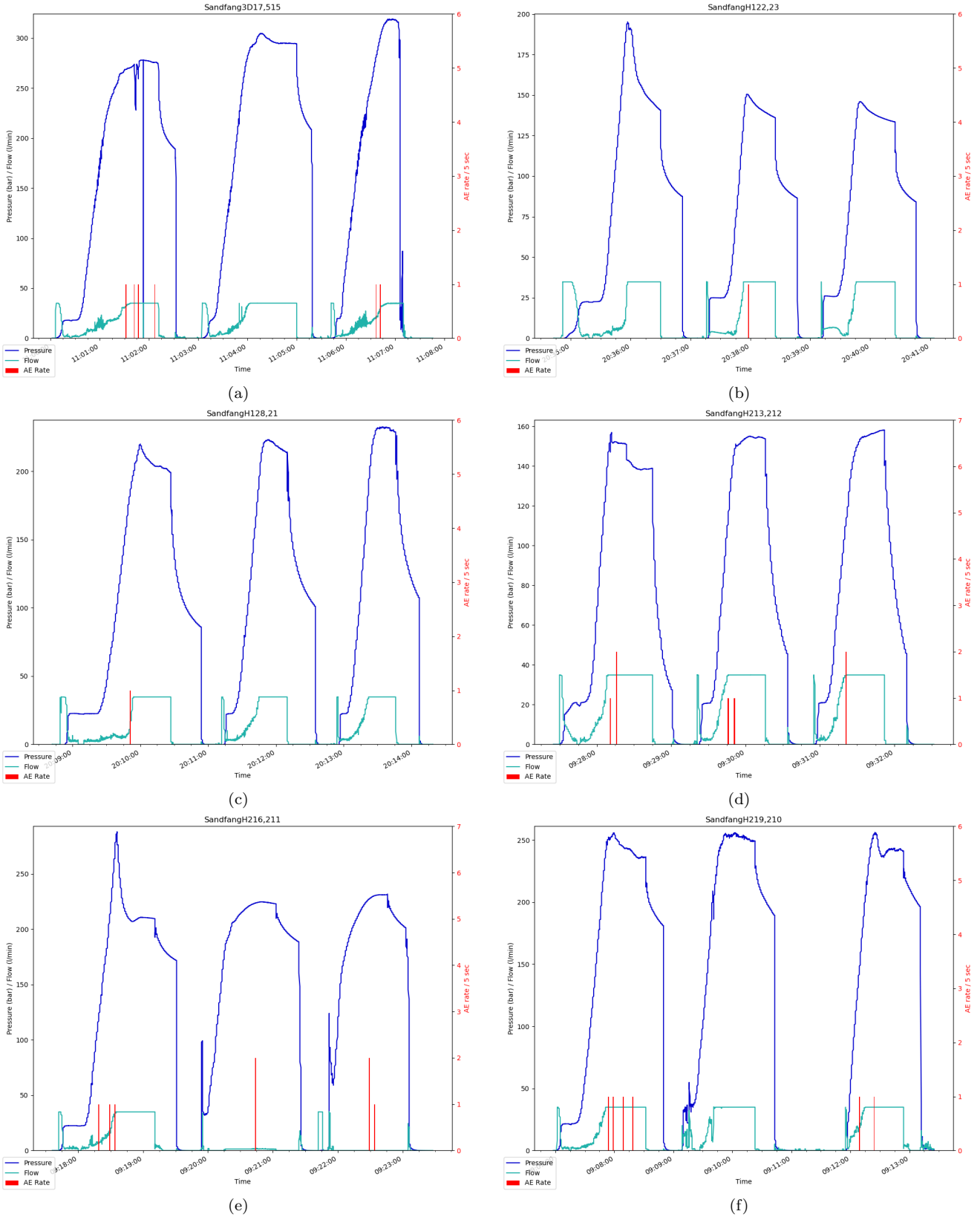

Figure 38: Plot showing how the AE-rate measured in hits per 5 seconds compares to the pressure and flow from HF tests at Løkjelsvatn power plant.

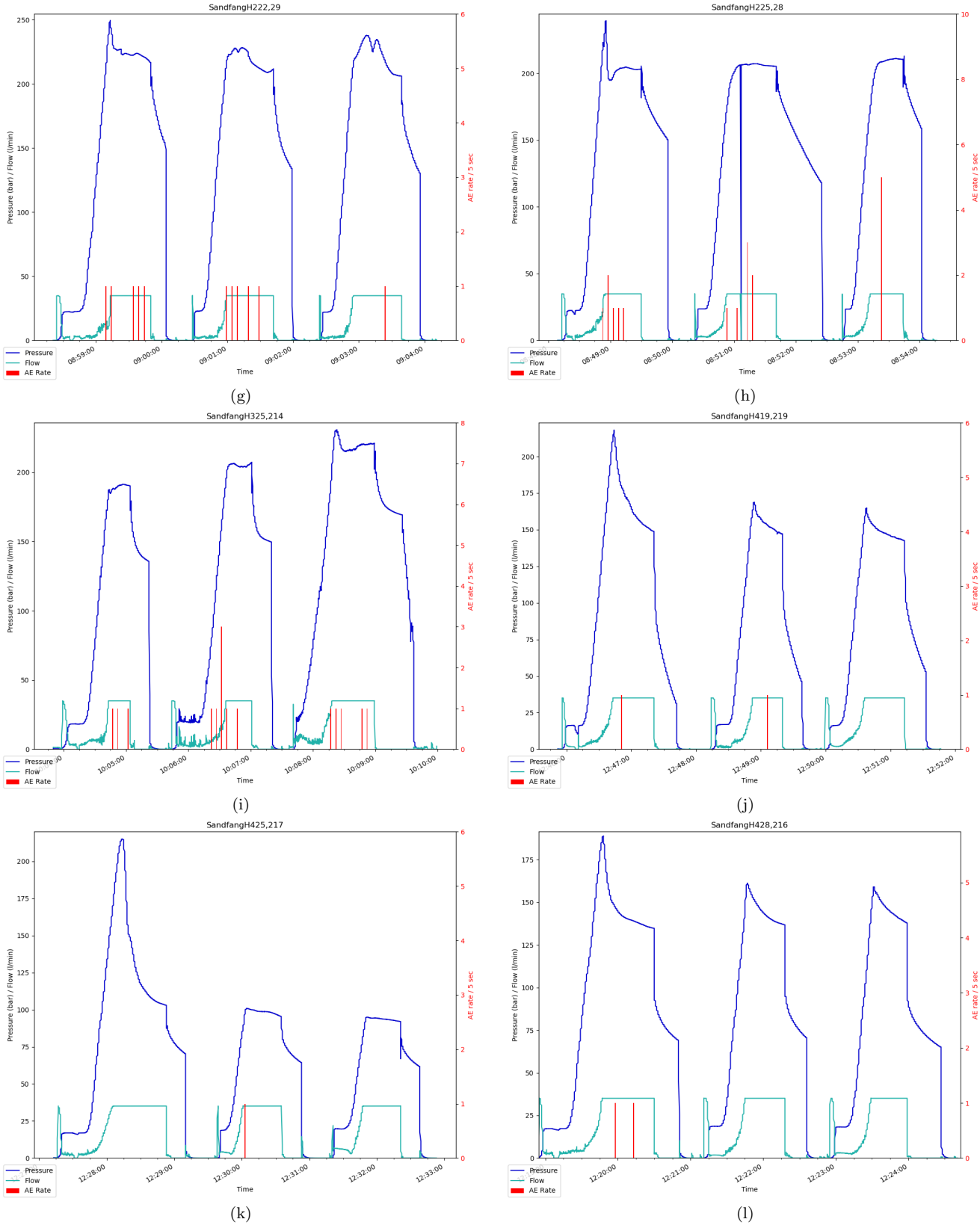

(g) (h) (i) (j) (k) (l)

Figure 39: Plot showing how the AE-rate measured in hits per 5 seconds compares to the pressure and flow from HF tests at Løkjelsvatn power plant.

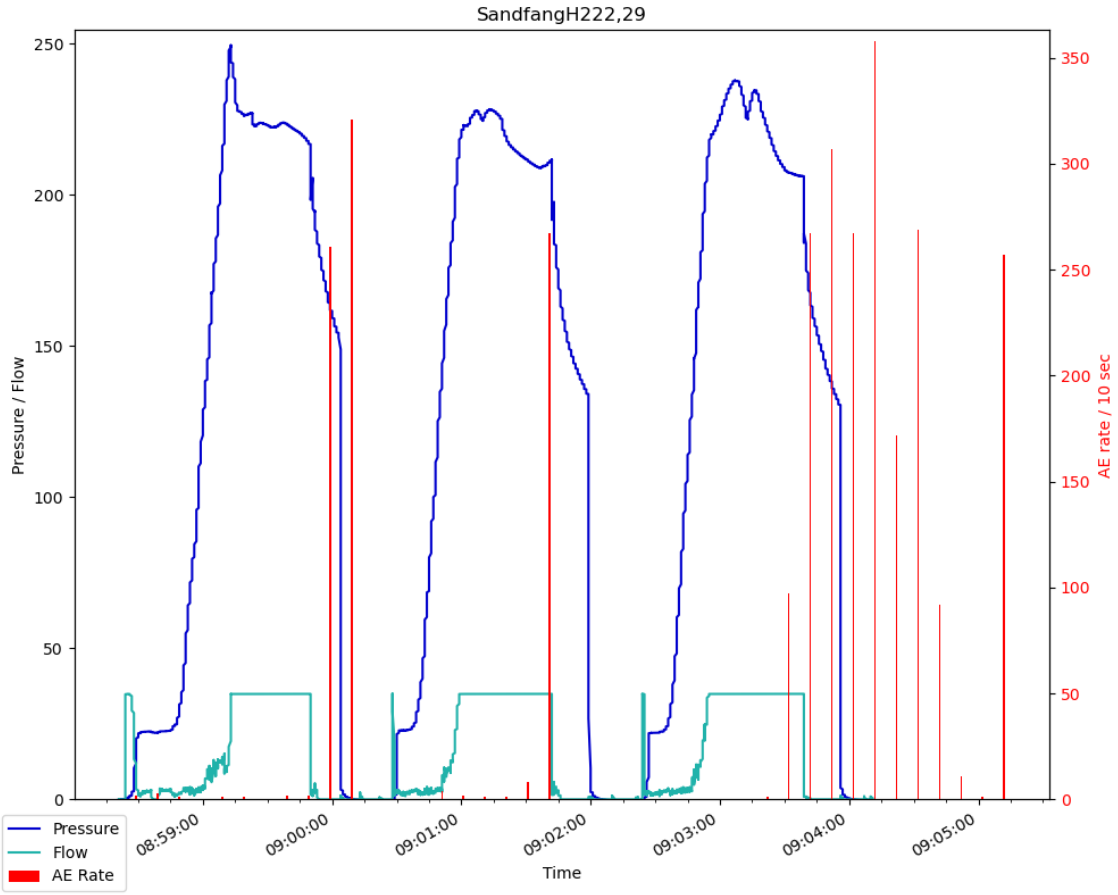

Figure 40: Unfiltered AE-data and its AE-rate. The spike towards the end of the pressure cycles is due to water hitting the sensors. Note that the AE-rate spikes indicated in Fig.39(g) is still present in this figure, but the magnitude of the spikes caused by the water (>100 hits) drowns them out.

6 Discussion

In the following discussion the source of AE during fracture jacking will be discussed, followed by the data acquired during in-situ monitoring at Løkjelsvatn along with potential improvements to the AE-program. Then the plan for Nordøyvegen will be presented together with what went wrong and how these problems can be mitigated in the future. Then lastly the potential use of AE to detect HJ during pre-excavation grouting will be presented.

6.1 AE source during jacking

6.1.1 Frictional shear

It is common knowledge that rubbing two objects together causes sound, for instance when rubbing your hands or when a sandpaper is dragged across a piece of wood. The source of this sound caused by rubbing/frictional sliding is complex; however, a simplified explanation is given in the article by Le Bot (2017), here the source of roughness noise (frictional noise) during sliding is explained as asperity tips repeatedly striking each other, like small hammer impacts exciting the structure, which create small vibrations (sound waves) that propagate outwards. This mechanism of sound wave generation is thought to be the source of acoustic emission signals originating during jacking, i.e. frictional shear along touching asperity surfaces. Since roughness is scale dependent the same mechanism is expected to cause acoustic signals during inter-grain frictional sliding as well as during shearing of fractures.

During pressurization a fracture might open both through tensile reopening (HJ) and through slip along pre-existing fractures, often called hydro shearing. The latter of which occur when the frictional resistance within a fracture is overcome and the fracture is oriented favourably with respect to the in-situ stresses Gischig et al. (2015). During the creation of enhanced geothermal systems (EGS) hydro shearing of pre-existing faults or fracture zones have been associated with substantial earthquakes of a greater magnitude than those associated with hydraulic fracturing (Gischig et al. 2015). There is clearly a scale difference between an EGS and HJ, but Gothäll & Stille (2009) mentions that some horizontal deformation can occur within a fracture if shear loads act on it. During lab monitoring of controlled fracture reopening through pore pressure increase of a sandstone Stroisz et al. (2016) found that fracture sliding invoked significantly more AE events compared to fracture generation, propagation or reopening.

Therefore it can be assumed that it's the same (or similar) mechanisms that cause seismic vibrations at field scale (hm/km scale faults) and at smaller scales in the lab (mm/cm scale fractures). This indicates that frictional shear might be one of the sources of acoustic signals during hydraulic jacking in the field, as this has been the case at both relatively larger and smaller scales.

It can be assumed that the roughness and filling of the joints, i.e. frictional resistance, in the monitored rock mass should have an impact on the usefulness of in-situ AE-monitoring. The effect of fracture infilling on AE-signal strength will probably depend on the thickness and type of infilling. When a sufficiently thick mineral filling is present the AE-signal resulting from jacking will probably be due to the inter-grain friction acting within fracture filling material. This seems likely as inter-grain friction is the interpreted AE-source during the study conducted by Codeglia et al. (2017). From Fig.41 the angle of friction for different fracture filling materials is shown, it can be assumed that a higher angle of friction will lead to a stronger AE-signal, i.e. a sandy infilling will be better for AE-monitoring as oppose to a clayey infilling. This assumption is based on the fact that a higher angle of friction is indicative of higher frictional resistance, i.e. higher surface roughness. It would be interesting to compare AE-measurements from rock masses having different Q-values, specifically with regards to the joint friction (Jr/Ja) values to research whether the above mentioned assumptions are true or not.

Rock	Description	Peak c' (MPa)	Peak $\phi°$	Residual c' (MPa)	Residual $\phi°$
Basalt	Clayey basaltic breccia, wide variation from clay to basalt content	0.24	42		
Bentonite	Bentonite seam in chalk	0.015	7.5		
	Thin layers	0.09-0.12	12-17		
	Triaxial tests	0.06-0.1	9-13		
Bentonitic shale	Triaxial tests	0-0.27	8.5-29		
	Direct shear tests			0.03	8.5
Clays	Over-consolidated, slips, joints and minor shears	0-0.18	12-18.5	0-0.003	10.5-16
Clay shale	Triaxial tests	0.06	32		
	Stratification surfaces			0	19-25
Coal measure rocks	Clay mylonite seams, 10 to 25 mm	0.012	16	0	11-11.5
Dolomite	Altered shale bed, ± 150 mm thick	0.04	1(5)	0.02	17
Diorite, granodiorite and porphyry	Clay gouge (2% clay, PI = 17%)	0	26.5		
Granite	Clay filled faults	0-0.1	24-45		
	Sandy loam fault filling	0.05	40		
	Tectonic shear zone, schistose and broken granites, disintegrated rock and gouge	0.24	42		
Greywacke	1-2 mm clay in bedding planes			0	21
Limestone	6 mm clay layer			0	13
	10-20 mm clay fillings	0.1	13-14		
	<1 mm clay filling	0.05-0.2	17-21		
Limestone, marl and lignites	Interbedded lignite layers	0.08	38		
	Lignite/marl contact	0.1	10		
Limestone	Marlaceous joints, 20 mm thick	0	25	0	15-24
Lignite	Layer between lignite and clay	0.014-.03	15-17.5		
Montmorillonite Bentonite clay	80 mm seams of bentonite (mont-morillonite) clay in chalk	0.36 0.016-.02	14 7.5-11.5	0.08	11
Schists, quartzites and siliceous schists	100-15- mm thick clay filling	0.03-0.08	32		
	Stratification with thin clay	0.61-0.74	41		
	Stratification with thick clay	0.38	31		
Slates	Finely laminated and altered	0.05	33		
Quartz / kaolin / pyrolusite	Remoulded triaxial tests	0.042-.09	36-38		

Figure 41: Angle of friction and cohesion for different fracture filling materials and rock types. It's assumed that a high frictional angle would cause stronger AE-signals during jacking. Source of figure: Hoek (2006).

When the fracture filling is sufficiently thin, or not present, the joint surface roughness becomes more important as the source of friction, and subsequently acoustic signals. In Fig.42 fracture profiles having different roughness and undulation is shown for a visual representation of surface roughness, following the logic mentioned above it is believed that a stepped, rough joint/fracture would yield the greatest AE-signals. As this fracture profile is associated with the greatest amount of asperities, increasing the likelihood of asperity contact during jacking.

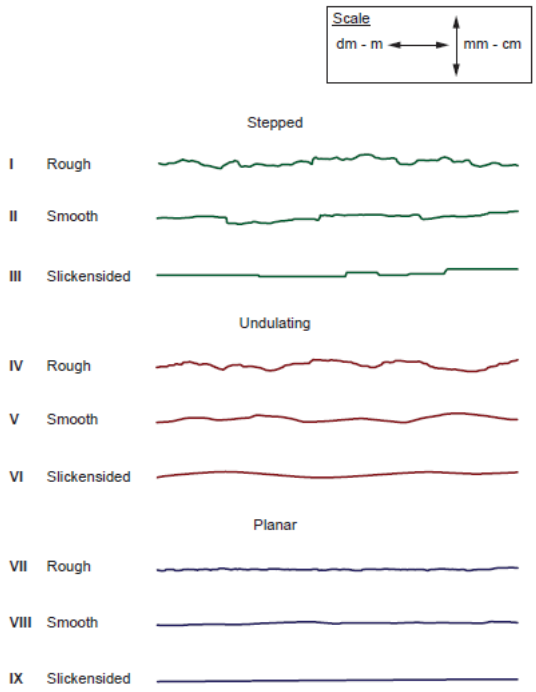

Figure 42: Appearance of fracture profiles having different roughness and undulation, source: (NGI 2015)

If there exists fractures perpendicular to the jacked fracture these could potentially be sheared emitting acoustic signals in addition to those originating within the jacked fracture itself. A situation like this could happen close to the surface where the weight of the overburden is the only normal load acting on a horizontal fracture, if an area the same size as the average block size is critically loaded uplift could ensue according to (Gothäll & Stille 2009), and close to the surface rock wedges could also in theory be lifted (Brantberger et al. 2000). Such uplift would cause shear movement between the moving blocks/wedges and neighboring fracture walls. The amount of AE-signals generated in these neighbouring fractures would also depend on the joint roughness and filling, as explained above as well as the amount of uplift, i.e. sheared distance. This is easy to imagine as more uplift will cause more asperities to come into contact, resulting in more AE-wave generation. The same will be true if there exist voids and fractures parallel to the jacked fracture, these might potentially be closed from the opening of the adjacent jacked fracture, resulting in the fracture walls bumping into each other and/or touching asperities being sheared. Such fracture closure is present during pre-excavation grouting according to Stille et al. (2012) who stated that smaller fractures will be closed during hydraulic jacking of nearby larger fractures.

6.1.2 Grout flow

Previously the flow of fluids within fractures have been picked up by acoustic emission sensors, e.g. groundwater seepage (Huck et al. 1980), and intrusion of supercritical CO_2 into pre-existing fractures (Ishida et al. 2017). It can be expected that a similar AE-signal will be present during grouting, hence another potential source for AE-signals will be the friction acting between the moving grout and fracture walls. This AE-signal can be considered as noise in some instances. However, this signal is expected to remain somewhat constant as long as the grout is flowing. Removing the AE-signals from grout flow could therefore easily be achieved by applying a sufficiently high trigger value or through the use of a band-pass filter.

6.1.3 Micro-cracks

The acoustic emission signals associated with mirco-crack opening and closing as well as pore collapse and volumetric expansion mentioned by Feng et al. (2019) is thought to be too small in magnitude for AE-sensors to notice them during in-situ AE-monitoring of hydraulic jacking. If these processes happen within a few m^3 of the AE-sensors they might be recorded, if they originate outside this relatively small volume of rock mass they are expected to be reduced to non-measurable levels through attenuation. This is because large scale cracks/fractures are associated with lower frequencies where as micro-cracks result in a higher frequency elastic signal (Feng et al. 2019), and as mentioned in section.3.3.6 higher frequency waves are attenuated more than low frequency waves.

6.2 AE-measurements at Løkjelsvatn powerplant

In the following section the data resulting from in-situ monitoring at Løkjelsvatn will be presented together with noise sources, filtering approach and potential improvements to the AE-program.
It should be noted that the following discussion assumes the acquired data actually represents AE-data from HF/HJ, however this isn't necessarily the case.

6.2.1 Noise sources

During the in-situ AE-monitoring conducted at Løkjelsvatn many potential noise sources were present. At the very first trial a low trigger value was chosen (< 20 Hz), this caused a continuous stream of acoustic emission signals to be recorded. The reason for this was most likely electrical signals from the AE-equipment itself, often called system noise e.g (Feng et al. 2019). Such a signal can be reduced by calibrating the system prior to monitoring according to (Feng et al. 2019), or by setting the trigger value at a sufficiently high value; this latter approach was the one used at Løkjelsvatn with the trigger value being increased to 20 kHz.
The other man-made noise sources during the monitoring are believed to be the following: vibrations from the pumps used to pressurize the packers and test section during HF/HTPF testing, insertion/removal of the packer-rod, geological hammer impacts on the tunnel wall, lead break tests, percussion drilling, blasting, truck engine and potentially also speech/shouting. In addition to this water flow within the borehole is a potential noise source and water hitting the sensors is definitely a source of noise during this field work, as seen in Fig.40. In Appendix.B a catalogue of the different wave-forms associated with noise during monitoring is shown. Creating such a catalogue for the project is important since algorithms matching waveform and/or frequency spectrum patterns could potentially be used to detect and remove AE-events related to noise (Lopez-Comino et al. 2017).
It should be noted that the wave forms associated with noise have been visually classified by the author based on example wave forms given in Feng et al. (2019) and Plenkers et al. (2010). The time of different noise events were noted during the fieldwork and then AE hits occurring at the same time (+/- 1 min) of the noise was visually inspected. This means that the waves assumed to be from a particular noise source could in fact be something completely different, which is an inherit problem of visual correlation.

6.2.2 Filtering

To be able to extract data from the AE-logs at Løkjelsvatn extensive filtering was needed. The reason for this was mainly the water hitting the sensors, as shown in Fig.40. The water created large spikes of >40 AE hits within a span of 10 seconds, which made interpretation difficult, at first the spikes were analysed for differences in the parameters and it was found that the spikes caused by water had a longer duration, higher frequency and absolute energy. When the data sets were filtered according to these parameters the spikes were reduced; however, they were still to prominent to be able to extract valuable data from the plots, hence it was decided to remove the spikes as a whole. This was done by only including the AE-data occurring within the constant flow portion of the pressure/flow graphs, as it is in this interval HF and HJ occur. And since monitoring HJ/HF was the scope of this field test every AE-event initiated outside the constant flow portion could be considered noise. After filtering the initial 7568 AE hits recorded at Løkjelsvatn, 66 remained an was used as the data for this thesis. Together with 60 AE hits from the noise portion.

One problem with this extensive filtering is that valuable AE-signals associated with a HF/HJ might have been excluded from the data-set if it occurred within the same time interval as the noise (e.g. water stream). Many authors have also noted an increase in AE-activity associated with fracture closure following pressure release, these signals might also have been filtered away using the above mentioned technique. That being said it was the most time efficient filtering method, the data wasn't filtered further after the removal of these spikes.

The reason for not filtering the data further was because no difference capable of being used as a filter was found between the data and noise. As can be seen in Fig.36 the data generally fell within the max/min or IQR range for the noise and hence no definitive cut-off value could be chosen. It was therefore decided to plot every AE-hit as it was expected that the same noise would be present in both the HF and HJ data sets. Meaning that supposedly any difference between the data sets were caused by the fundamental difference in the data as oppose to noise contained within the data set. This assumption could be wrong and is seen as a weakness of the study. The filtering approach shown by Niemz et al. (2020) with creating a band-pass filter based on the stacked frequency spectra wasn't applicable as the noise and data displayed similar frequency peaks (See Fig.37).

6.2.3 Acoustic emission parameters of hydraulic fracturing, hydraulic jacking and noise

Zhang (2018) states that high frequency and low absolute energy is related to the development of smaller scale cracks and that the inverse, with low frequency and high absolute energy, is generally found to represent larger fractures Zhang (2018). Since fracture jacking and fracture tip propagation increases the size of the initially formed fracture it was expected that the data acquired during HF-testing would behave in the same way. However, the data obtained during the field work did not abide by this relationship as initially expected.

As shown the absolute energy was actually lower during subsequent pressure cycles than during the initial fracture formation (see Fig.36). The frequency on the other hand appears to somewhat follow the proposed relationship. The frequency spectra of HJ1 and HJ2 generally indicate lower frequencies than the spikes related to HF, which is in accordance with the proposed relationship. However, HJ2 indicates higher frequencies than HJ1, which breaks with the expected lowering of frequencies with increased fracture size. It should be noted that due to the relatively high p-values between HF and HJ1/HJ2 it cannot be concluded that the observed difference in absolute energy isn't due to chance. If we assume the data is valid then the reason for the absolute energy discrepancy could potentially be because the initial relationship proposed by Zhang (2018) was obtained during lab-trials using a pneumatic press, meaning that the relationship might not be applicable to larger scale cracks in the field as was initially anticipated. It is also the case that the method for fracture generation is vastly different in the two projects, HF vs tri-axial testing, which might also help explain the difference.

Zang et al. (2016) noted an increase in amplitude with each HJ cycle, this observation doesn't fit to the data obtained during this thesis, where the data indicate a decrease in amplitude with each HJ cycle. Again the statistical data indicate that the proposed difference could be due to chance which might be the reason for the observed decrease in amplitude.

The frequency spectra related to the hydraulic fracturing at Äspo HRL is shown in Niemz et al. (2020). In this article a range of 3 - 20 kHz is assigned the HF/HJ data which is vastly different from the frequency spectra obtained in this thesis which ranges from 75 - 145 kHz. The reason for this might be the difference in break-down pressure and fracture reopening pressure in the two projects. Generally for the tests conducted at Løkjelsvatn the breakdown pressure was around 20 - 25 Mpa, for the project at Äspo the same pressure was around 10 - 12 Mpa Zang et al. (2016). Therefore the force needed to initiate the fractures at Løkjelsvatn was greater than that needed at Äspo HRL. Since an increase in force increases the amount of work

done by the fluid on the fracture wall during fracture initiation (Work = force x displacement x cosΘ)) then the resulting energy release was greater at Løkjelsvatn. And since higher energy leads to higher frequencies this might explain the relatively high frequencies observed at Løkjelsvatn. Or a far simpler explanation could be the fact that the sensors used at Äspo HRL were sensitive to frequencies between 1 - 100 kHz (Zang et al. 2016), whereas the sensors used at Lökjelsvatn were most sensitive to frequencies in the range 10 - 100 kHz, due to the delay of one of the sensors.
Noise data generally displays higher counts and longer rise time than the data associated with HF, HJ1 and HJ2. The latter of which is in accordance with the hypothesis stated by (Koerner et al. 1981) that background noise has slower rise times relative to true acoustic events. The p-values obtained between HF-noise and HJ2-noise for count, duration and rise time can be said to be significant ($p<0.05$), HJ1 on the other hand doesn't indicate any significance for the same parameters (see Table 4) indicating that HJ1 and noise is more similar in nature compared to HF-noise and HJ2-noise. This might be because this data contains some degree of noise, which could the peak in frequency around 90 kHz observed in the frequency spectra for both HJ1 and noise (see Fig.37), this same peak is present in HJ2 but it's not as prominent as in HJ1. Hence it can not be ruled out that noise wasn't present in both data-sets.
The reason for the increased duration with each HJ cycle could potentially be related to the increase in fracture size, no literature could be found regarding such a potential relationship with regards to acoustic emission monitoring. However, such a relationship do exist during earthquakes with larger fault ruptures being related to longer earth quake duration (Salmon et al. 1992). The source of wave formation in the two processes are different (stick-slip vs frictional shear) so such a relationship with regards to acoustic emissions is still speculation from the author.

6.2.4 AE-rate

The following discussion about AE-rate is based on the assumption that every rate-spike is from true acoustic events and not noise, this assumption could be wrong and will be discussed further in section.6.6. The following points assumed to be breakdown pressure (P_b), reopening pressure (P_r) and shut-in pressure (P_s) are found using the approach given by Haimson & Cornet (2003) mentioned in section.3.1.1.
From the AE-rate plots in Fig.38 there exists an increase in rate at or close to P_b associated with fracture formation (see Fig.8). During the second and third pressure cycle many of the observed rate-spikes correlates nicely with the point interpreted as P_r. Some spikes can be seen to occur after the interpreted P_r, these

are assumed to be related to either fracture-tip propagation or potentially also fracture closure. An increase in AE-rate during fracture closure is shown to exist in the literature, e.g. Koerner et al. (1981).
In (f) from Fig.39 and (g),(i), (j) and (l) from Fig.40 such an AE increase can presumably be observed close to the assumed shut-in pressure. The recorded AE-rates in this thesis are similar to the ones recorded by for instance Zang et al. (2016), which could be an indication that hydraulic fracturing and/or jacking were successfully recorded through the use of AE-monitoring during the fieldwork at Løkjelsvatn.
However, there exists a possibility for observer bias when interpreting data; observer bias is the tendency to see what we expect to see, or what we want to see. It's in essence a form of confirmation bias applied to data analysis.
Due to the data obtained in this thesis being so different to the previous literature with regards to the AE-parameters and their distribution during fracture growth it can not with certainty be said that HF/HJ was monitored during the field work at Løkjelsvatn. Which would indicate that the apparent connection between AE-rate and P_b, P_r and P_s should be explained by another mechanism, perhaps the apparent connection is just noise occurrences (perhaps from the HF-test equipment) being interpreted as HF/HJ. It is also just as likely that HF/HJ was observed, but that such a direct parameter comparison isn't useful/applicable. Hence the data and results remain inconclusive with regards to this aspect of the thesis.

6.2.5 Attenuation

As noted in section.3.3.6 the major mechanism leading to attenuation is: geometric spreading, internal friction, scattering and mode conversion. The shallowest HF-experiment conducted at Løkjelsvatn was 13 meters deep within the rock mass and the deepest was 28 meters deep. This means that the formed AE-waves would have to travel through 13 - 28 meters of rock before being recorded by the AE-sensors. During this travel path the geometric spreading alone would lead to substantial attenuation. In this field-test the wave-amplitude at the source wasn't known so using Eq.8 would be impossible; however, the equation does indicate that the amplitude is reduced linearly during propagation.
As noted in section.3.3.6 the attenuation shown in Fig.26 doesn't account for internal structures. Hence the fractures, layer- and foliation boundaries present in the low quality phyllite at Løkjelsvatn could potentially have caused a greater attenuation than estimated above, if the requirements indicated in section.3.3.6 were met. It's impossible to know the exact attenuation but given the quality of the rock mass and depth of the AE-source it was probably significant.

During the HF-study conducted at the Äspo HRL (Zang et al. 2016) the rock mass consisted of a hard crystalline rock which is well suited for AE-monitoring as it contains few discontinuities, contains no/low amount of foliation and is relatively dense, all of which help reduce the attenuation of AE-waves propagating through it. During this study the AE-sensors were also placed within boreholes, further limiting the attenuation. The AE-results gathered from this study (see Fig.22) strongly resemble those from Løkjelsvatn power plant, with AE-counts generally being higher during the initial fracture formation and the following jacking, see Fig.38/39. This might indicate that even with the assumed substantial attenuation the AE-sensors managed to pick up and record the AE-signal created by the HF/HJ during this field test.

6.2.6 Potential improvements to the AE-program

6.2.6.1 Attenuation reduction

The first obvious improvement would have been to place the AE-sensors within boreholes surrounding the HF/HJ-test hole, as was done at Äspo HRL in Zang et al. (2016). This would have placed the sensors closer to the source meaning that the AE-wave would have to travel through less rock mass, leading to less attenuation. Another added benefit of this would have been to place the sensors within more competent, homogeneous rock as the rock mass closest to the tunnel wall would have been damaged by the drill and blast excavation method, resulting in a disturbance zone surrounding the tunnel, as noted by Hoek (2006).
Another possible solution would be to drill a hole and grout a wave-guide in the form of a steel rod into the rock mass. Using the same figure as in the previous section (Fig.26) it's clear that the attenuation of steel is less than that of rock. The attenuation through a wave-guide would roughly be in the range of 0.01-0.1 dB/meter.
In future monitoring projects; if spilling bolts are used at the tunnel face, an AE-sensor could be attached to one of the bolts which, in theory, should work as a wave-guide (idea initially proposed by Helene Strømsvik, pers. com).

6.2.6.2 Noise reduction

After conducting the field work it was found that the implemented noise reduction wasn't optimal. It would have been beneficial if a physical shield had been placed over the sensors, which would have removed the noise created by water hitting the sensors. The monitoring was conducted in close proximity to the equipment used in the HF/HTPF-tests, resulting in vibrations and water flow interfering with the sensors. If it's possible to conduct future AE-monitoring at distance from the potential man-made noise sources this would be optimal, but this method of noise reduction will be project specific as it might not always be possible (e.g. in areas with much construction activity). In the field the drilling of additional monitoring boreholes were permitted during AE monitoring, this was a noise source that could have been avoided if it was needed. However, it's important to weigh the advantages and disadvantages when deciding whether or not to halt construction activity, as doing so might reduce advancement rates, which is associated with increased costs for the project.
Another possible solution for noise reduction, which was the plan at Nordøyvegen, is to place the sensors within boreholes. One benefit of placing the sensors within the rock mass is that the sensors will be further away from any man-made noise. At Løkjelsvatn this approach would also potentially have protected the sensors from any water dripping on them. Boreholes, together with frequency filtering, is one of the most common noise reduction measures found in the literature regarding in-situ AE-monitoring of rock masses (e.g. (Feng et al. 2019), (Ishida et al. 2017), (Zang et al. 2016) etc.).

6.2.6.3 Acoustic velocity information

It would have been beneficial for the AE-monitoring program conducted at Løkjelsvatn if the acoustic velocity of the phyllite was known. This would have allowed for an estimation of the attenuation resulting from wave scattering through use of Eq.10 - 11. The acoustic velocity is also crucial for estimating the source location of an AE-hit (Feng et al. 2019).

6.2.6.4 Source location

If more sensors were used during the monitoring at Løkjelsvatn the source of the different AE-hits could then have been estimated through arrival time differences at each sensor, sensor coordinates and the acoustic velocity of the rock mass (Feng et al. 2019).
One potential use of AE-source location is shown in Zang et al. (2016) where AE hypo-centers were used to estimate fracture location, orientation and expansion after a HF-test. The strike of the estimated fracture planes based on the AE-clouds were in good agreement with previously conducted stress measurement tests and impression packer moldings (Niemz et al. 2020) (Article based on same data as (Zang et al. 2016)).
As noted in section.3.3.5.3 a minimum of five sensors is needed to successfully locate the source of an acoustic wave. One added benefit of source location is the fact that spatial filtration can be conducted. This could have helped eliminate some of the man-made sources originating from outside of the monitored rock mass at Løkjelsvatn, making data analysis easier.

6.3 Nordøyvegen field test

Due to unforeseen consequences the planned field test at Nordøyvegen tunneling project didn't go as expected, leading to no AE-measurements being conducted. This meant that the initial scope of this thesis, using AE-measurements to verify hydraulic jacking from pre-excavation grouting, wouldn't be possible. In the following section the original plan, the problems, their consequences and potential solutions will be discussed.

6.3.1 Planned monitoring set up

Prior to the field test a plan was created for how to conduct the in-situ AE-measurements. The plan consisted of placing the AE-sensors within three boreholes surrounding a grouting hole showing leakage. This was done to ensure that a water bearing fracture was present in the vicinity of the AE-sensors, increasing the chances of jacking occurring when the grout penetrated into and sealed said fracture. Beforehand it was concluded that these AE-measuring holes would be drilled using a 100mm drill bit, then the holes would be flattened at the bottom using a grinding bit to ensure optimal coupling between the AE-sensors and rock mass.

The first problem with the field test occurred because the contractor tasked with tunnel construction normally didn't use 100 mm drill bits at their drilling jumbo. However, a worn 100 mm drill bit was found at the construction site and it was attempted to drill the monitoring holes using this, without success. The result of this drilling wasn't satisfactory as the borehole walls were highly irregular and deviated substantially. This deviation was so great that the grinding bit couldn't be inserted into the holes since the drill rod used for the grinding bit had metal rings welded to it that got stuck on the irregularities of the borehole. To counteract this an attempt was made to grind down the irregularities, but this made the hole to large, causing the drill bit to flick back and forth, making flattening the bottom of the borehole impossible. The disturbance zone at the tunnel face was also deemed to be too substantial, hence why the sensors weren't mounted on the tunnel face as was done at Løkjelsvatn. Therefore it was decided to cancel the monitoring program.

6.3.2 Encountered problems and possible solutions

In the following section the problems encountered will be briefly presented together with potential solutions.

6.3.2.1 Sub-optimal borehole quality

It is difficult to know why the borehole turned out the way it did. It could potentially be the use of high penetration rate, feed force and rotation speed, the worn drill bit, bad rock mass quality at the tunnel face or it could be a combination of some/all of these factors.
If AE-measurements within boreholes are going to be successful in the future it is important that the borehole is of sufficient quality to be able to actually use the grinding bit and place the sensors correctly. To achieve this the boreholes should be drilled using a good quality drill bit and the rotation, feed pressure and penetration rate should be optimized with regards to the rock mass properties. It is important that the contractor tasked with drilling the holes is made aware of the importance of the AE-monitoring program and why the holes need to be of a good quality.
An even better approach would be to use a diamond core-barrel to drill the borehole. This is because when conducting stress-measurements using the over-coring method the measurement borehole is drilled using a diamond core barrel and the end is flattened using a grind bit, then the door-stopper strain gauge is installed (Myrvang 1983). The same method can potentially be applied for attaching the AE-sensors at the borehole end, instead of a door-stopper.

6.3.2.2 Grout and water leakage

The drilling of the 100 mm boreholes close to grouting holes with significant leakage also resulted in grout flowing out through the would be AE-test holes when the pre-excavation grouting was started. This caused a delay in the grouting procedure since the packers available at the construction site were to small to clog the opening of these 110 mm boreholes.

If water leaks into the AE-measurement hole the same effect observed at Løkjelsvatn can occur, meaning that the sensors will be continuously triggered, making it hard to detect and interpret AE-signals radiating from the studied source. An even worse scenario would be if grout flowed into the AE-measurement hole, which was observed at Nordøyvegen. Not only does this complicate the grouting process in and of itself, it also poses a risk to the inserted AE-equipment if this isn't removed before the grout solidifies. Both of these scenarios would be costly; the first through increased time usage and grout consumption, and the second through the potential loss of AE-equipment.

To solve this something as easy as inserting a elongated packer and inflating it could be used, this would block grout and water from flowing in through fractures intersecting the borehole. One problem with this approach however is that the AE-sensors need to be mounted on the inside, or outside, of the packer. Which means the packer would have to be modified to accommodate the sensors in some way.

Another similar approach could be to create a system where an expandable metal cage with an elastic rubber sleeve threaded over it is inserted into the borehole then expanded using a packer that is removed prior to monitoring (think coronary artery stent), a similar concept to this have already been applied to the rehabilitation of leaking water pipes (Hu & Chan 2014).

Another possibility, although expensive, would be to drill holes using a fore-poling casing system where the inner diameter of the casing is large enough to accompany both the grinding bit and the following AE-measurement set-up, the idea being that the casing would keep water/grout out of the borehole. Similar to this if the borehole is drilled using a diamond core barrel as mentioned above the core barrel can be removed, bottom flattened and then the core barrel can be reinserted for AE-monitoring through the inner tube, i.e. working the same as the casing tube mentioned above. This assumes that the sensors could fit inside the internal diameter of the tube and that the potential loss of the tube is accepted.

To avoid the use of a 100 mm borehole all together the wave-guide principle could be used. To implement this at the tunnel face would mean to drill a long hole (> 10 m would be optimal) and grout a steel rod in place. If grouting won't be possible due to time constraints a swellex bolt (or similar) could be inserted and expanded

within the borehole, the bolt should in theory work as a wave-guide. When the steel rod of choice is inserted then the AE-sensors would be mounted to the end of the rod outside of the rock mass. This again introduces the risk of water and outside noise interfering with the monitoring, hence actions should be taken to reduce their extent; this can be achieved through controlling the amount of activity at the tunnel face while at the same time placing a roof over the sensors.
It is generally important that the chosen method for AE-monitoring doesn't hinder the construction work and tunnel advancement too much, as this would make in-situ AE-measurements a costly and undesirable approach to monitoring grouting for the occurrences of jacking.

6.4 Potential benefits of AE-monitoring during pre-excavation grouting

As mentioned earlier in section.3.3.6 attenuation is high when fractures exist in a rock mass. This is because AE-waves can't travel through voids and have to find contact points between asperities to propagate through a fracture. Pre-excavation grouting will possibly help reduce the amount of attenuation since the grouting will fill these voids, creating a larger area for the waves to propagate through. It is expected that the amount of attenuation resulting from the grout would depend on the grout used and if additives are present or not.
Attenuation through mode conversion is dependent on the acoustic impedance between two rock layers (or materials), this again is dependent on the density of the material and seismic velocity of the wave at the interface. Meaning that the attenuation is dependent on the W/C-ratio (high ratios have lower density) and additives for the grouting material. Therefore it can be assumed that the AE attenuation during grouting would be smaller if the grouting was done using a W/C-ratio of 0,5 as oppose to a higher W/C-ratios. It would be interesting to see possible future research comparing the attenuation from different grout types, W/C-ratios and liquid vs solidified grout in a controlled lab-setting, as the author haven't found any in the current literature.
Another potential benefit of AE-monitoring during pre-excavation grouting will be the possibility of detecting hydraulic jacking. It is believed that this is possible based on previous research (e.g. (Zang et al. 2016)) showing an increase in AE rate during fracture reopening and from the discussion regarding potential sources for AE-signals during jacking of fractures (see section.6.1). The results obtained in this thesis aren't used as proof of AE's usefulness to detect jacking due to the discussed shortcomings of the data.

If the AE-sensors are set-up properly and installed at the tunnel face (either in boreholes or with the use of a wave-guide) they can potentially detect hydraulic jacking in real time if the operator of the AE-system has sufficient knowledge in interpreting AE-signals. However, if the sensors aren't set up properly they will either record too much noise, or they might not be sensitive enough to record the jacking taking place. A better use of the AE-sensors would be to validate other means of detecting when hydraulic jacking is taking place, like the RTGC-method or pressure-flow graph analysis with the aid of the PF-index. These methods work well for their designed purpose, but both make assumptions and are thus prone to misinterpretation as mentioned in section.3.2.4.1. In this aspect AE could be a valuable tool when it comes to confirming whether or not false-positive jacking have occurred. The thought being that the AE-signal resulting from jacking will be much stronger than that of a clay-plug bursting for instance. It can be assumed that the AE-signal resulting from jacking would indicate a higher AE-rate and absolute energy than those resulting from false-positive jacking occurrences. If a large amount of hydraulically jacked fractures are monitored the AE-characteristics associated with these can also be catalogued for future references at the project, making in-situ detection a possibility.

As stated by Strømsvik et al. (2018) grout pushed into motion after a standstill could potentially lead to instances of false-jacking, if the flow of grout is a source of acoustic signals as discussed in section.6.1.2 then AE-monitoring might also be used to interpret false jacking as a real jacking event. This could happen as flow and AE-rate (hypothetically) is increased when grout is pushed into motion, if such a signal is observed together with a decrease in pressure then one might interpret hydraulic jacking where no jacking took place. Therefore the use of AE-monitoring isn't a fool proof solution to verify whether a real hydraulic jacking event has taken place. As with every other method the results obtained from AE should be critically reviewed and they should be compared with results from other methods and/or parameters. If AE proves to be useful to detect or help with the detection of HJ it will give grouting operators and project owner a valuable tool that can be used to alter the grouting scheme to best fit the project requirements. Potentially reducing the amount of unwanted jacking which will be beneficial for the project economy and also the CO_2 emissions of the project (Strømsvik 2019).

6.5 Conducting AE-monitoring successfully

There are a lot of aspects to conducting a successful AE-monitoring program, the usual approach indicated in the relevant literature on in-situ acoustic emission monitoring is shown schematically in Fig.43.
It is advised to conduct a trial run of the AE-set up whenever this is possible, this is so that potential problems related to the AE set-up can be corrected prior to the actual monitoring.
If no trial run is done then the need for good quality post-filtration is needed, and as indicated in this thesis this requires a lot of work and might yield insufficient results regardless. Therefore an emphasis is placed on the importance of trial-runs, good quality acoustic shielding and filtration techniques to conduct a successful AE-monitoring. The time of noise occurring in the field should also be reported as accurately as possible to make removing the noise from the data-set easier.

6.6 Weaknesses of the study

The fact that the data presented in this thesis indicate the opposite of the relevant literature is unfortunate, this might be because of several reason; too strict or too lenient filtering, human error related to the code produced or some other reason not thought of. The above mentioned reasons will be briefly presented here:

6.6.1 Filtering

Signal processing is a complicated subject which increases the possibility of misuse and misinterpretation. As mentioned above extensive filtering was needed to remove noise from the data-set, which is seen as the biggest weakness of this study. The filtering might have had the unintentional consequence of removing viable, important data from the data-set which could have changed the outcome of the conducted analysis. It's possible that a completely different conclusions could have been drawn and that the data might not have been as inconclusive as it was had the need for filtering not been so great.
Another weakness is that the conducted filtering only focused on the noise occurring at the end of each pressurization cycle as this noise was the most noticeable, hence noise occurring at the beginning and middle of the pressurization cycles were kept and not removed as it was hard to discern any difference between the AE-hits based on parameters or wave-form.

6.6.2 Human error

Great care was taken to reduce the amount of human error present in the code used, it was tested on different data sets, critically reviewed and revised during these past months. However, mistakes do happen and the code used might have had faults not picked up by the author.

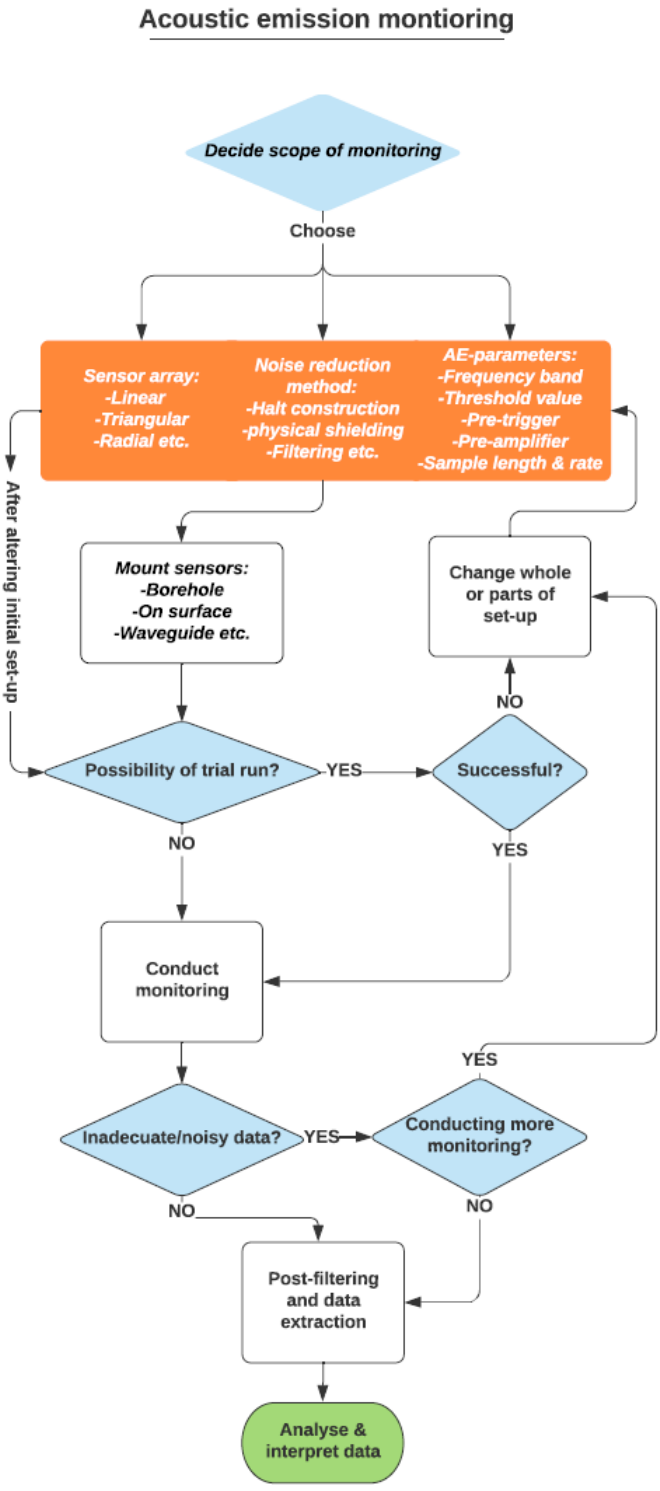

Figure 43: Flowchart indicating the steps needed to successfully conduct in-situ AE-monitoring based on information gathered in the relevant literature. (Created using lucid charts).

7 Conclusion

During this thesis a lot of aspects regarding use of acoustic emissions in the field have been discussed. Based on the statistical and parameter analysis conducted on data obtained from in-situ AE monitoring of hydraulic fracturing stress measurements tests and discussions related to source of acoustic emissions during jacking, problems occurring in the field and the potential use of AE to detect HJ during pre-excavation grouting the following conclusions can be drawn:

- The parameters related to HF and HJ1/2 indicated a trend towards a lower absolute energy and amplitude with each jacking cycle. This is opposite to what previous literature has shown.
- An increase in fracture size with each jacking cycle is thought to be related to an increase in AE-signal duration.
- An increase in AE-rate is seen close to the the perceived points related to fracture initiation, fracture reopening and closing. And the AE-rate data presented in this thesis is similar to that presented in previous literature.
- The source of acoustic signals during jacking is thought to be frictional resistance acting between asperities and fracture walls during structural movement caused by the jacking motion. It is postulated that the type of fracture infilling and/or fracture roughness and undulation will have an effect on the resulting acoustic signal strength as these parameters are directly related to a fractures frictional resistance.
- Future AE-monitoring programs should include source location and acoustic shielding. And attenuation reduction through the use of either a borehole or a wave-guide would be beneficial. It is of great importance that such a borehole has a good quality and that measures are put in place to reduce grout and/or water flow into the monitoring borehole. The seismic velocity of the rock mass should also be determined to allow for AE source location.
- Acoustic emission monitoring could, in theory, be a viable method for detecting hydraulic jacking during pre-excavation grouting when used together with other HJ-detecting methods (e.g. pressure and flow graphs). Doing this could help eliminate instances of false-positive HJ interpretations giving the project owner and contractor the ability to alter the grouting scheme to fit the project requirements.

It should be noted that whether hydraulic jacking was successfully monitored through the use of AE-sensors remain inconclusive. The AE-rate plots indicate that HJ was in fact recorded as these correlate nicely with the perceived points related to fracture initiation and reopening/closing. The parameter study on the other hand indicate that the recorded AE-hits were not resulting from hydraulic fracturing and/or jacking, based on the differences between the data and what previous literature. It is postulated that a different conclusion would have been drawn had the data not been so noisy.

8 Further research

In the future it would be interesting to see studies conducted on the following subjects:

- Test the use of AE-monitoring during pre-excavation grouting to check it's potential for detecting hydraulic jacking in-situ.
- Comparing the results from AE-monitoring with the PF-index created by Helene Strømsvik (Strømsvik et al. 2018).
- Compare AE monitoring in a borehole as oppose to using a wave-guide with respect to usefulness, signal strength, set-up time, cost etc.
- Testing the use of in-situ AE-monitoring on different lithologies and rock mass qualities and report on the major differences.
- Testing AE-monitoring on different grouting schemes with different pressure, grout mixtures, w/c-ratio etc.
- Study the impact liquid grout, and later solidifed grout, has on AE-wave attenuation compared to an open fracture with no infilling.
- Effect of fracture infilling and fracture roughness (jr/ja-values) on suitability for AE-monitoring of rock mass jacking.

References

Ashikhmen, V. A. & Pronina, L. E. (2001), 'Investigations of the penetrability of cement grout into a cavity having a small opening.', *Hydrotechnical Construction* **35**(8), 436–440.

Brantberger, M., Stille, H. & Eriksson, M. (2000), 'Controlling grout spreading in tunnel grouting — analyses and developments of the gin-method', *Tunnelling and Underground Space Technology* **15**(4), 343 – 352.
URL: *http://www.sciencedirect.com/science/article/pii/S0886779801000037*

Brown, E. T. & Hoek, E. (1978), Trends in relationships between measured in-situ stresses and depth, *in* 'International Journal of Rock Mechanics and Mining Sciences & Geomechanics Abstracts', Vol. 15, Pergamon, pp. 211–215.

Cai, M., Kaiser, P., Morioka, H., Minami, M., Maejima, T., Tasaka, Y. & Kurose, H. (2007), 'Flac/pfc coupled numerical simulation of ae in large-scale underground excavations', *International Journal of Rock Mechanics and Mining Sciences* **44**(4), 550 – 564.
URL: *http://www.sciencedirect.com/science/article/pii/S1365160906001481*

Codeglia, D., Dixon, N., Fowmes, G. J. & Marcato, G. (2017), 'Analysis of acoustic emission patterns for monitoring of rock slope deformation mechanisms', *Engineering Geology* **219**, 21–31.

Dehls, J. F., Olesen, O. & Rønning, J. S. (2011), 'Magnetisk og batymetrisk kartlegging ved vegprosjektet fv. 659 nordøyvegen, møre og romsdal.'.

Dixon, N., Hill, R. & Kavanagh, J. (2003), 'Acoustic emission monitoring of slope instability: development of an active waveguide system', *Proceedings of the Institution of Civil Engineers - Geotechnical Engineering* **156**(2), 83–95.
URL: *https://doi.org/10.1680/geng.2003.156.2.83*

Eriksson, M. & Stille., H. (2003), 'A method for measuring and evaluating the penetrability of grouts', *ASCE Geotech. Special Publ. (GSP)* **120**, 1326–1337.

Feng, X.-T., Young, R., Reyes-Montes, J., Aydan, Ö., Ishida, T., Liu, J.-P. & Liu, H.-J. (2019), 'Isrm suggested method for in situ acoustic emission monitoring of the fracturing process in rock masses', *Rock Mechanics and Rock Engineering* **52**(5), 1395–1414.

Ganerød, G. V. & Lutro, O. (2011), Berggrunnsgeologisk og strukturgeologisk kartlegging i forbindelse med prosjektet fv. 659 nordøyvegen, møre og romsdal., Technical report, Norges geologiske undersøkelse.

Gischig, V. S., Preisig, G. et al. (2015), Hydro-fracturing versus hydro-shearing: a critical assessment of two distinct reservoir stimulation mechanisms, *in* '13th ISRM International Congress of Rock Mechanics', International Society for Rock Mechanics and Rock Engineering.

Gothäll, R. & Stille, H. (2009), 'Fracture dilation during grouting', *Tunnelling and Underground Space Technology* **24**(2), 126 – 135.
URL: *http://www.sciencedirect.com/science/article/pii/S0886779808000564*

Grøv, E., Strømsvik, H. & Haugsand, M. H. (2020), 'Sementbasert berginjeksjon. sluttrapport fra prosjektet tight', *SINTEF Viten* .

Grøv, E., Funehag, J. & Janson, T. (2014), 'Rock mass grouting in sweden and norway a matter of cultural differences or factual causes?', *Geotechnical News* **32**, 41–51.

Grøv, E. & Woldmo, O. (2012), Modern pre-grouting technology in norway, pp. 805–815.

Gustafson, G. & Stille, H. (2005), 'Stop criteria for cement grouting', *Felsbau: Zeitschrift für Geomechanik und Ingenieurgeologie im Bauwesen und Bergbau* **25**(3), 62–68.

Haimson, B. & Cornet, F. (2003), 'Isrm suggested methods for rock stress estimation part 3: hydraulic fracturing (hf) and/or hydraulic testing of pre-existing fractures (htpf)', *International Journal of Rock Mechanics and Mining Sciences* **40**, 1011–1020.

Hardy, H. (2003), 'Acoustic emission/microseismic activity-volume 1: Principles, techniques and geotechnical applications, ed', *AA Balkema* .

Hardy, H. R. (1981), Applications of acoustic emission techniques to rock and rock structures: a state-of-the-art review, *in* 'Acoustic Emissions in Geotechnical Engineering Practice', ASTM International.

Harris, C. R., Millman, K. J., van der Walt, S. J., Gommers, R., Virtanen, P., Cournapeau, D., Wieser, E., Taylor, J., Berg, S., Smith, N. J., Kern, R., Picus, M., Hoyer, S., van Kerkwijk, M. H., Brett, M., Haldane, A., del Río, J. F., Wiebe, M., Peterson, P., Gérard-Marchant, P., Sheppard, K., Reddy, T., Weckesser, W., Abbasi, H., Gohlke, C. & Oliphant, T. E. (2020), 'Array programming with NumPy', *Nature* **585**(7825), 357–362.
URL: *https://doi.org/10.1038/s41586-020-2649-2*

Haugsand, M. H. et al. (2019), Hydraulic jacking and pressure distribution during rock mass grouting with cement based grouts, *in* 'ISRM 9th Nordic Grouting Symposium', International Society for Rock Mechanics and Rock Engineering.

Hoek, E. (2006), *Practical rock engineering.*
URL: *https://www.rocscience.com/learning/hoeks-corner/course-notes-books*

Hu, B. & Chan, R. (2014), A deployable stent for structural repair of water pipes.

Huck, P. & Koerner, R. (1981), Acoustic emission monitoring of soil and rock grouting, *in* 'Acoustic Emissions in Geotechnical Engineering Practice', ASTM International.

Huck, P., Waller, M., Koerner, R., McCabe, W. & Fowler, J. (1980), 'Monitoring and control of particulate grouting in rock', *Final Report to US Dept. of Transportation, Federal Highway Administration, Contract No. DOT-FH-11-9397 (E)* .

Hunter, J. D. (2007), 'Matplotlib: A 2d graphics environment', *IEEE Annals of the History of Computing* **9**(03), 90–95.

Ishida, T., Desaki, S., Yamashita, H., Inui, S., Naoi, M., Fujii, H. & Katayama, T. (2017), 'Injection of supercritical carbon dioxide into granitic rock and its acoustic emission monitoring', *Procedia Engineering* **191**, 476 – 482. ISRM European Rock Mechanics Symposium EUROCK 2017.
URL: *http://www.sciencedirect.com/science/article/pii/S1877705817323469*

Ishida, T., Kanagawa, T. & Uchita, Y. (2014), 'Acoustic emission induced by progressive excavation of an underground powerhouse', *International Journal of Rock Mechanics and Mining Sciences* **71**, 362 – 368.
URL: *http://www.sciencedirect.com/science/article/pii/S1365160914001993*

Jalaleddin, Y. R., Masakuni, T., Håkan, S. et al. (2013), Theoretical approaches in grouting fractures of the rock mass: Theories and applications, *in* '47th US Rock Mechanics/Geomechanics Symposium', American Rock Mechanics Association.

Karlsson, K. I. & Grob, C. (2017), 'Fv. 659 nordøyvegen, fjørtoftfjordtunnelen, ingeniørgeologisk rapport for konkurransegrunnlag', pp. 0 – 58.

Koerner, R., McCabe, W. & Lord, A. (1981), 'Overview of acoustic emission monitoring of rock structures', *Rock mechanics* **14**(1), 27–35.

Le Bot, A. (2017), Noise of sliding rough contact, *in* 'Journal of Physics: Conference Series', Vol. 797, IOP Publishing, p. 012006.

Liu, X., Han, M., Li, X., Cui, J. & Liu, Z. (2020), 'Elastic wave attenuation characteristics and relevance for rock microstructures', *Journal of Mining Science* **56**(2), 216–225.

Lombardi, G. & Deere, D. (1993), 'Grouting design and control using the gin principle', *International water power & dam construction* **45**(6), 15–22.

Lopez-Comino, J. A., Cesca, S., Heimann, S., Grigoli, F., Milkereit, C., Dahm, T. & Zang, A. (2017), 'Characterization of hydraulic fractures growth during the äspö hard rock laboratory experiment (sweden)', *Rock Mechanics and Rock Engineering* **50**(11), 2985–3001.

Mann, H. B. & Whitney, D. R. (1947), 'On a test of whether one of two random variables is stochastically larger than the other', *The annals of mathematical statistics* pp. 50–60.

Mistras group (2017), *Micro-SMH SYSTEM USER MANUAL*, Physical acoustics corporation.

Myrvang, A. M. (1983), 'Practical use of rock stress and deformation measurements', **2**.

NGI (2015), *Using the Q-system: Rock mass classification and support design*, NGI. **URL:** *https://www.ngi.no/eng/Services/Technical-expertise/Engineering-geology-and-rock-mechanics/Q-system*

Niemz, P., Cesca, S., Heimann, S., Grigoli, F., von Specht, S., Hammer, C., Zang, A. & Dahm, T. (2020), 'Full-waveform-based characterization of acoustic emission activity in a mine-scale experiment: a comparison of conventional and advanced hydraulic fracturing schemes', *Geophysical Journal International* **222**(1), 189–206.

NVE (2017), Nves innstilling – søknad om konsesjon for løkjelsvatn kraftverk i etne kommune, hordaland, Technical report, Olje- og energidepartementet.

Ødegaard, H. & Nilsen, B. (2021), 'Rock stress measurements for unlined pressure tunnels: A true triaxial laboratory experiment to investigate the ability of a simplified hydraulic jacking test to assess fracture normal stress', *Rock Mechanics and Rock Engineering* pp. 1–21.

Plenkers, K., Kwiatek, G., Nakatani, M. & Dresen, G. (2010), 'Observation of seismic events with frequencies f¿ 25 khz at mponeng deep gold mine, south africa', *Seismological Research Letters* **81**(3), 467–479.

Prop. 140 S (2016-2017), *Finansiering av prosjektet fv 659 Nordøyvegen i Møre og Romsdal*, Det kongelige samferdseldepartement, Oslo.

Rafi, J. Y. (2014), Study of pumping pressure and stop criteria in grouting of rock fractures, PhD thesis, Architecture and the Built Environment, KTH Royal Institute of Technology.

Rafi, J. Y. & Stille, H. (2014), 'Control of rock jacking considering spread of grout and grouting pressure', *Tunnelling and Underground Space Technology* **40**, 1 – 15.
URL: *http://www.sciencedirect.com/science/article/pii/S0886779813001351*

Rafi, J. Y. & Stille, H. (2015), 'Basic mechanism of elastic jacking and impact of fracture aperture change on grout spread, transmissivity and penetrability', *Tunnelling and Underground Space Technology* **49**, 174–187.

Ramberg, I. B., Bryhni, I., Nøttvedt, A. & (ed.) Rangnes, K. (2013), *Landet blir til - Norges geologi*, second edn, Norges geologiske forening.

Salmon, M., Short, S. & Kennedy, R. (1992), Strong motion duration and earthquake magnitude relationships, Technical report, Lawrence Livermore National Lab., CA (United States); EQE International, Inc ....

Skanska (2018), 'Skanska har signert kontrakt om bygging av nordøyvegen'.
URL: *https://www.skanska.no/hvem-vi-er/media/pressemeldinger/228404/Skanska-har-signert-kontrakt-om-bygging-av-Nordoyvegen*

Skjetne, P. & Mo, S. (2016), Numerical simulations of grout flow in simplified geometries., *in* '8th Nordic Grouting Symposium', Oslo, Norway.

SKL (2018), Løkjelsvatn kraftverk - informasjonsbrosjyre, Technical report, Sunnhordaland Kraftlag AS.

Stille, H., Gustafson, G. & Hassler, L. (2012), 'Application of new theories and technology for grouting of dams and foundations on rock', *Geotechnical and Geological Engineering* **30**(3), 603–624.

Stroisz, A., Pradhan, S., Jordan, M., Cerasi, P., Walle, L., Bauer, A., Stenebråten, J., Stanchits, S., Will, R. et al. (2016), Monitoring of fracture reopening in sandstones, *in* '50th US Rock Mechanics/Geomechanics Symposium', American Rock Mechanics Association.

Strømsvik, H. (2019), 'The significance of hydraulic jacking for grout consumption during high pressure pre-grouting in norwegian tunnelling', *Tunnelling and Underground Space Technology* **90**, 357 – 368.
URL: *http://www.sciencedirect.com/science/article/pii/S0886779819300136*

Strømsvik, H., Morud, J. C. & Grøv, E. (2018), 'Development of an algorithm to detect hydraulic jacking in high pressure rock mass grouting and introduction of the pf index', *Tunnelling and Underground Space Technology* **81**, 16 – 25.
URL: *http://www.sciencedirect.com/science/article/pii/S0886779817309823*

Svečko, R., Kusić, D., Kek, T., Sarjaš, A., Hančič, A. & Grum, J. (2013), 'Acoustic emission detection of macro-cracks on engraving tool steel inserts during the injection molding cycle using pzt sensors', *Sensors (Basel, Switzerland)* **13**, 6365–6379.

Terry, M. P. & Robinson, P. (2003), 'Evolution of amphibolite-facies structural features and boundary conditions for deformation during exhumation of high-and ultrahigh-pressure rocks, nordøyane, western gneiss region, norway', *Tectonics* **22**(4).

Van Rossum, G. (2020), *The Python Library Reference, release 3.8.2*, Python Software Foundation.

Virtanen, P., Gommers, R., Oliphant, T. E., Haberland, M., Reddy, T., Cournapeau, D., Burovski, E., Peterson, P., Weckesser, W., Bright, J. et al. (2020), 'Scipy 1.0: fundamental algorithms for scientific computing in python', *Nature methods* **17**(3), 261–272.

Yaghoobi Rafi, J. (2013), Design approaches for grouting of rock fractures; Theory and practice, PhD thesis, KTH Royal Institute of Technology.

YIT (2018), 'Yit norge bygger løkjelsvatn kraftverk'.
URL: *https://www.yit.no/media/jolstra4*

Zang, A., Stephansson, O., Stenberg, L., Plenkers, K., Specht, S., Milkereit, C., Schill, E., Kwiatek, G., Dresen, G., Zimmermann, G., Dahm, T. & Weber, M. (2016), 'Hydraulic fracture monitoring in hard rock at 410 m depth with an advanced fluid-injection protocol and extensive sensor array', *Geophysical Journal International* **208**(2), 790–813.
URL: *https://doi.org/10.1093/gji/ggw430*

Zhang, J. (2018), 'Investigation of relation between fracture scale and acoustic emission time-frequency parameters in rocks', *Shock and Vibration* **2018**.

Zou, L., Håkansson, U., Cvetkovic, V. et al. (2018), Impacts of elastic jacking on rock grouting, *in* 'ISRM International Symposium-10th Asian Rock Mechanics Symposium', International Society for Rock Mechanics and Rock Engineering.

A Code

A.1 Code to extract AE-data and conduct statistical analysis

```
#Import different modules and libraries used in the code:
import os
import matplotlib.pyplot as plt
import numpy as np
import re
import statistics
import scipy
from scipy import stats
from Outlier import stat


def atoi(text):#Function that converts text (ascii) to number (int)
    return int(text) if text.isdigit() else text

def natural_keys(text): #Function that sorts input in descending order.
    return [ atoi(c) for c in re.split(r'(\d+)', text) ]

#Creates empty lists for respective AE-parameters
rise=[] #Risetime
cnt=[] #Count
dur=[] #duration
amp=[] #Amplitude
abs_ener=[] #abs_ener2
#Path for placement of AE-file containing HJ data
path="C:\\Users\\Christoffer Surdal\\Desktop\\HF"

for root,dir,files in os.walk(path): #Return tuples of  root, directory and files
    files.sort(key=natural_keys) #Sorts the files in numerical order
    for filename in files: #Iteralte over files in the file tuple
        file_path=str(os.path.join(path,filename)) #Joins the filename and path,
        f=open(file_path,"r") #Opens file in "read" mode
        for lines in f: #Iterate over lines in file.
            x= lines.strip() #Remove white/empty lines
            if x: #If value in line continue
                x=x.split() #Splits into indexes on spaces (empty)
                if x[0]=="1" or x[0]=="2": #Checks if index 0
```

```
    contains a 1 or 2 (since these are the lines cotaining AE-info)
37                  #Extracts the relevant AE-parameters and
    appends them to their respective list.
38                  rise.append(float(x[3]))
39                  cnt.append(float(x[4]))
40                  dur.append(float(x[6]))
41                  amp.append(float(x[7]))
42                  abs_ener.append(float(x[11]))
43
44          #Closes the file.
45          f.close()
46
47 #The following code does exactly the same as the above mentioned
    code
48 #Only for the AE-files related to the HJ
49 rise2=[]
50 cnt2=[]
51 dur2=[]
52 amp2=[]
53 abs_ener2=[]
54
55 path="C:\\Users\\Christoffer Surdal\\Desktop\\HJ1"
56
57 for root,dir,files in os.walk(path):
58     files.sort(key=natural_keys)
59     for filename in files:
60         file_path=str(os.path.join(path,filename))
61         f=open(file_path,"r")
62
63         for lines in f:
64             x= lines.strip()
65             if x:
66                 x=x.split()
67
68                 if x[0]=="1" or x[0]=="2":
69                     rise2.append(float(x[3]))
70                     cnt2.append(float(x[4]))
71                     dur2.append(float(x[6]))
72                     amp2.append(float(x[7]))
73                     abs_ener2.append(float(x[11]))
74
75
76         f.close()
77
78 rise3=[]
79 cnt3=[]
80 dur3=[]
```

```
amp3=[]
abs_ener3=[]

#The following code does exactly the same as the above mentioned
    code
#Only for the AE-files related to the HJ2
path="C:\\Users\\Christoffer Surdal\\Desktop\\Jekk2_fin"

for root,dir,files in os.walk(path):
    files.sort(key=natural_keys)
    for filename in files:
        file_path=str(os.path.join(path,filename))
        f=open(file_path,"r")

        for lines in f:
            x= lines.strip()
            if x:
                x=x.split()

                if x[0]=="1" or x[0]=="2":
                    rise3.append(float(x[3]))
                    cnt3.append(float(x[4]))
                    dur3.append(float(x[6]))
                    amp3.append(float(x[7]))
                    abs_ener3.append(float(x[11]))


        f.close()


rise4=[]
cnt4=[]
dur4=[]
amp4=[]
abs_ener4=[]

#The following code does exactly the same as the above mentioned
    code
#Only for the AE-files related to the noise
path="C:\\Users\\Christoffer Surdal\\Desktop\\Noise"

for root,dir,files in os.walk(path):
    files.sort(key=natural_keys)
    for filename in files:
        file_path=str(os.path.join(path,filename))
        f=open(file_path,"r")

```

```
        for lines in f:
            x= lines.strip()
            if x:
                x=x.split()

                if x[0]=="1" or x[0]=="2":
                    rise4.append(float(x[3]))
                    cnt4.append(float(x[4]))
                    dur4.append(float(x[6]))
                    amp4.append(float(x[7]))
                    abs_ener4.append(float(x[8]))


        f.close()

#Prints length of data related to HF, HJ1, HJ2 and noise to check
    how many AE-hits
#Were used in the analysis
print(len(rise))
print(str(len(rise2)))
print(str(len(rise3)))
print(str(len(rise4)))

#Prints the statistical five number summary for HF, HJ1, HJ2 and
    noise.
#No number= HF, 2 = HJ1 3= HJ2 4=noise
print(stat(abs_ener,abs_ener2,abs_ener3,abs_ener4))
print(stat(amp,amp2,amp3,amp4))
print(stat(cnt,cnt2,cnt3,cnt4))
print(stat(dur,dur2,dur3,dur4))
print(stat(rise,rise2,rise3,rise4))



#Creates a figure with five stacked sub figures.
fig, (axs1,axs2,axs3,axs4,axs5) = plt.subplots(5, 1)

#Create figure title and labels.
fig.suptitle("Box plots for different AE-parameters related to
    hydraulic fracturing (HF) and jacking (HJ)")
labels=["Noise","HJ2","HJ1","HF"]

#Creates lists containing each parameter from the respective
    datasets.
pl1=[abs_ener4,abs_ener3,abs_ener2,abs_ener]
pl2=[amp4,amp3,amp2,amp]
```

```
pl3=[cnt4,cnt3,cnt2,cnt]
pl4=[dur4,dur3,dur2,dur]
pl5=[rise4,rise3,rise2,rise]



#Create box plots (bp) of plot lists pl1 - pl5
bp1 = axs1.boxplot(pl1,0,"", patch_artist=True,labels=labels,vert=
    False)
bp2 = axs2.boxplot(pl2,0,"", patch_artist=True,labels=labels,vert=
    False)
bp3 = axs3.boxplot(pl3,0,"", patch_artist=True,labels=labels,vert=
    False)
bp4 = axs4.boxplot(pl4,0,"", patch_artist=True,labels=labels,vert=
    False)
bp5 = axs5.boxplot(pl5,0,"", patch_artist=True,labels=labels,vert=
    False)


#Change the color of the median line and face color for every
    boxplot.
for box in bp1['boxes']:
    for med in bp1["medians"]:
        box.set(facecolor = 'darkred')
        med.set(color="white")

for box in bp2['boxes']:
    for med in bp2["medians"]:
        box.set(facecolor = 'dodgerblue' )
        med.set(color="white")

for box in bp3['boxes']:
    for med in bp3["medians"]:
        box.set(facecolor = 'green' )
        med.set(color="white")

for box in bp4['boxes']:
    for med in bp4["medians"]:
        box.set(facecolor = 'navy')
        med.set(color="white")

for box in bp5['boxes']:
    for med in bp5["medians"]:
        box.set(facecolor = 'orange' )
        med.set(color="white")


```

```
#Change color and style of grid behind box-plots.
axs1.xaxis.grid(True, linestyle='-', which='major', color='lightgrey',
                alpha=0.5)

axs2.xaxis.grid(True, linestyle='-', which='major', color='lightgrey',
                alpha=0.5)

axs3.xaxis.grid(True, linestyle='-', which='major', color='lightgrey',
                alpha=0.5)

axs4.xaxis.grid(True, linestyle='-', which='major', color='lightgrey',
                alpha=0.5)

axs5.xaxis.grid(True, linestyle='-', which='major', color='lightgrey',
                alpha=0.5)


#Sets title and  x-axis label for all the subplots.
axs1.set(title="Spread absolute energy",axisbelow=True,)
axs1.set_xlabel("Absolute energy (aJ)")

axs2.set(title="Spread amplitude",axisbelow=True)
axs2.set_xlabel("Amplitude (dB)")

axs3.set(title="Spread AE count",axisbelow=True,)
axs3.set_xlabel("Number of threshold crossings (count)")

axs4.set(title="Spread duration",axisbelow=True)
axs4.set_xlabel("Duration ($\mu$s)")

axs5.set(title="Spread rise time",axisbelow=True)
axs5.set_xlabel("Risetime ($\mu$s)")


#Change limits (size) of x-axis for all subplots to fit the data
start, end = axs1.get_xlim()
axs1.xaxis.set_ticks(np.arange(0, end, 1))

start, end = axs2.get_xlim()
axs2.xaxis.set_ticks(np.arange(25, end,1))

start, end = axs3.get_xlim()
```

```
axs3.xaxis.set_ticks(np.arange(0, end, 1))

start, end = axs4.get_xlim()
axs4.xaxis.set_ticks(np.arange(0, end,50))

start, end = axs5.get_xlim()
axs5.xaxis.set_ticks(np.arange(0, end,5))

#adjusts the horisontal space between subplots
plt.subplots_adjust(hspace=1)

#Shows plot on the monitor.
plt.show()
```

A.2 Code to calculate statistical five number summary

```
import numpy as np #Imports the numpy library
import scipy #imports science python library (scipy)
from scipy import stats #Imports the statistics module from scipy
import statistics #Imports statistics library


def stat(x,y,z,n): #Defines function stat
    a_x = np.array(x)  #Creates an array from input x

    upper_quartile_x = np.percentile(a_x, 75)#Extracts the upper
   percentile from a_x
    lower_quartile_x = np.percentile(a_x, 25)#Extracts the lower
   percentile from a_x


    med_x=statistics.median(x) #Finds median of array x
    iqr_x=upper_quartile_x-lower_quartile_x #Calculates inter-
   quartile range

    max_x = a_x[a_x<=upper_quartile_x+1.5*iqr_x].max() #Finds max
   value (i.e upper whisker)
    min_x = a_x[a_x>=lower_quartile_x-1.5*iqr_x].min() #Finds min
   value (i.e lower whisker)
    #
   ------------------------------------------------------------------------

    #Following code does the same as above mentioned code but for
   input y
    a_y = np.array(y)

    upper_quartile_y = np.percentile(a_y, 75)
```

```
    lower_quartile_y = np.percentile(a_y, 25)

    med_y=statistics.median(y)
    iqr_y=upper_quartile_y-lower_quartile_y
    max_y = a_y[a_y<=upper_quartile_y+1.5*iqr_y].max()
    min_y = a_y[a_y>=lower_quartile_y-1.5*iqr_y].min()
    #
    ------------------------------------------------------------------------

    #Following code does the same as above mentioned code but for
    input z
    a_z = np.array(z)

    upper_quartile_z = np.percentile(a_z, 75)
    lower_quartile_z = np.percentile(a_z, 25)

    med_z=statistics.median(z)
    iqr_z=upper_quartile_z-lower_quartile_z
    max_z = a_z[a_z<=upper_quartile_z+1.5*iqr_z].max()
    min_z = a_z[a_z>=lower_quartile_z-1.5*iqr_z].min()

    #
    ------------------------------------------------------------------------

    #Following code does the same as above mentioned code but for
    input z
    a_n = np.array(n)

    upper_quartile_n = np.percentile(a_n, 75)
    lower_quartile_n = np.percentile(a_n, 25)

    med_n=statistics.median(n)
    iqr_n=upper_quartile_n-lower_quartile_n
    max_n = a_n[a_n<=upper_quartile_n+1.5*iqr_n].max()
    min_n = a_n[a_n>=lower_quartile_n-1.5*iqr_n].min()


    #Create text strings appended to values r1-r4 for each input,
    #representing min, Q1, med, Q3 and max.
    r1=(str(min_x)+" | " +str(lower_quartile_x)+" | "+str(med_x)+"
    | "+str(upper_quartile_x)+" | "+str(max_x)+"\n")
    r2=(str(min_y)+" | " +str(lower_quartile_y)+" | "+str(med_y)+"
    | "+str(upper_quartile_y)+" | "+str(max_y)+"\n")
    r3=(str(min_z)+" | " +str(lower_quartile_z)+" | "+str(med_z)+"
    | "+str(upper_quartile_z)+" | "+str(max_z)+"\n")
    r4=(str(min_n)+" | " +str(lower_quartile_n)+" | "+str(med_n)+"
    | "+str(upper_quartile_n)+" | "+str(max_n)+"\n")
```

```
61
62      #Conducts mann-whitney U test comparing different input
        parameters. In this case:
63      t2=scipy.stats.mannwhitneyu(x,y) #HF/HJ1
64      t1=scipy.stats.mannwhitneyu(x,z) #HF/HJ2
65      t3=scipy.stats.mannwhitneyu(y,z) #HJ1/HJ2
66      t4=scipy.stats.mannwhitneyu(x,n) #HF/Noise
67      t5=scipy.stats.mannwhitneyu(y,n) #HJ1/Noise
68      t6=scipy.stats.mannwhitneyu(z,n) #HJ2/Noise
69
70      #Creates print line 1 consisting of r1 - r4
71      print1=(str(r1) + str(r2) +str(r3)+str(r4)+"\n")
72      #Creates print line for Mann-whitney U test results t1 - t6
73      print2=(str(t1)+"HF/HJ1\n"+str(t2)+"HF/HJ2\n"+str(t3)+"HJ1/HJ2\
        n"+str(t4)+"HF/Noise\n"+str(t5)+"HJ1/Noise\n"+str(t6)+"HJ2/Noise
        \n")
74
75      #Returns printline 1 and print line 2
76      return(str(print1) + str(print2))
```

A.3 Fourier transform function

```
import scipy #Imports rfft and fft from Scipy
from scipy.fft import rfft, rfftfreq

def fourier(wave): #Creates function fourier that accepts an AE-wave array
    N=10240 #Number of samples.
    SR=5000 # Sample rate in kHZ
    yf = rfft(wave) #Calculates y axis of fourier transform
    xf = rfftfreq(N, 1/SR) #Calculates x-axis of fourier transform.
    #xf only accept number of samples and 1/sample rate (Or alternatively sample interval (s))

    return(yf,xf) #Returns values for yf and xf:
#Source of scipy documentation: https://docs.scipy.org/doc/scipy/reference/tutorial/fft.html
```

A.4 Fourier transform iteration code

```
1
2
3 #The following code iterates over every AE-wave file, extracts wave
      parameters and feeds them to a fourier
4 #Transform that is then printed out after transforming the wave
     from the time domain to the frequency domain.
5 #Imports libraries and modules used in this code:
6 import os
7 import matplotlib.pyplot as plt
8 import numpy as np
9 from matplotlib.ticker import (MultipleLocator, FormatStrFormatter,
      AutoMinorLocator)
10 import re
11 from scipy import stats
12
13 #Imports fourier code from fourier.py
14 from fourier import fourier
15
16 def atoi(text):#Function that converts text (ascii) to number (int)
17     return int(text) if text.isdigit() else text
18
19 def natural_keys(text): #Function that sorts input in descending
     order.
20     return [ atoi(c) for c in re.split(r'(\d+)', text) ]
21 wave1=[]
22
23
24
25
26 path="C:\\Users\\Christoffer Surdal\\Desktop\\HF_waves"
27 for root,dir,files in os.walk(path): #Return tuples of  root,
     directory and files
28     files.sort(key=natural_keys) #Sorts the files in numerical
     order
29     for filename in files: #Iteralte over files in the file tuple
30         file_path=str(os.path.join(path,filename)) #Joins the
     filename and path,
31         f=open(file_path,"r") #Opens file in "read" mode
32         for lines in f: #Iterate over lines in file.
33             x= lines.strip() #Remove white/empty lines
34             if x: #If value in line continue
35                 x=x.split() #Splits into indexes on spaces (empty)
36             if "-" in x[0] or "0" in x[0]: #Checks if - or 0 in
     first integer as these lines contain information regarding the
     wave.
```

```
                wave1.append(x[0]) #Appends related wave
    information to wave file
    f.close()#Closes file

#Same as above mentioned code but for HJ1 waves.
wave2=[]

path="C:\\Users\\Christoffer Surdal\\Desktop\\HJ1_waves"

for sub,dir,files in os.walk(path):
    files.sort(key=natural_keys)
    for filename in files:
        fil=str(os.path.join(path,filename))
        f=open(fil,"r")

    for lines in f:
        x= lines.strip()
        if x:
            x=x.split()
            if "-" in x[0] or "0" in x[0]:
                wave2.append(x[0])
    f.close()

#Same as above mentioned code but for HJ2 waves.
wave3=[]


path="C:\\Users\\Christoffer Surdal\\Desktop\\HJ2_waves\\"

for sub,dir,files in os.walk(path):
    files.sort(key=natural_keys)
    for filename in files:
        fil=str(os.path.join(path,filename))
        f=open(fil,"r")

    for lines in f:
        x= lines.strip()
        if x:
            x=x.split()
            if "-" in x[0] or "0" in x[0]:
                wave3.append(x[0])
    f.close()

#Same as above mentioned code but for Noise waves.
wave4=[]

path="C:\\Users\\Christoffer Surdal\\Desktop\\Noise_waves\\"
```

```
#path="C:\\Users\\Christoffer Surdal\\Desktop\\Waves jekk\\"
for sub,dir,files in os.walk(path):
    files.sort(key=natural_keys)
    for filename in files:
        fil=str(os.path.join(path,filename))
        f=open(fil,"r")

    for lines in f:
        x= lines.strip()
        if x:
            x=x.split()
            if "-" in x[0] or "0" in x[0]:
                wave4.append(x[0])
    f.close()

wave1=[float(i) for i in wave1] #Converts every index in list wave1
    to float.
wave2=[float(i) for i in wave2] #Converts every index in list wave2
    to float.
wave3=[float(i) for i in wave3] #Converts every index in list wave3
    to float.
wave4=[float(i) for i in wave4] #Converts every index in list wave4
    to float.

#Conducts fourier analysis on each wave array, extracting X and y
   coordinates.
fourier_y_ax1, fourier_x_ax1 =fourier(wave1)
fourier_y_ax2, fourier_x_ax2 =fourier(wave2)
fourier_y_ax3, fourier_x_ax3 =fourier(wave3)
fourier_y_ax4, fourier_x_ax4 =fourier(wave4)

#Creates a figure with 4 stacked subplots. Every plot shares the
   same x-axis
fig, (ax1,ax2,ax3,ax4) = plt.subplots(4,1, sharex=True)
#Alter the horizontal spacing for the sub-plots
fig.subplots_adjust(hspace=0.5)
#Change the apparence of ticks on x-axis
ax1.xaxis.set_tick_params(which='both', labelbottom=True)
ax1.xaxis.set_minor_locator(AutoMinorLocator()) #automatically
   locate minor ticks

#Creates fourier line plot from x-axis value and y-axis value
   received from fourier transform for HF_waves
ax1.plot(fourier_x_ax1,np.abs(fourier_y_ax1),"r",linewidth=0.5)
#Formats ticks present in plot.
ax1.tick_params(which='both', width=0.5)
ax1.tick_params(which='major', length=7)
```

```
122 ax1.tick_params(which='minor', length=4)
123
124 #Assigns labels and title.
125 ax1.set_xlabel("Frequency (kHz)")
126 ax1.set_ylabel("Amplitude")
127 ax1.set_title("Hydraulic fracturing frequency spectra")
128
129 #Following code does the same as above but for HJ1_waves
130 ax2.xaxis.set_tick_params(which='both', labelbottom=True)
131 ax2.xaxis.set_minor_locator(AutoMinorLocator())
132 #Plots frequency spectra of noise (ax2)
133 ax2.plot(fourier_x_ax2,np.abs(fourier_y_ax2),"r",linewidth=0.5)
134 #Formats ticks present in plot.
135 ax2.tick_params(which='both', width=0.5)
136 ax2.tick_params(which='major', length=7)
137 ax2.tick_params(which='minor', length=4)
138 #Assigns labels and title.
139 ax2.set_xlabel("Frequency (kHz)")
140 ax2.set_ylabel("Amplitude")
141 ax2.set_title("Hydraulic jacking 1 frequency spectra")
142
143 #Following code does the same as above but for HJ2_waves
144 ax3.xaxis.set_tick_params(which='both', labelbottom=True)
145 ax3.xaxis.set_minor_locator(AutoMinorLocator())
146 #Plots frequency spectra of noise (ax2)
147 ax3.plot(fourier_x_ax3,np.abs(fourier_y_ax3),"r",linewidth=0.5)
148
149 #Formats ticks present in plot.
150 ax3.tick_params(which='both', width=0.5)
151 ax3.tick_params(which='major', length=7)
152 ax3.tick_params(which='minor', length=4)
153
154 #Assigns labels and title.
155 ax3.set_xlabel("Frequency (kHz)")
156 ax3.set_ylabel("Amplitude")
157 ax3.set_title("Hydraulic jacking 2 frequency spectra")
158
159 #Following code does the same as above but for Noise_waves
160 ax4.xaxis.set_tick_params(which='both', labelbottom=True)
161 ax4.xaxis.set_minor_locator(AutoMinorLocator())
162 #Plots frequency spectra of noise (ax2)
163 ax4.plot(fourier_x_ax4,np.abs(fourier_y_ax4),"r",linewidth=0.5)
164
165 #Formats ticks present in plot.
166 ax4.tick_params(which='both', width=0.5)
167 ax4.tick_params(which='major', length=7)
168 ax4.tick_params(which='minor', length=4)
```

```
169
170 #Assigns labels and title.
171 ax4.set_xlabel("Frequency (kHz)")
172 ax4.set_ylabel("Amplitude")
173 ax4.set_title("Noise frequency spectra")
174
175 #Sets title of figure
176 fig.suptitle("Frequency domain of AE-hits from hydraulic fractures
       (HF), jacking (HJ) and noise")
177
178
179 start, end = ax1.get_xlim()
180 #Finds axis limits
181
182
183 #Shows plots on terminal
184 plt.show()
```

A.5 Frequency domain and time domain plot code

```
1
2  import os
3  import matplotlib.pyplot as plt
4  from scipy.fft import rfft, rfftfreq
5  import numpy as np
6  from matplotlib.ticker import (MultipleLocator, FormatStrFormatter,
       AutoMinorLocator)
7  import re
8
9  def atoi(text):
10     return int(text) if text.isdigit() else text
11
12 def natural_keys(text):
13     return [ atoi(c) for c in re.split(r'(\d+)', text) ]
14
15 #Path for wave file
16 path="C:\\Users\\Christoffer Surdal\\Desktop\\Jekk2_wav"
17
18         wave=[] #Creates empty lists for wave parameters duration
       and
19         Dur=[]
20
21 for root,dir,files in os.walk(path): #Return tuples of  root,
       directory and files in path
22     files.sort(key=natural_keys) #Sorts the files in numerical
       order
23     for filename in files: #Iteralte over files in the file tuple
24         file_path=str(os.path.join(path,filename)) #Joins the
       filename and path,
25         f=open(file_path,"r") #Opens file in "read" mode
26
27         for lines in f: #Iterate over lines in file.
28             x= lines.strip() #Remove white/empty lines
29             if x: #If value in line continue
30                 x=x.split() #Splits into indexes on spaces (empty)
31                     if "-" in x[0] or "0" in x[0]: #Checks if - or
       0 in first integer as this is related to wave data
32                     wave.append(x[0]) #Appends wave parameters to
       wave list.
33                 if "TIME:" in x[0]: #Checks if TIME in first
       integer
34                     Time=str(x[1])# If true append string of second
        integer to time (this is start time the AE-wave)
35
36
```

```
37
38
39          i=0
40          while i<len(wave): #Checks if i is less than lenght of wave
41              if len(Dur) == 0: #If true and if lenght of duration is
     equal to 0
42                  Dur.append(float(0.0000002000)) #Then one sample
    interval is appended to duration
43                  i=i+1 #I is increased by 1
44              else: #If duration is longer than 0
45                  x=Dur[i-1]+float(0.0000002000) #Then x is equal to
    the previous duration + one sample interval
46                  Dur.append(x) #x is then appended to dur
47                  i=i+1 #i is increased by one
48                  #This code calculates total duration of the AE-wave
49
50          wave=[float(i) for i in wave] #Change every integer in wave
     to float
51
52          N=len(wave) #finds length of wave
53          SR=5000 #Sample rate (to get output in kHz)
54
55          yf = rfft(wave) #Conducts fourier transform on wave
56          xf = rfftfreq(N, 1 / SR)
57
58          #Creates a figure with two stacked sup-plots
59          fig, (ax1, ax2) = plt.subplots(2, 1)
60           #Adjusts horizontal space between subplots
61          fig.subplots_adjust(hspace=0.35)
62
63          #Plots result from fourier transform i.e wave in frequency
    spectra
64          ax1.plot(xf,np.abs(yf),"r",linewidth=0.5)
65
66          #Changes x-axis to fill in ticks automatically when zoomed
67          ax1.xaxis.set_minor_locator(AutoMinorLocator())
68          #Change apparence of ticks
69          ax1.tick_params(which='both', width=0.5)
70          ax1.tick_params(which='major', length=7)
71          ax1.tick_params(which='minor', length=4)
72          #Set axis labels
73          ax1.set_xlabel("Frequency (Khz)")
74          ax1.set_ylabel("Amplitude (V)")
75
76          #Plots duration of wave on x-axis and amplitude on y-axis (
    i.e. wave in time domain)
77          ax2.plot(Dur,wave,"r",linewidth=0.5)
```

```
78          #Sets axis labels
79          ax2.set_xlabel("Time (s)")
80          ax2.set_ylabel("Amplitude (V)")
81          #Sets figure title
82          fig.suptitle("Frequency- and time domain. Wave origin: HF \
    n" +str(filename))
83          #Changes white space around figure so that it is tight
84          fig.tight_layout()
85
86          #Closes file
87          f.close()
88          #Shows plot on terminal
89          plt.show()
```

A.6 AE rate calculation code

```
1
2  import datetime #Imports modules used from python
3  import time
4  def count(list1, start, end): #Defines function count
5      c = 0 #Sets count to 0
6      for x in list1: #iterates over values in list1
7          #Checks if x in list one is between start and end
8          if float(round(x))>= float(start) and float(round(x))<=
       float(end):
9              c+= 1 #If true count is increased by 1
10     return c #Return count
11
12 def ae(fil): #Defines function AE that accepts an AE file
13     f=open(fil,"r") #Opens file in read mode
14
15     time_file=[] #Create empty list for time
16     start_time=0
17     for lines in f: #Iterate over lines in F
18         if ":" in lines: #If : in line
19             y=lines.split() #removes spaces at beginning and end
20         x= lines.strip()#remove spaces at beginning and end
21         if x: #Checks if info in integer x
22             x=x.split() #If true splits list into integers
23             if x[0]=="1" or x[0]=="2": #Checks if 1 or 0 in first
       integer
24                 time_file.append(float(x[1])) #If true time is
       integer 1
25
26
27
28
29     start_time=(y[3]) #Start time is equal to integer 3 in list y
30     #Creates date time object of start_time in format H:M:S
31     date_time = datetime.datetime.strptime(start_time, "%H:%M:%S")
32     #Extract time from date time object by removing year, month,
       day
33     time=date_time-datetime.datetime(1900,1,1)
34     #Uses function seconds total to tranfrom time from H:M:S to S
35     seconds_tot=time.total_seconds()
36
37
38
39     #Time difference between HF file and AE file (project specific)
40     time_dif=(284)
41
```

```
42      AE_rate=[]#Creates empty list for AE_rate
43      time=[]#Creates empty time list
44      sec=0 #initiate sec at 0
45
46      if len(time_file)>0: #Checks that time file contains info
47          while sec<=(float(time_file[-1])+15): #loop runs as long as
        sec is within value at the end of time_file + 15 sec
48              #append AE rate by sending time file into function
    count and counting every AE-hit within +/- 2 seconds
49              AE_rate.append(count(time_file,sec-2,sec+2))
50              #Create time z which is occurence of rate spike. Z
    coonsists of start time + sec + time difference
51              z=datetime.timedelta(seconds=seconds_tot+sec+time_dif)
52              #Remove micro seconds from Z, left with only seconds
53              x = z - datetime.timedelta(microseconds=z.microseconds)
54
55              time.append(x)#Appends seconds to time
56              sec=sec+5#Increases sec with 5 i.e. count AE-hits the
    next five seconds
57
58      return(AE_rate,time)#Returns AE_rate and time files
59      f.close() #Closes file
```

A.7 AE-file and HF-file plot code

```
1
2  #Imports used modules and libraries
3  from splitt import splitt
4  from AE import ae
5  import os
6  import matplotlib.pyplot as plt
7  import matplotlib.dates as dates
8  from plot_pf import plot_splitt
9  import datetime
10 import time
11 import numpy as np
12 import matplotlib
13 import re
14 import matplotlib.ticker as ticker
15 from matplotlib.ticker import (MultipleLocator, FormatStrFormatter,
       AutoMinorLocator)
16 import math
17
18
19 def atoi(text):#Function that converts text (ascii) to number (int)
20     return int(text) if text.isdigit() else text
21
22 def natural_keys(text): #Function that sorts input in descending
     order.
23     return [ atoi(c) for c in re.split(r'(\d+)', text) ]
24
25 splitt_file="SandfangH216,211" #Name of HF file you want to plot
26
27 #Path of splitt file
28 path="C:\\Users\\Christoffer Surdal\\OneDrive - NTNU\\Koding\\Logg
     splitting\\"+splitt_file+".txt"
29
30 #Extracts time, pressure and flow lists from HF file in Path.
31 time,pres,flow=splitt(path)
32
33 time_list=[]#creates empty list for time
34 for element in time: #iterate over times in time list from HF file
35     date_time = datetime.datetime.strptime(str(element), "%H:%M:%S"
     ) #Coverts to datetime object
36     time_list.append(date_time) #Appends date time object to
     time_list
37
38
39
40 ae_list=[]
```

```
rt=[]
r=[]
Rate_list=[]
aerate=[]

i=0 #Sets i to 0
path="C:\\Users\\Christoffer Surdal\\Desktop\\filt_S_J_fin"#Path to filtered AE-files


for root,dir,files in os.walk(path): #Return tuples of  root, directory and files
    files.sort(key=natural_keys) #Sorts the files in numerical order
    for filename in files: #Iteralte over files in the file tuple
        file_path=str(os.path.join(path,filename)) #Joins the filename and path,
        rate,rate_time=ae(file_path) #Extracts rate and rate time from ae file path
        #Iterate over time m in ae time list and n in HF time list
        for m in rate_time:
            for n in time:
                if m==n: #If ae time = HF time
                    for y in rate_time: #Iterate over time of rate
                        x=datetime.datetime.strptime(str(y), "%H:%M:%S") #Create date time object of rate time
                        rt.append(x) #Rate time /rt append date time object
                    for x in rate: #Iterate over rate list
                        r.append(x) #Append elements of rate list to r


while i<len(rt): #While i less than rate time
    if rt[i]>=time_list[0]: #If rate time at index i is larger or equal to time_list index 0
        Rate_list.append(rt[i]) #rt index i is appended to rate list
        aerate.append(r[i]) #And ae rate at same integer is appended
    else:
        pass #If not pass
    i=i+1


#Change every integer in ae rate, pressure and flow to flaot
RATE=[float(i) for i in aerate]
```

```
77 PRES=[float(i) for i in pres]
78 FLOW=[float(i) for i in flow]
79
80 #Create x axis for  rate time
81
82 x3=matplotlib.dates.date2num(Rate_list)
83
84
85
86 y1=PRES #assigns rate flow and rate to y1,y2,y3
87 y3=FLOW
88 y4=RATE
89
90 #Create x axis for HF time
91 x1=matplotlib.dates.date2num(time_list)
92 #Sets tick spacing
93 tick_spacing=5
94
95 color1="mediumblue"#Predefines some colors
96 color2="lightseagreen"
97 color3="red"
98
99 #Create a figure
100 fig, ax1=plt.subplots(figsize=(10,8))
101 #Sets labels
102 ax1.set_xlabel("Time")
103 ax1.set_ylabel("Pressure (bar) / Flow (l/min)")
104 #Plots AE rate and pressure and FLOW
105
106 l1,=ax1.plot_date(x1,y1,color=color1,linestyle="-",marker="")
107 l2,=ax1.plot_date(x1,y3,color=color2,linestyle="-",marker="")
108 ax1.tick_params(axis="y")
109
110 #Following code snippets is just to format the plot
111 ax1.xaxis.set_minor_locator(AutoMinorLocator())
112 ax3=ax1.twinx()
113 ax3.set_ylabel("AE rate / 5 sec",color=color3)
114 ax3.set_ylim(0,max(y4)+5, 1.0)
115 ax3.tick_params(axis="y")
116 l4=ax3.bar(x3,y4,width=0.00001,color=color3)
117 ax3.xaxis.set_major_formatter(dates.DateFormatter('%d/%m'))
118 ax3.xaxis.set_minor_locator(AutoMinorLocator())
119 ax3.tick_params(axis="y",labelcolor=color3)
120 fig.canvas.set_window_title(splitt_file)
121 fig.legend((l1, l2, l4), ('Pressure', 'Flow','AE Rate'), 'lower
    left',prop={'size': 10})
122 plt.gca().xaxis.set_major_formatter(dates.DateFormatter('%H:%M:%S')
```

```
    )
fig.autofmt_xdate()
plt.title(splitt_file)
fig.tight_layout()
ax3.set_ylim(0,max(y4)+5)
ax1.set_ylim(0,max(y1)+5)

#Shows plot
plt.show()
```

A.8 Pressure, flow extraction code

```
1
2 #Following code extracts time, pressure and flow from HF file
3 import datetime
4 import time
5
6 def splitt(file):
7     f=open(file,"r")
8
9     flow=[]
10    pres=[]
11    minutes=[]
12    pros_time=[]
13
14    for lines in f:
15        if "Tid:" in lines:
16            y=lines.split()
17
18        x= lines.strip()
19        if x:
20            x=x.split()
21
22            if len(x) == 4 and "og" not in x:
23                minutes.append(x[0])
24                pres.append(x[1])
25                flow.append(x[2])
26
27    start_time=y[1]
28
29    date_time = datetime.datetime.strptime(start_time, "%H:%M:%S")
30    time=date_time-datetime.datetime(1900,1,1)
31
32    seconds_tot=time.total_seconds()
33
34    for elements in minutes:
35        z=elements.replace(",",".")
36        y=float(z)*60
37        x=seconds_tot+y
38        time=datetime.timedelta(seconds=x)
39        x = time - datetime.timedelta(microseconds=time.
   microseconds)
40        pros_time.append(x)
41
42    pros_flow=[]
43    pros_pres=[]
44    for elements in flow:
```

```
45          z=elements.replace(",",".")
46
47          pros_flow.append(z)
48
49      for elements in pres:
50          z=elements.replace(",",".")
51
52          pros_pres.append(z)
53
54
55      return(pros_time,pros_pres,pros_flow)
56      f.close()
```

B Noise catalogue

B.1 Blasting signal

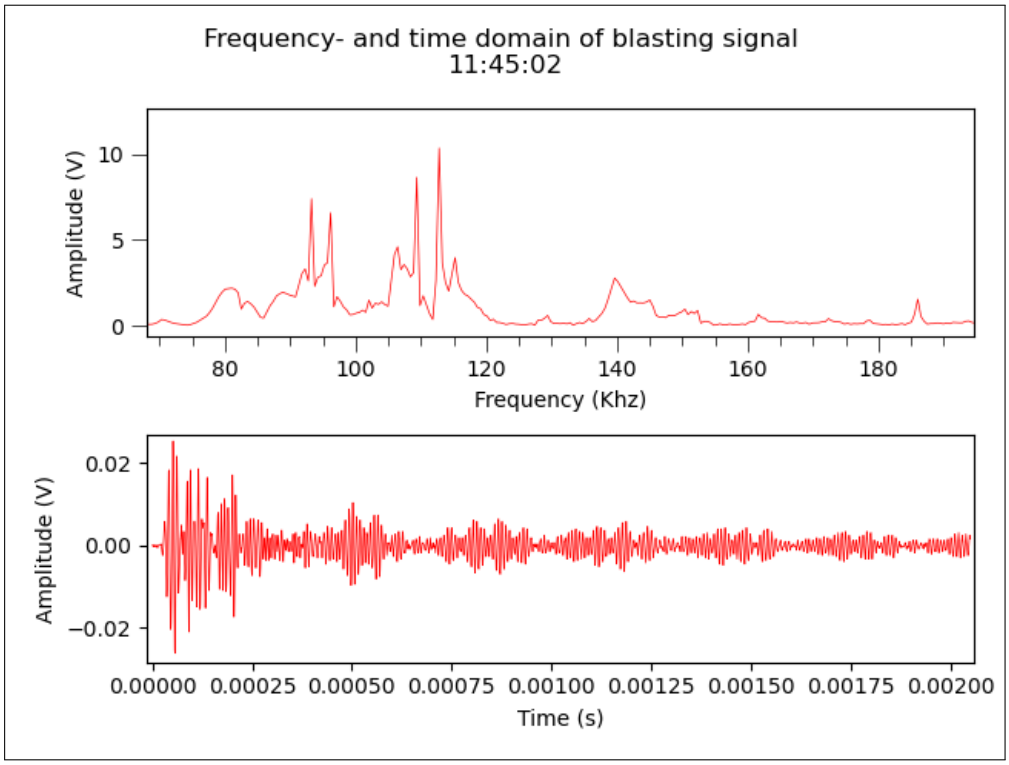

B.2 Vibration signal

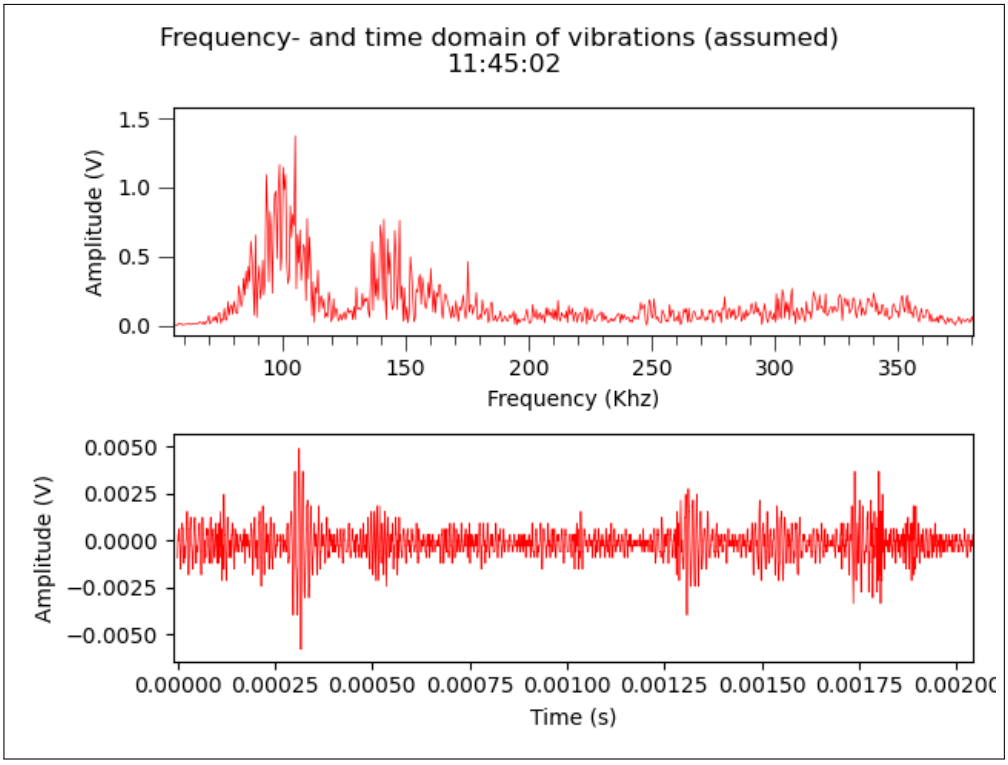

B.3 Hammer impact signal

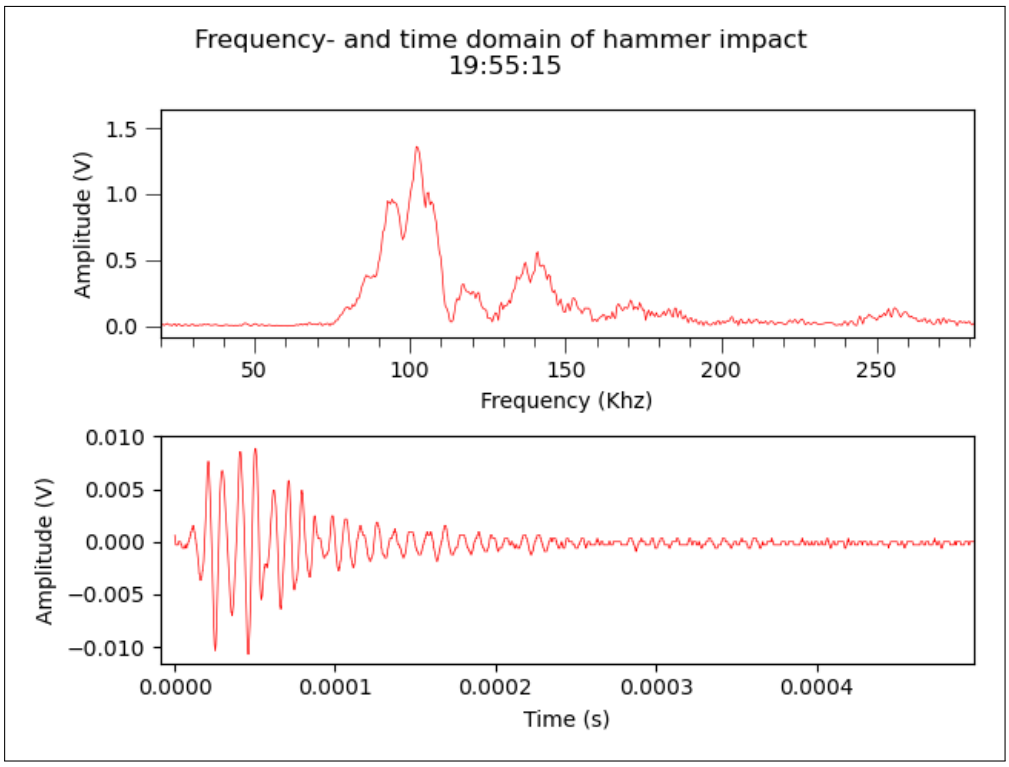

B.4 Drilling signal

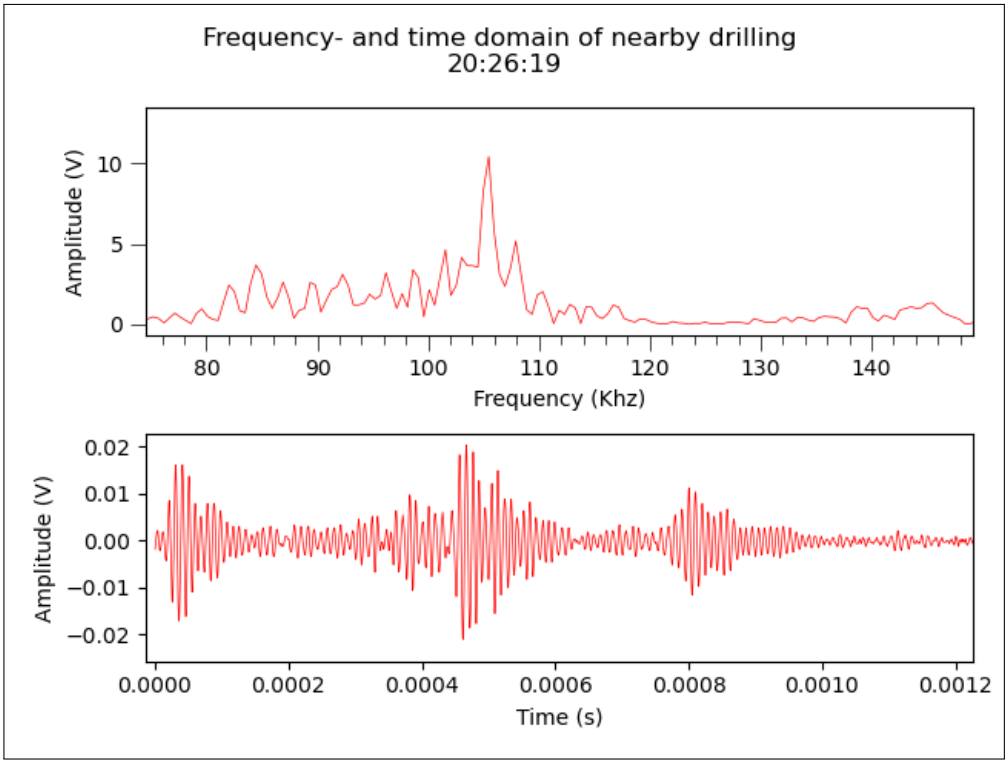

B.5 Electric signal

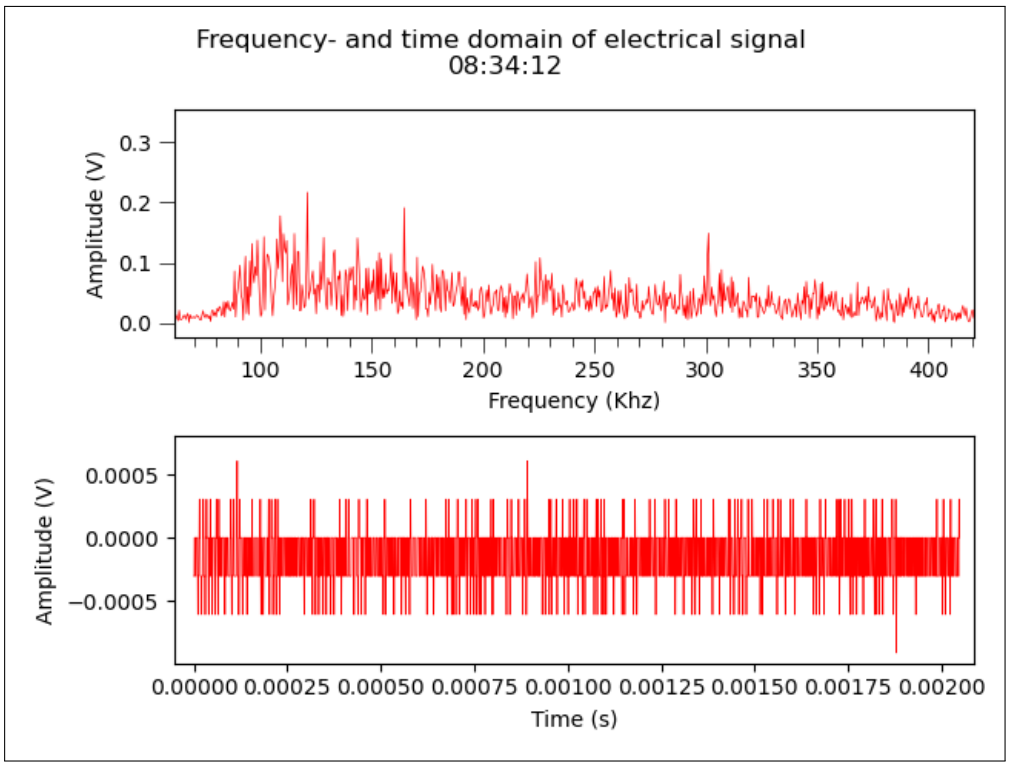

C Unfiltered plots

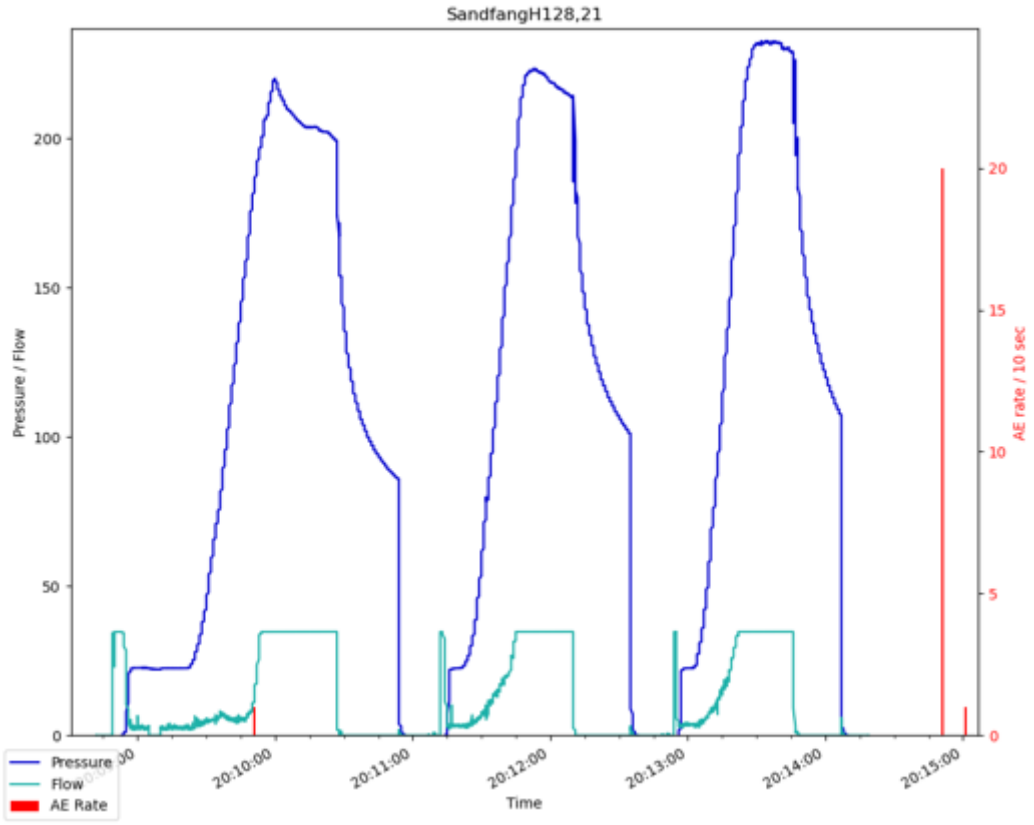

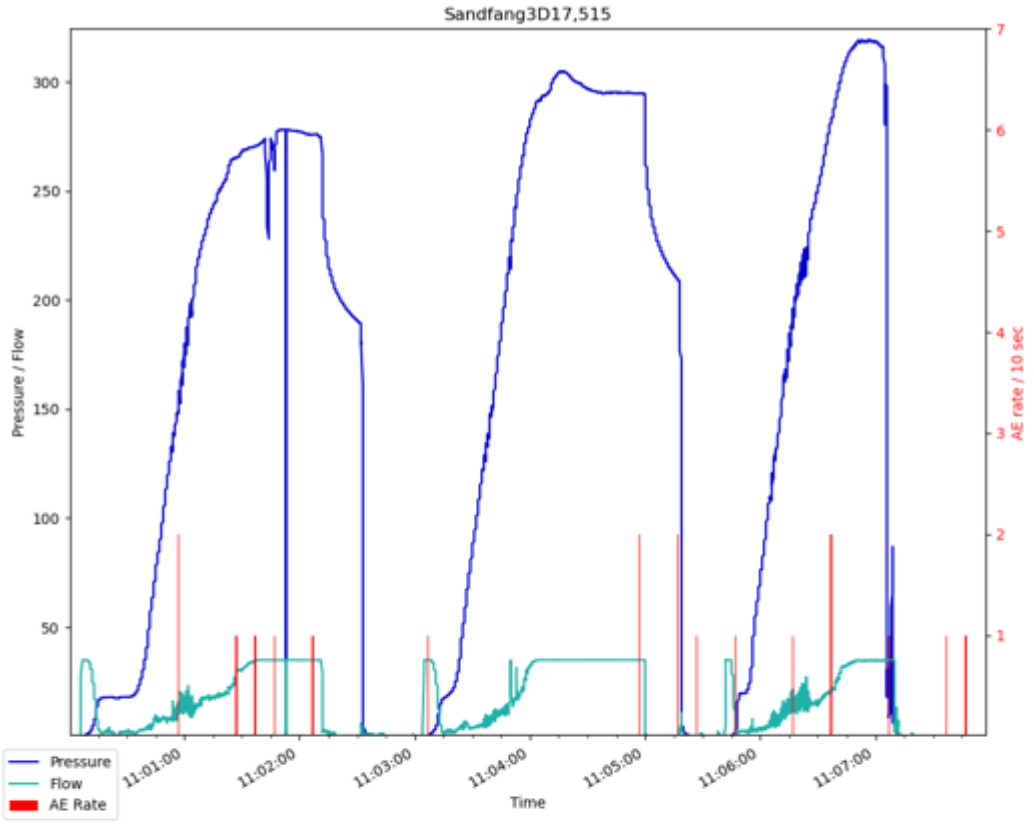
Sandfang3D17,515
Pressure / Flow
AE rate / 10 sec
Time
Pressure
Flow
AE Rate
11:01:00
11:02:00
11:03:00
11:04:00
11:05:00
11:06:00
11:07:00

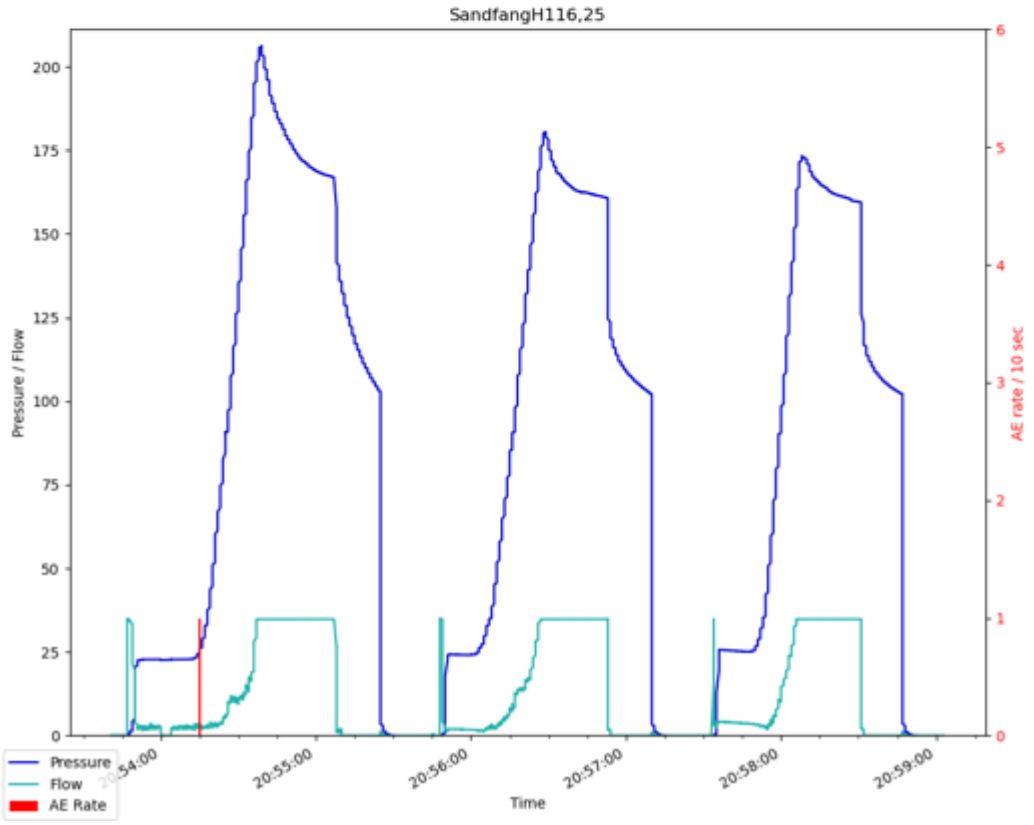
SandfangH116,25
Pressure / Flow
AE rate / 10 sec
Time
Pressure
Flow
AE Rate
20:55:00
20:56:00
20:57:00
20:58:00
20:59:00

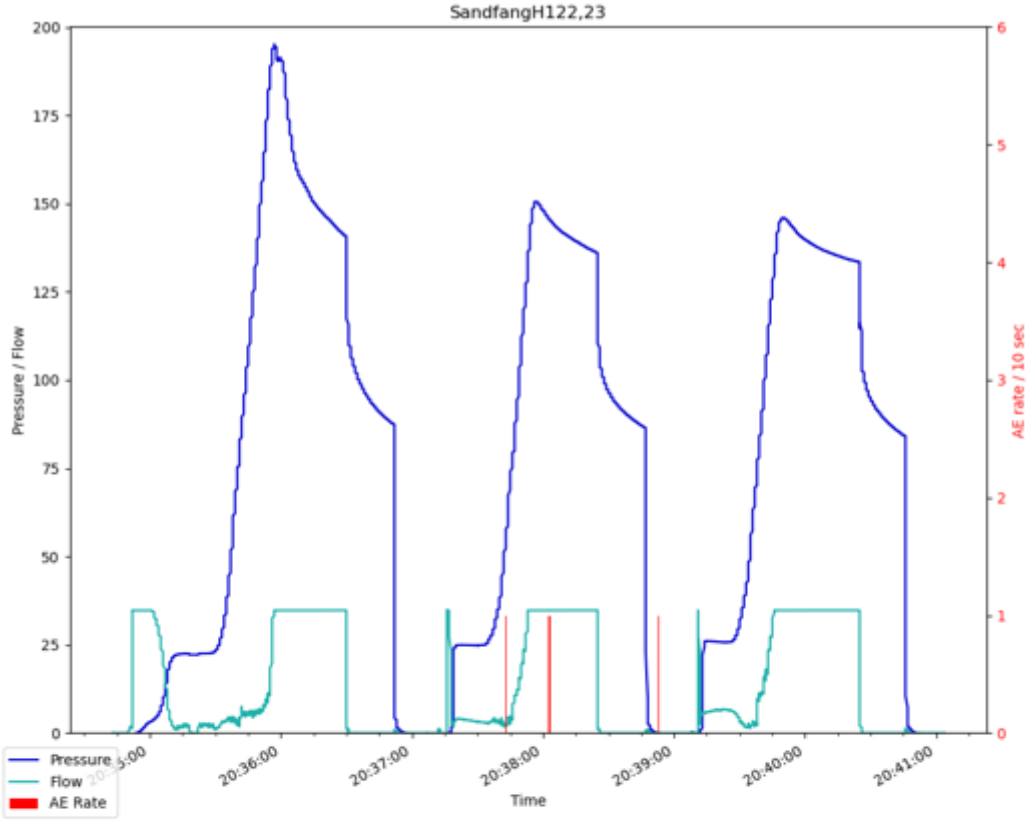
SandfangH122,23
Pressure / Flow
AE rate / 10 sec
Time
Pressure
Flow
AE Rate
20:36:00
20:37:00
20:38:00
20:39:00
20:40:00
20:41:00

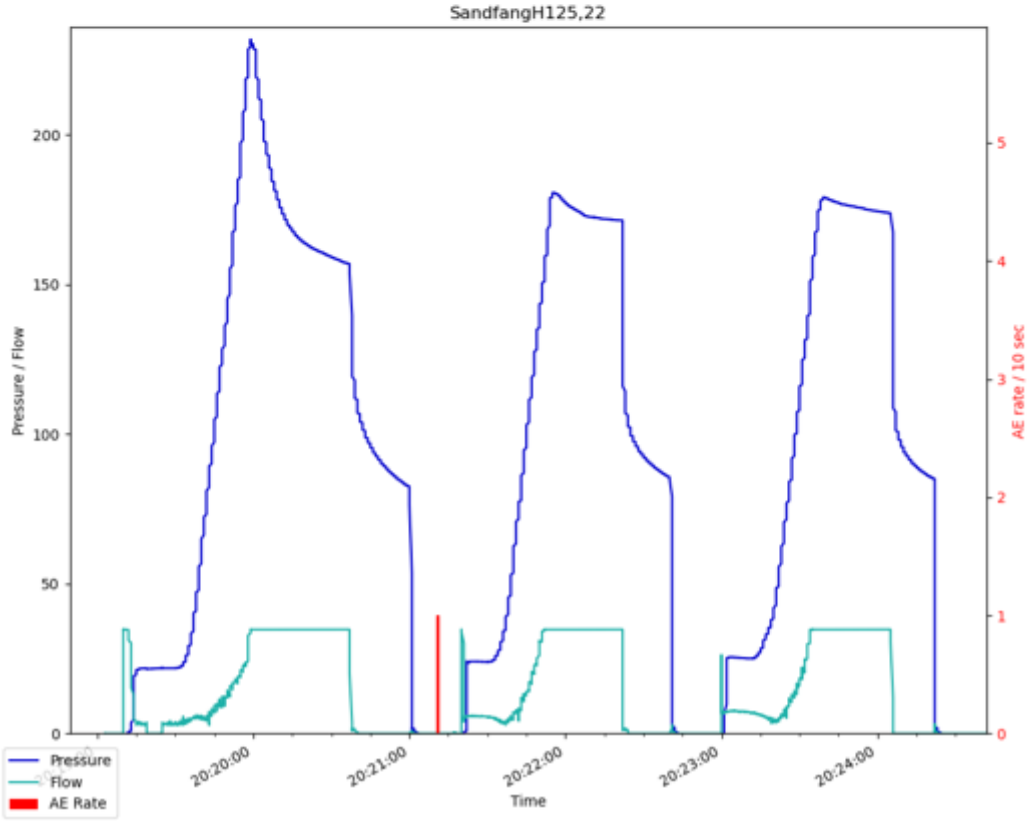
SandfangH125,22
Pressure / Flow
AE rate / 10 sec
Time
Pressure
Flow
AE Rate
20:20:00
20:21:00
20:22:00
20:23:00
20:24:00

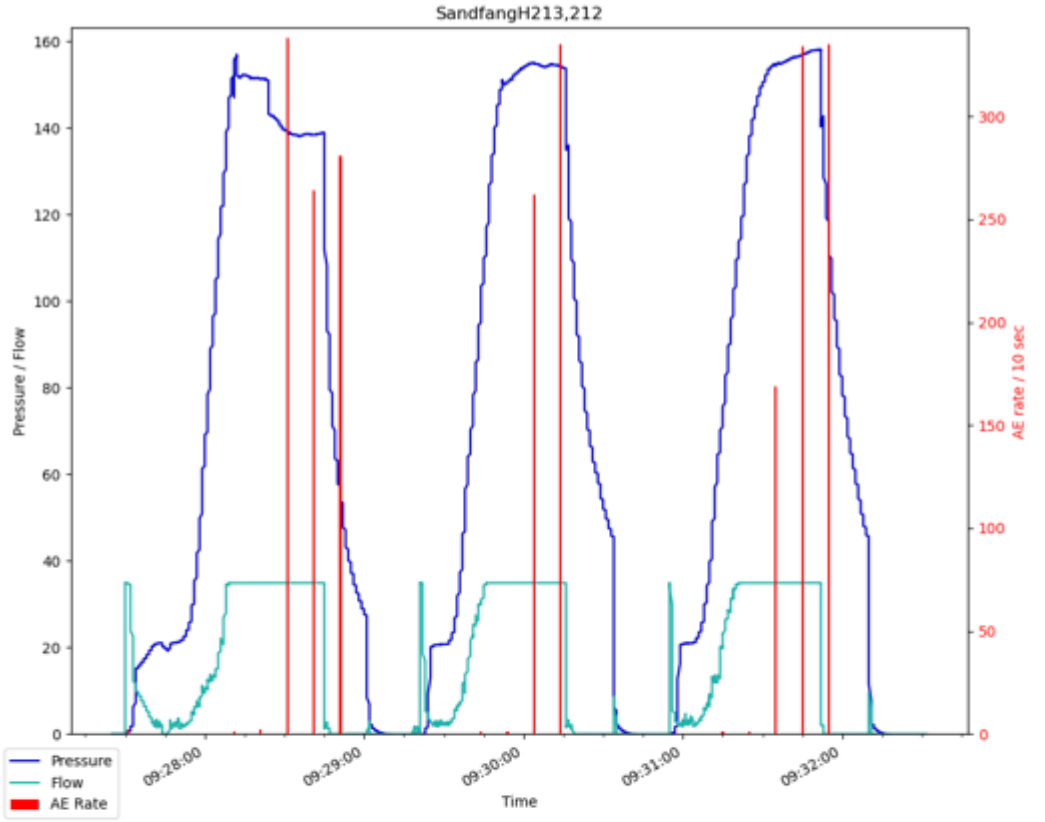
SandfangH213,212
Pressure / Flow
AE rate / 10 sec
Time
Pressure
Flow
AE Rate
09:28:00
09:29:00
09:30:00
09:31:00
09:32:00

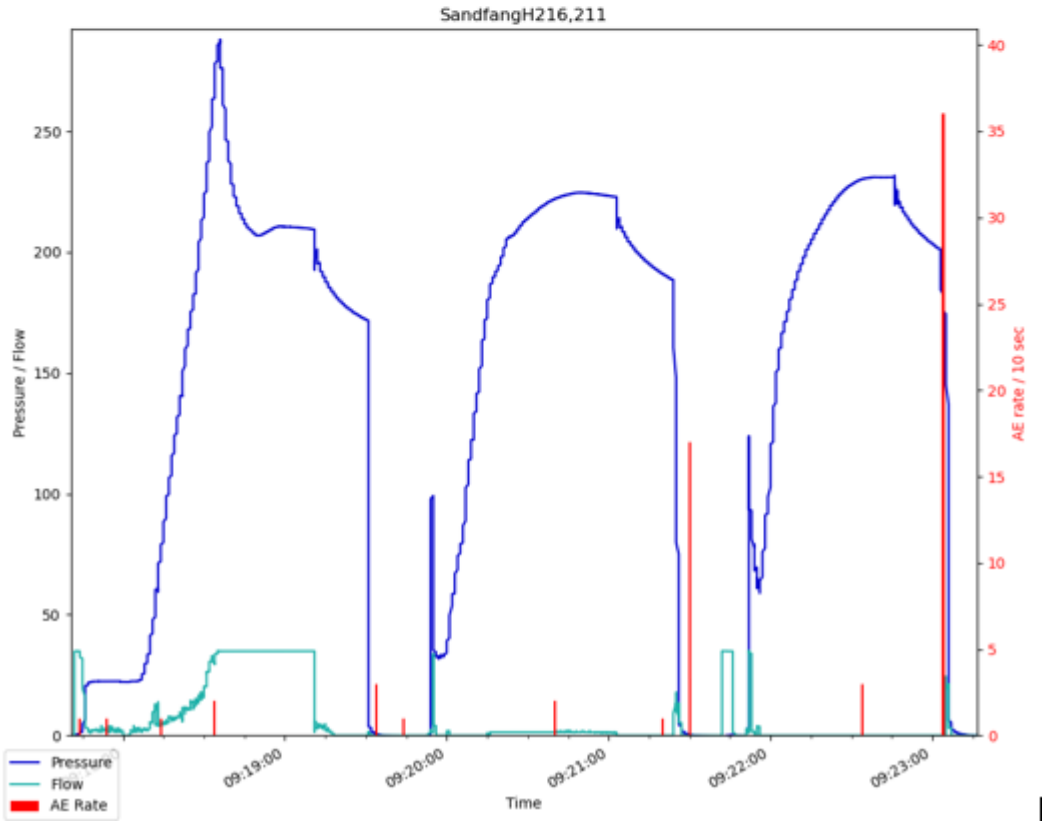
SandfangH216,211
Pressure / Flow
AE rate / 10 sec
Time
Pressure
Flow
AE Rate
09:19:00
09:20:00
09:21:00
09:22:00
09:23:00

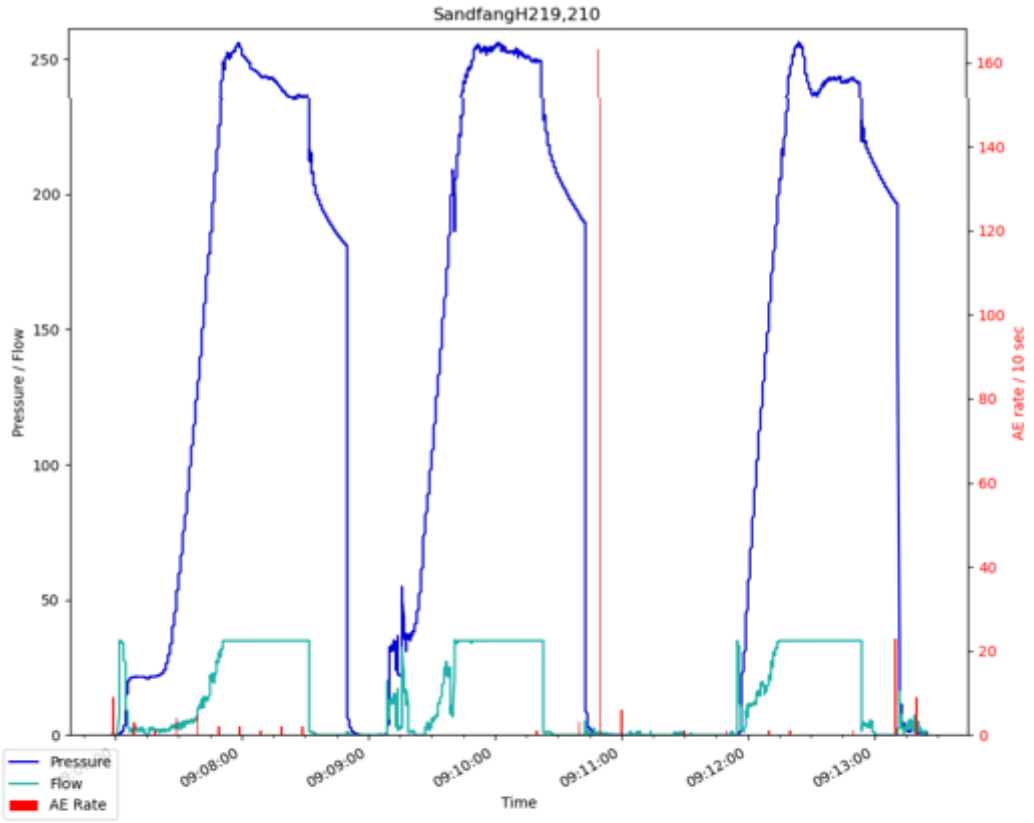
SandfangH219,210
Pressure / Flow
AE rate / 10 sec
Time
Pressure
Flow
AE Rate
09:08:00
09:09:00
09:10:00
09:11:00
09:12:00
09:13:00

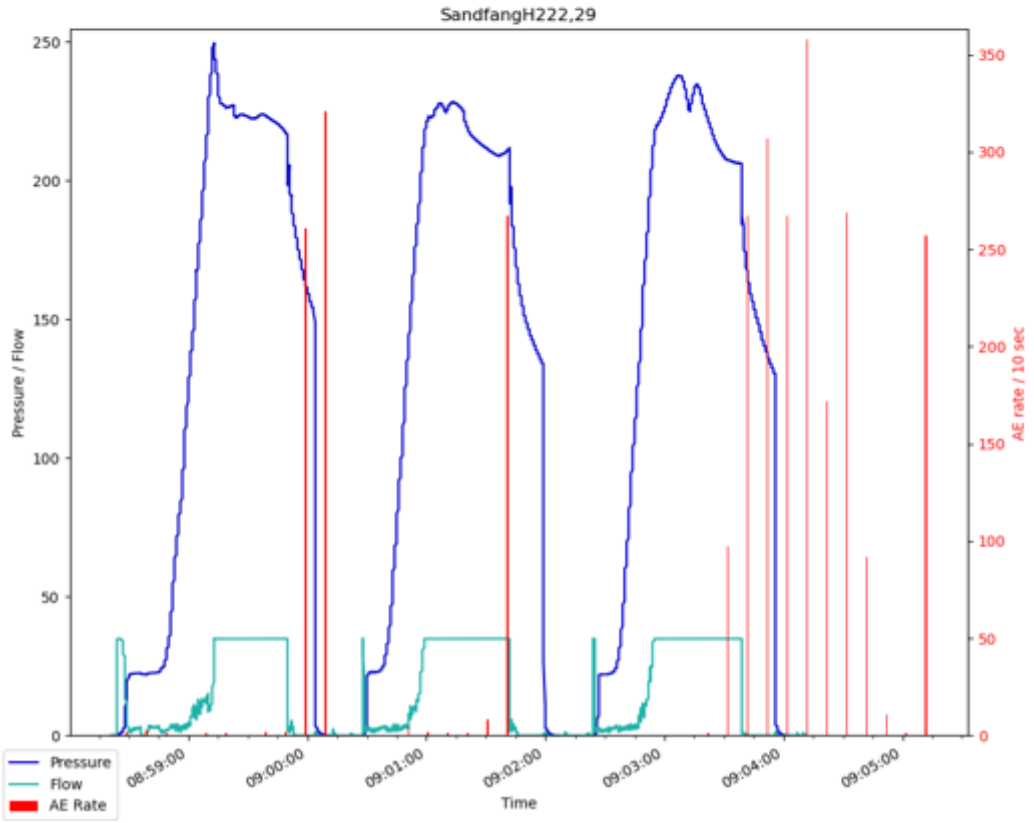
SandfangH222,29
Pressure / Flow
AE rate / 10 sec
Time
Pressure
Flow
AE Rate
08:59:00
09:00:00
09:01:00
09:02:00
09:03:00
09:04:00
09:05:00

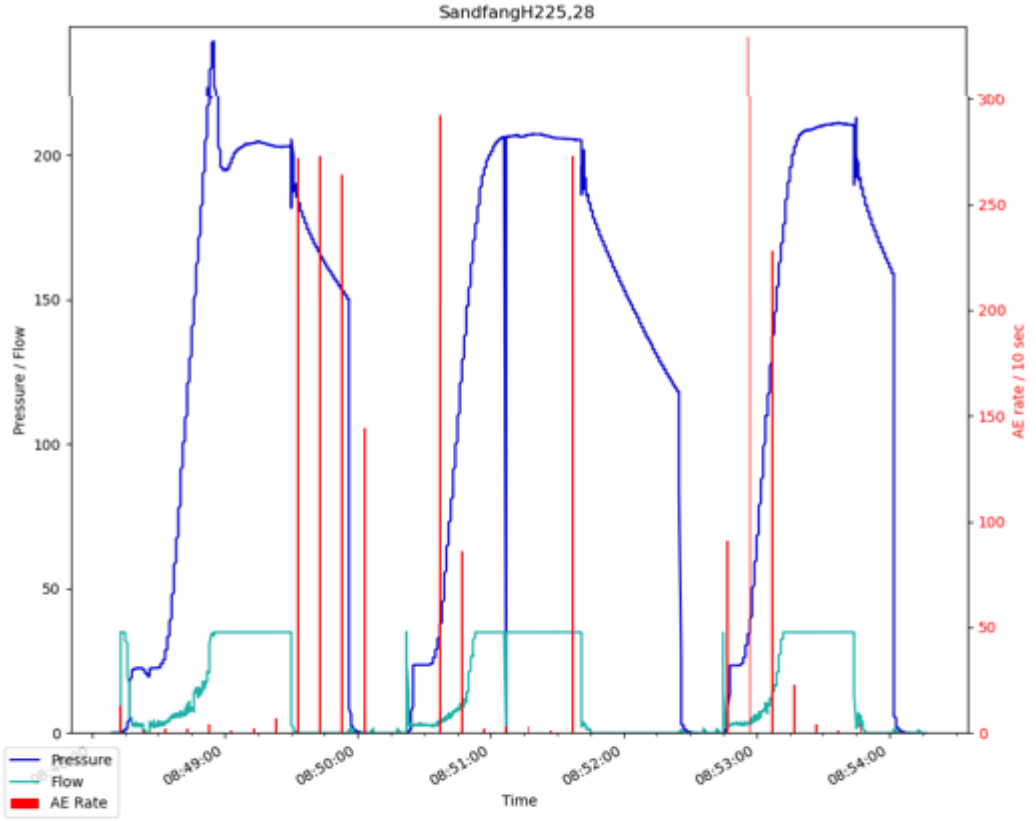
SandfangH225,28
Pressure / Flow
AE rate / 10 sec
Time
Pressure
Flow
AE Rate
08:49:00
08:50:00
08:51:00
08:52:00
08:53:00
08:54:00

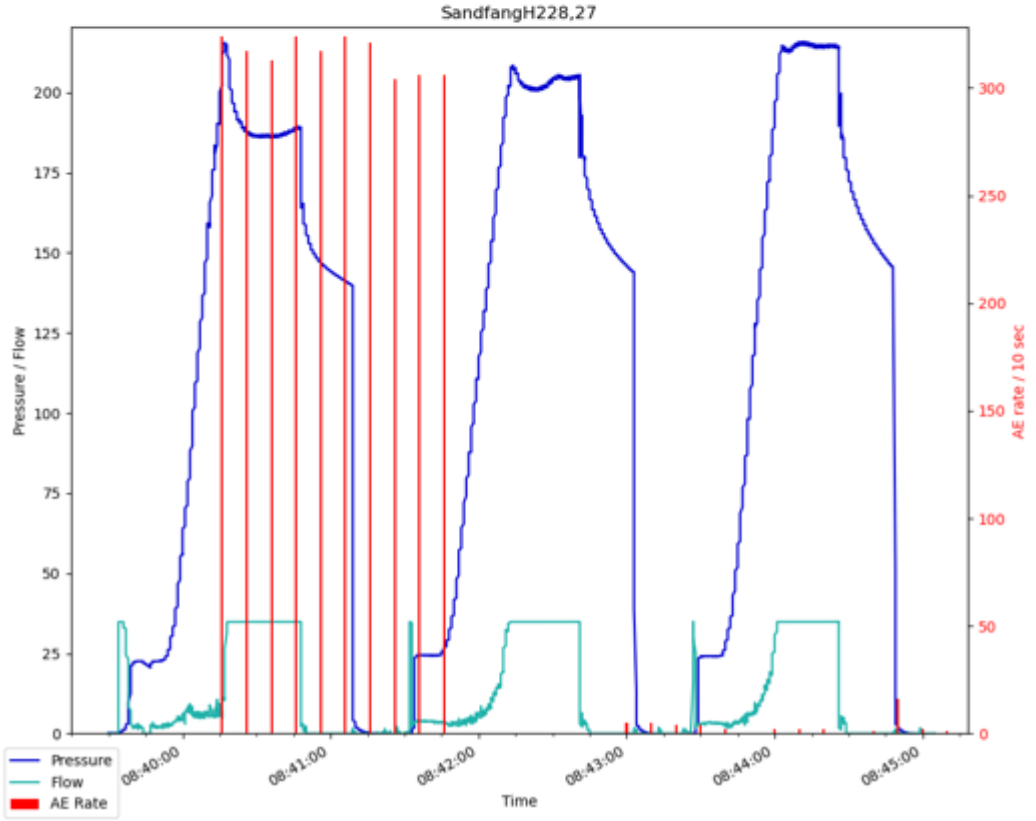
SandfangH228,27
Pressure / Flow
AE rate / 10 sec
Time
Pressure
Flow
AE Rate
08:40:00
08:41:00
08:42:00
08:43:00
08:44:00
08:45:00

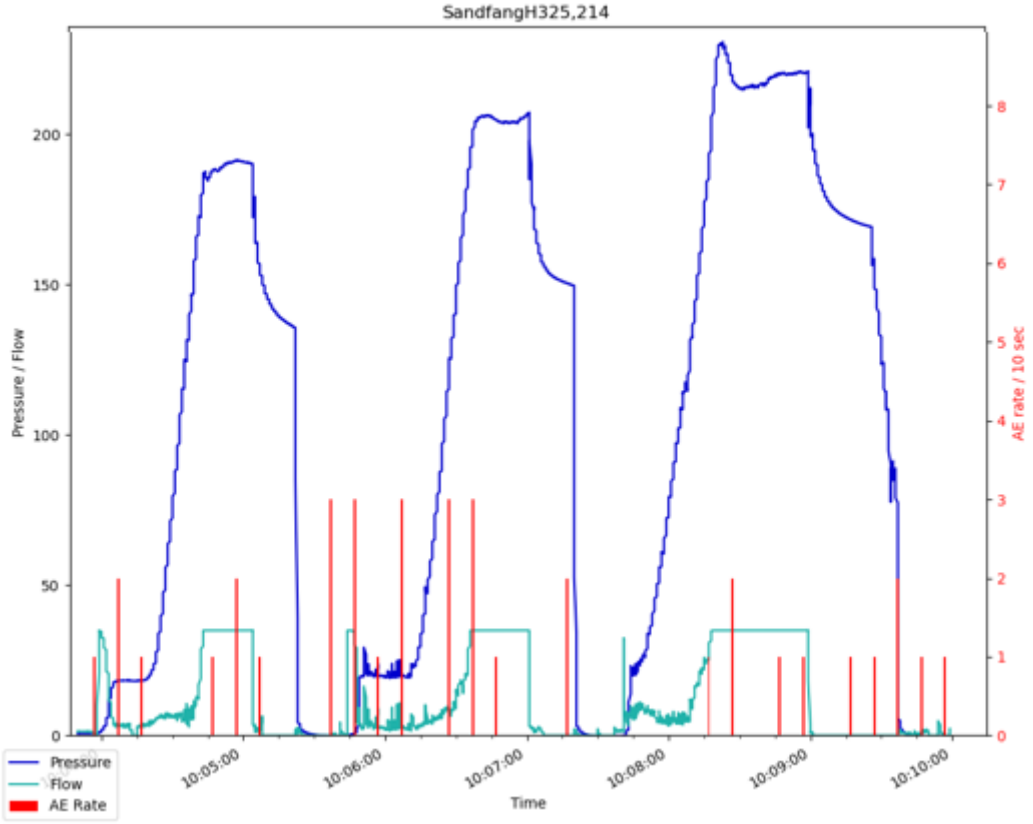
SandfangH325,214
Pressure / Flow
AE rate / 10 sec
Time
Pressure
Flow
AE Rate
10:05:00
10:06:00
10:07:00
10:08:00
10:09:00
10:10:00

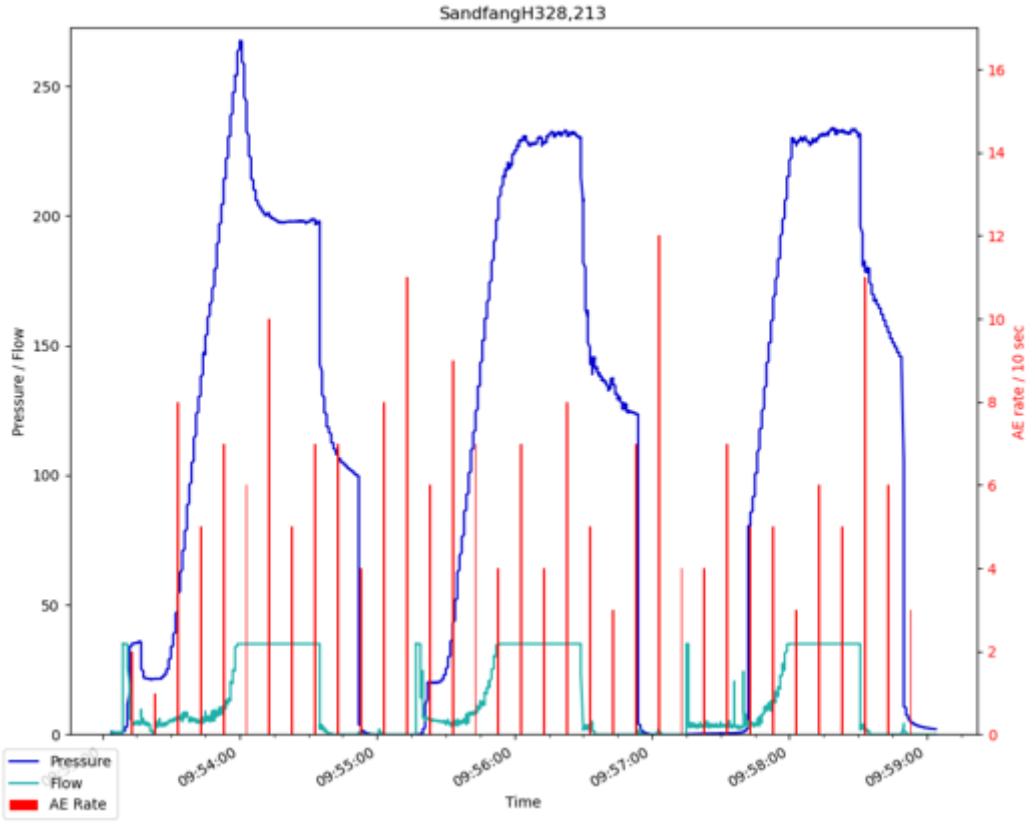
SandfangH328,213
Pressure / Flow
AE rate / 10 sec
Time
Pressure
Flow
AE Rate
09:54:00
09:55:00
09:56:00
09:57:00
09:58:00
09:59:00

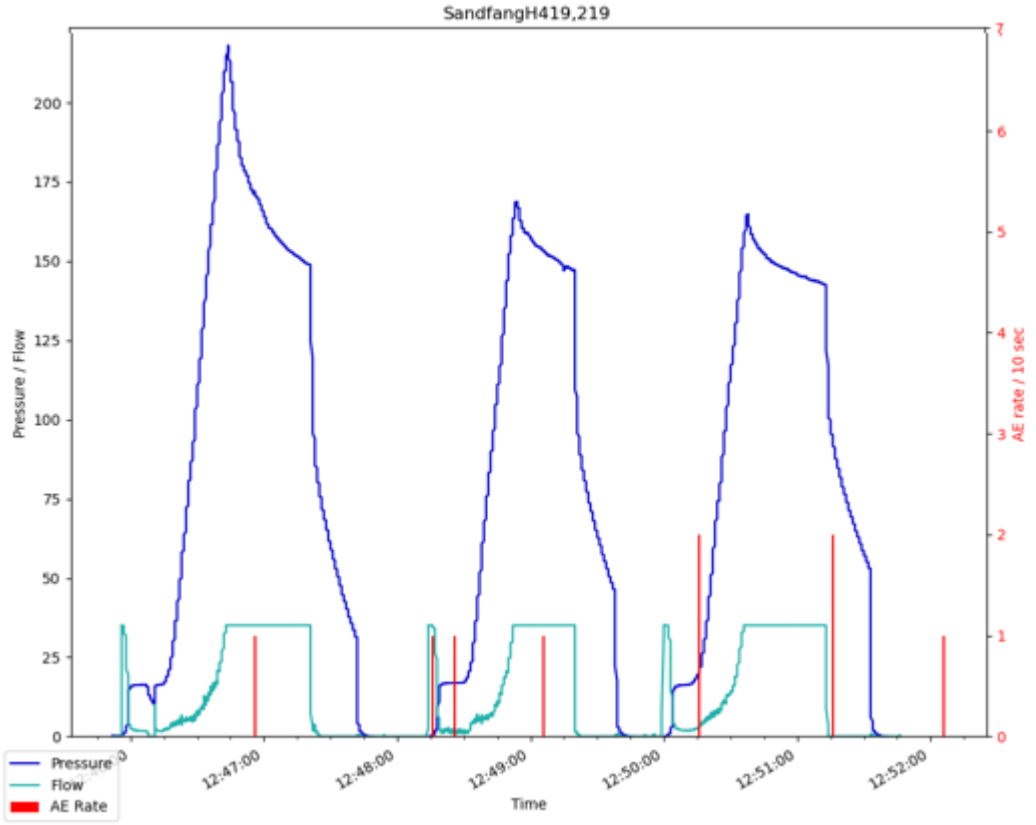
SandfangH419,219
Pressure / Flow
AE rate / 10 sec
Time
Pressure
Flow
AE Rate
12:47:00
12:48:00
12:49:00
12:50:00
12:51:00
12:52:00

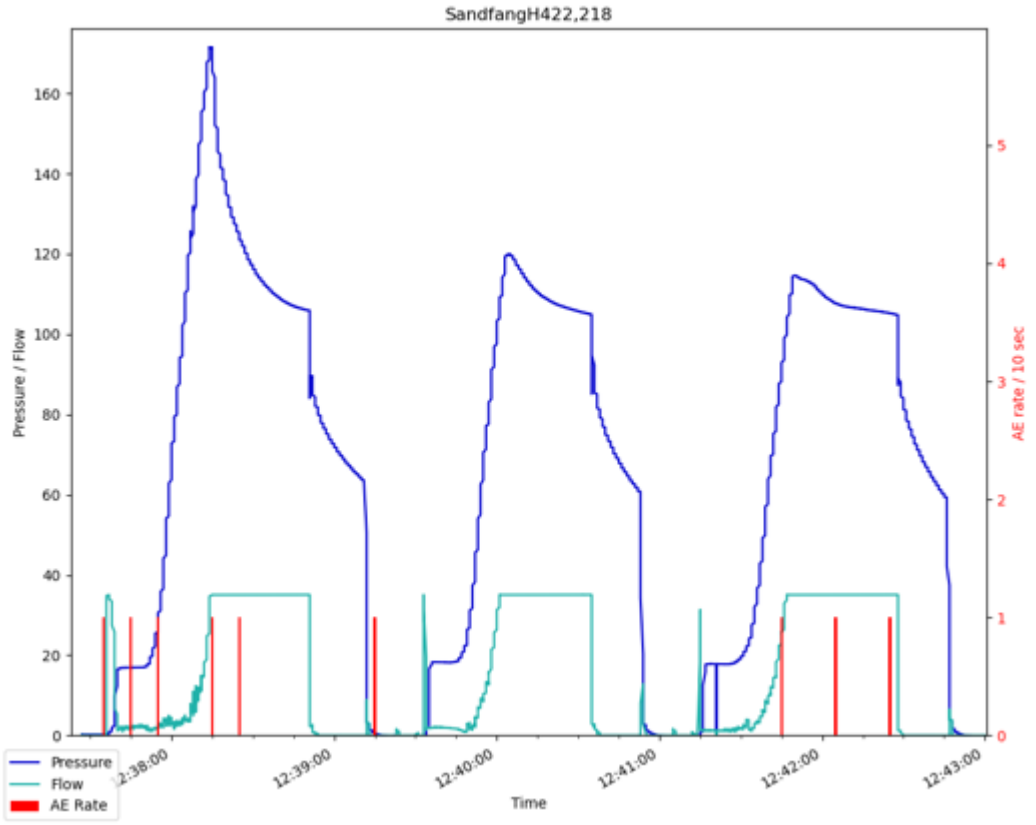
SandfangH422,218
Pressure / Flow
AE rate / 10 sec
Time
Pressure
Flow
AE Rate
12:39:00
12:40:00
12:41:00
12:42:00
12:43:00

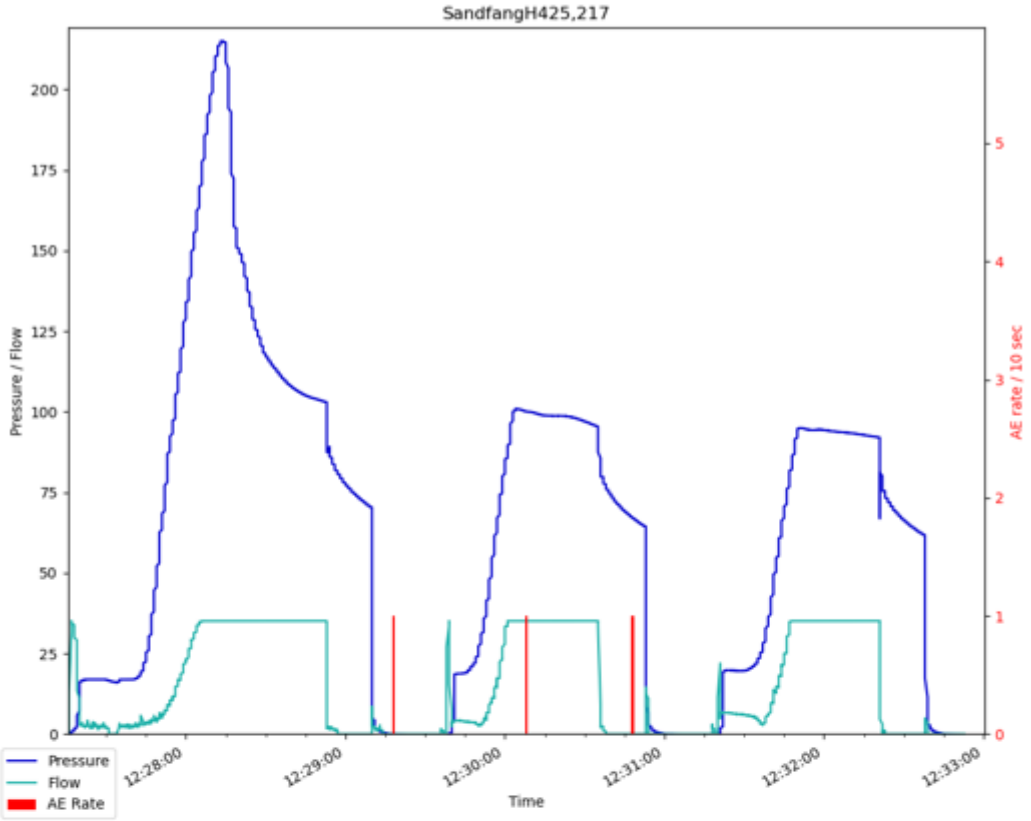
SandfangH425,217
Pressure / Flow
AE rate / 10 sec
Time
Pressure
Flow
AE Rate
12:28:00
12:29:00
12:30:00
12:31:00
12:32:00
12:33:00

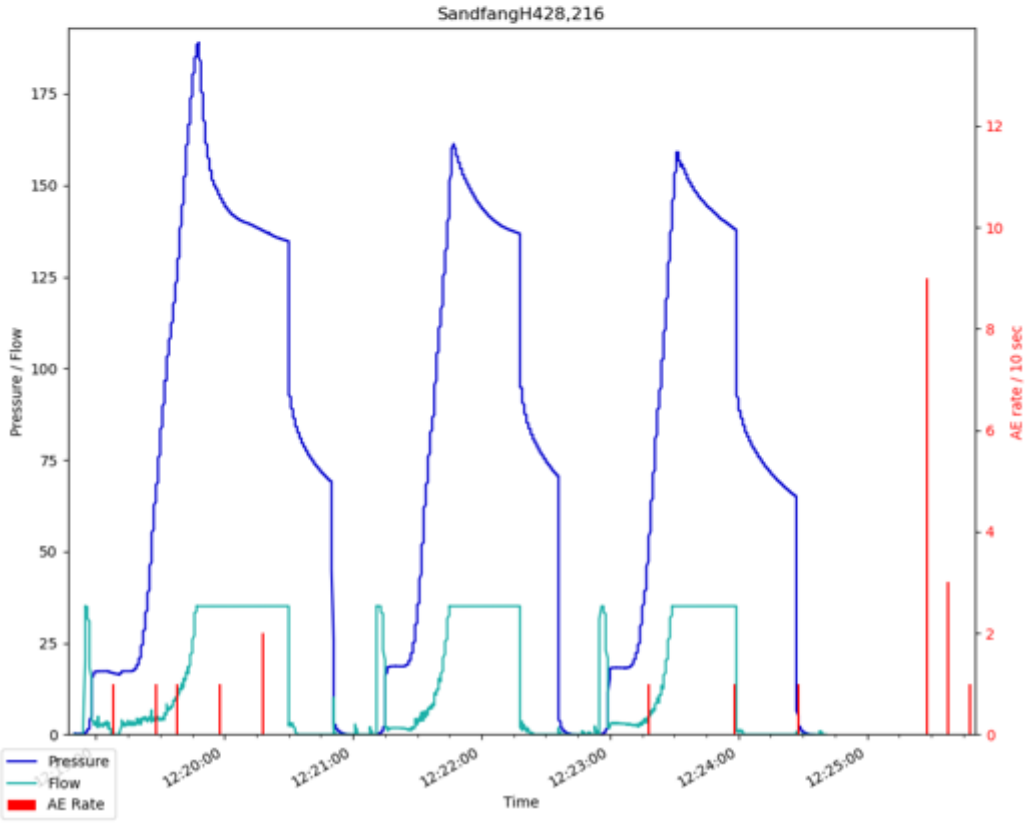
SandfangH428,216
Pressure / Flow
AE rate / 10 sec
Time
Pressure
Flow
AE Rate
12:20:00
12:21:00
12:22:00
12:23:00
12:24:00
12:25:00